

**Investigating the Effect of Austenite Grain Size and Grain Boundary Character on
Deformation Twinning Behavior in A High-Manganese TWIP Steel: A TEM In-Situ
Deformation Study**

Chang-Yu Hung

Dissertation submitted to the faculty of the
Virginia Polytechnic Institute and State University
in partial fulfillment of the requirements for the degree of
Doctor of Philosophy
in
Materials Science and Engineering

Mitsuhiro Murayama, Chair

William T. Reynolds

Norman E. Dowling

James M. Howe

May 27th, 2021

Blacksburg, Virginia

Keywords: ultrafine grained materials, TWIP Steel, twin boundary migration, grain boundary, deformation twinning, strain mapping, in situ transmission electron microscopy (TEM)

Investigating the Effect of Austenite Grain Size and Grain Boundary Character on Deformation Twinning Behavior in A High-Manganese TWIP Steel: A TEM In-Situ Deformation Study

Chang-Yu Hung

Abstract

Nanocrystalline metals exhibit a high strength/hardness but generally poor ductility during deformation regardless of their crystal structure which is often called the strength-ductility trade-off relationship and generally appears in most ultrafine-grained metals. The ultrafine-grained (UFG) high manganese austenitic twinning-induced plasticity (TWIP) steels have been found to overcome the strength-ductility trade-off but their underlying mechanism of discontinuous yielding behavior has not been well understood. In this study, our systematic TEM characterization suggests that the plastic deformation mechanisms in the early stage of deformation, around the macroscopic yield point, show an obvious association with grain size and nucleation of deformation twin was promoted rather than suppressed in UFG. More specifically, the main mechanism shifts from the conventional slip in grain interior to twinning nucleated from grain boundaries with decreasing the grain size down to less than 1 μm . We also provide insights into the atomistic process of deformation twin nucleation at $\Sigma 3\{111\}$ twin boundaries, the dominant type of grain boundary in the UFG-TWIP steel of interest. In response to the external tensile stresses, the structure of coherent $\Sigma 3\{111\}$ twin boundary changes from atomistically smooth to partly defective by the grain boundary migration mechanism thus the “kink-like” defective step can act as a nucleation site for deformation twin, which deformation process is different from the one induced by dislocation pile-ups in coarse-grained counterparts and explain why UFG TWIP steel can retain the moderate ductility.

In addition to the effect of grain size on deformation twin nucleation, grain boundary character was also taken into account. In coarse-grained TWIP steel, we experimentally reveal that deformation twin nucleation occurs at an annealing twin ($\Sigma 3\{111\}$) boundary in a high-Mn austenitic steel when dislocation pile-up at $\Sigma 3\{111\}$ boundary produced a local stress exceeding the twinning stress, while no obvious local stress concentration was required at relatively high-energy grain boundaries such as $\Sigma 21$ or $\Sigma 31$. A periodic contrast reversal associated with a sequential stacking faults emission from $\Sigma 3\{111\}$ boundary was observed by in-situ transmission electron microscopy (TEM) deformation experiments, proving the successive layer-by-layer stacking fault emission was the deformation twin nucleation mechanism. The correlation between grain boundary character and deformation behavior was discussed both in low- and high-sigma value grain boundaries. On the other hand, localized strain concentration causes the nucleation of deformation twins at grain boundaries regardless of the grain boundary misorientation character in UFG TWIP steel. The invisibility of stacking fault (zero contrast) was also observed to be emitted at $\Sigma 3\{111\}$ boundaries in the coarse-grained TWIP steel, which deformation twin nucleation mechanism is found to be identical to UFG Fe-31Mn-3Si-3Al TWIP steel.

Investigating the Effect of Austenite Grain Size and Grain Boundary Character on Deformation Twinning Behavior in A High-Manganese TWIP Steel: A TEM In-Situ Deformation Study

Chang-Yu Hung

General Audience Abstract

High manganese (Mn) twin-induced plasticity (TWIP) steel is a new type of steels which exhibit pronounced strain hardening rate so that offering an extraordinary potential to adjust the strength-ductility relationship. This key advantage will help implement the current development of lightweighting components in automobile industry due to a considerable reduction of material use and an improved press formability. Such outstanding ductility can be contributed by the pronounced strain hardening rate during every such deformation processes, which is highly associated with several different controlling parameters, i.e., SFE, grain orientation, grain size, and grain boundary characters. In this study, we take particular attention to the effect of grain size and grain boundary characters on deformation twinning behavior besides well-known parameters such as SFE and grain orientation.

The effect of grain size on deformation twinning behavior was found to be deeply associated with the yielding behavior in TWIP steel, i.e., a discontinuous yielding behavior with a unique yield drop was observed in ultrafine-grained TWIP while a continuous yielding behavior was observed in coarse-grained counterpart. Our TEM characterization indicates that the microstructural features of grains $>10\ \mu\text{m}$ are different from the microstructural features in grains $<1\ \mu\text{m}$. In over- $10\ \mu\text{m}$ grains, normal dislocation slips and the formation of in-grain stacking faults are the main deformed microstructure. However, in the under- $1\ \mu\text{m}$ grains, the in-grain dislocation slip is inhibited, but the deformation twinning is promoted at grain boundaries.

This deformation transition from in-grain slip to twinning at grain boundary appears to be responsible for the discontinuous yielding behavior observed in stress-strain curve.

The effect of grain boundary character on deformation twinning was examined in both coarse- and ultrafine-grained TWIP steels. In coarse-grained TWIP steel, we found that deformation twinning behavior varies as the function of boundary structure, i.e., different atomic configuration. Coherent twin boundary can act as a nucleation site for deformation twin as a localized strain concentration was introduced by dislocation pile-ups. On the other hand, incoherent boundaries can act as a deformation twin nucleation site by a boundary relaxation mechanism, i.e., grain-boundary dislocations can dissociate into partial dislocations to both side of boundary to accommodate the misfit between grains. In UFG TWIP steel, we found that the coherent twin boundary can act as a deformation twin nucleation site without presence of dislocation pile-ups. Alternatively, twin boundary becomes defective with a “kink-like” step by boundary migration. As a result, this defective step would progressively accumulate localized strain field thus stimulate the nucleation of deformation twin. Such study provides a novel insight into the UFG TWIP steel and a roadmap toward controlling TWIP effect.

Attribution

The collaborators in this work and co-authors of the resulting publications are:

Mitsuhiro Murayama – *Professor at Virginia Tech, Department of Materials Science and Engineering*

Nobuhiro Tsuji – *Professor at Kyoto University, Department of Materials Science and Engineering*

Yu Bai – *Assistant Professor at Kyoto University, Department of Materials Science and Engineering*

Tomotsugu Shimokawa – *Professor at Kanazawa University, Faculty of Mechanical Engineering*

The specific contributions from my collaborators are as follows:

Chapter 3: Chang-Yu Hung and Dr. Murayama designed the experimental and wrote the paper. Chang-Yu Hung performed microstructural characterizations. Dr. Bai and Dr. Tsuji fabricated the alloy and performed mechanical properties tests. All authors discussed the results and commented on the manuscript.

Chapter 4: Chang-Yu Hung and Dr. Murayama designed the experimental and wrote the paper. Chang-Yu Hung performed microstructural characterizations. Dr. Bai and Dr. Tsuji fabricated the alloy and performed mechanical properties tests. Dr. Shimokawa performed crystallography-based geometric analyses. All authors discussed the results and commented on the manuscript.

Chapter 5: Chang-Yu Hung and Dr. Murayama designed the experimental and wrote the paper. Chang-Yu Hung performed microstructural characterizations. Dr. Shimokawa performed Frank loop dislocation analyses. Dr. Bai and Dr. Tsuji fabricated the alloy. All authors discussed the results and commented on the manuscript.

Table of Contents

Abstract	ii
Attribution.....	vi
Table of Contents	viii
List of Figures	xi
List of Tables.....	xiv
Chapter 1 Introduction	1
1.1 Research objectives.....	5
1.2 Dissertation organization	6
Chapter 2 Background	7
2.1 Strain hardening of TWIP steel.....	7
2.2 Stacking fault energy in TWIP steel	11
2.3 Effect of geometrical relationship between grain orientation and tensile axis on TWIP steel.....	19
2.4 Grain size effect in TWIP steel.....	20
References.....	23
Chapter 3 Grain Size Altering Yielding Mechanisms in Ultrafine Grained High-Mn Austenitic Steel: Advanced TEM Investigations	27
Abstract.....	28
3.1 Introduction.....	29
3.2 Materials and Experimental Methods	32
3.2.1 Sample fabrication	32
3.2.2 Electron backscattered diffraction characterization.....	33

3.2.3 Uniaxial tensile test.....	33
3.2.4 Transmission electron microscopy characterization	34
3.3 Results.....	34
3.3.1 Pre-straining microstructure characterization	35
3.3.2 Deformation microstructure characterization	40
3.3.2.1 Coarse-grained TWIP steel: deformed to 0.02 engineering strain	40
3.3.2.2 UFG TWIP steel: deformed to 0.03 engineering strain	45
3.3.2.3. Ultrafine-grained TWIP steel: deformed to 0.046 engineering strain..	46
3.3.2.4 Ultrafine-grained TWIP steel: deformed to 0.062 engineering strain...	48
3.4 Discussion.....	49
3.4.1 Stacking fault nucleation in the coarse-grained TWIP steel	50
3.4.2 Stacking fault and deformation twin nucleation in ultrafine grained TWIP steel	53
3.5 Conclusions	57
Acknowledgements	60
References	61
 Chapter 4 A Correlation Between Grain Boundary Character and Deformation Twin	
Nucleation Mechanism in Coarse-grained High-Mn Austenitic Steel.....	68
Abstract	69
4.1 Introduction	70
4.2 Results	72
4.3 Discussion.....	84
4.4 Conclusions	92

4.5 Materials and Methods	93
Acknowledgements	95
Supplementary information	96
References	101
Chapter 5 The microstructural response of $\Sigma 3\{111\}$ twin boundary to plastic deformation in an ultrafine-grained high-manganese austenitic steel	108
Abstract	109
5.1 Introduction	110
5.2 Experimental procedure.....	112
5.2.1 Sample fabrication.....	112
5.2.2 Uniaxial tensile test	113
5.2.3 Electron backscattered diffraction characterization.....	113
5.2.4 Transmission electron microscopy characterization	114
5.2.5 In-situ deformation TEM.....	114
5.2.6 Strain mapping using microprobe STEM	114
5.3 Results	114
5.4 Discussion.....	124
5.5 Conclusions	133
References	134
Acknowledgements	140
Chapter 6 Conclusions	141

List of Figures

Chapter 2

Figure 2.1 The uniaxial tensile stress-strain curves for a Ti-stabalized interstitial-free (IF) ferritic steel	8
Figure 2.2 Normalized strain hardening rate (normalized by the shear modulus) vs. true stress.....	10
Figure 2.3 Normalized strain hardening rate for several different fcc materials	13
Figure 2.4 Optical micrographs of the sample deformed to true strain of -0.34.....	14
Figure 2.5 Schematic showing the range of SFE for deformation twinning.....	17
Figure 2.6 Bright-field TEM images of the T618–Si TWIP steel at various true strains	18
Figure 2.7 Inverse polar figure along tensile axis direction of Fe-22Mn-0.6C (wt.%) TWIP steel	20
Figure 2.8 Inverse pole figures showing the crystallographic orientation dependences of the deformation twinning	22

Chapter 3

Figure 3.1 An engineering stress-strain curve of Fe-31Mn-3Al-3Si	35
Figure 3.2 EBSD maps of fully recrystallized coarse-grained and UFG- samples	37
Figure 3.3 Bright field (BF) TEM images show the microstructures and defects in the coarse-grained sample	39
Figure 3.4 A series of $g \cdot b$ analyses performed to a grain in the coarse-grained sample deformed to engineering strain = 0.02	42
Figure 3.5 BF TEM images showing the microstructure and defects in the UFG sample	

deformed to engineering strain = 0.03	45
Figure 3.6 BF TEM images showing the microstructure and defects in the UFG sample deformed to engineering strain = 0.046	47
Figure 3.7 The microstructures and defects in the UFG sample deformed to engineering strain = 0.062	49
Figure 3.8 A schematic illustration shows the precursor of deformation twin initiated at the area near grain boundary	52
Figure 3.9 The representative initial deformed microstructure in the UFG sample	55

Chapter 4

Figure 4.1 BF TEM micrographs showing the representative microstructure and structural defects in the TWIP steel	74
Figure 4.2 Selected frames of an in-situ deforming TEM test video	77
Figure 4.3 An experimentally observed $\Sigma 21$ boundary is superimposed onto the [112] $\Sigma 21$ boundary structure model	80
Figure 4.4 A BF TEM image shows a stacking fault in the impingement region of an inclined $S3\{111\}$ boundary and a deformation twin emitted from the $\Sigma 31$ boundary .	82
Figure 4.5 Selected frames of an in-situ deformation TEM test near a $\Sigma 73$ boundary region	83
Figure 4.6 A schematic illustration shows the precursors of deformation twin are initiated at a near grain boundary region	85
Figure S1 The grain orientation of an as-received Fe-31Mn-3Al-3Si TWIP steel derived from EBSD.....	98
Figure S2 Schematic illustrations show how fringe contrast reversal occurs.....	99

Figure S3 An atomic structure model built to reproduce the geometrical relationship between Grains-I and -II in Fig. 4(a) 100

Chapter 5

Figure 5.1 EBSD maps of fully recrystallized (0%) and tensile strained (4.6% and 6.2%) UFG samples 116

Figure 5.2 BF images show the formation of deformation twins in a UFG TWIP steel sample deformed to the engineering strain = 0.062 118

Figure 5.3 Selected frames of a TEM in-situ deformation test video data near the $\Sigma 3\{111\}$ twin boundary 119

Figure 5.4 BF images taken in a zone axis = [011] and HRTEM images show two kink-like steps and a deformation twin nucleated from a defective step 122

Figure 5.5 BF images show three deformation twins nucleated from one side of $\Sigma 3$ twin boundary and Strain maps for three regions on the both sides of $\Sigma 3\{111\}$ twin boundary 124

Figure 5.6 Two pairs of BF TEM and HRTEM images show two representative boundary structures of two $\Sigma 3\{111\}$ twin boundaries 127

Figure 5.7 Two closed Frank circuits labeled by “A” and “B” used to analyze the steps 129

Figure 5.8 A schematic illustration shows a two-step mechanism to form a nucleation site for deformation twin at a coherent annealing twin boundary 132

List of Tables

Chapter 2

Table 2.1 The overview of the mechanical properties and the value of SFE in the Fe-xMn-0.6C-yAl TWIP steel.....	16
--	----

Chapter 3

Table 3.1 List of symbols used in TEM images	38
Table 3.2 The $g \cdot b$ for perfect and partial dislocations	43

Chapter 4

Table 4.1 List of symbols used in TEM images	73
---	----

Chapter 1

Introduction

High strength materials become highly demanded in the recent years, especially for the automobile industry, huge construction, and protecting human being from tremendous disasters. However, ductility is usually sacrificed with increasing strength because of universal strength-ductility trade-off relationship. We need to overcome this strength-ductility trade-off since high strength materials should be formable and can be machined to a certain shape for many applications.

High-manganese austenitic steels have been considered to be one of the potential candidates that could overcome strength-ductility trade-off because the interaction between different deformation mechanisms such as deformation twinning and normal in-grain slip, somehow induce a pronounced strain hardening rate thus postponing the occurrence of necking¹⁻³. Although the origin of this pronounced strain hardening rate has not been fully understood, it is commonly believed that the dynamical Hall-Petch effect is the controlling mechanism, i.e., deformation twins can be formed during deformation and act as obstacles to dislocation movement by reducing the mean free path of dislocations. This would result in a strong strain hardening and lead to increase strength and ductility simultaneously. In general, lowering the stacking fault energy (SFE) is believed to be an efficient way to promote a high twinning activity, which intrinsic stacking fault energy is commonly in the range of 12 mJ/m² to 55 mJ/m² at room temperature⁴⁻⁹. Due to the importance of deformation twinning associated with strong strain-hardening effect in TWIP steels, how deformation twinning occurs during the plastic deformation has become a focus of recent investigation.

Quite divergent perspectives on the deformation twin nucleation mechanism exist in

the TWIP-steel literature. For example, H. Idrissi et al.¹⁰ mentioned that twin nucleation was attributed to the pole mechanism with a deviation proposed by Cohen and Weertman¹¹ in an Fe-20Mn-1.2C wt.% TWIP steel. The model based on a deviated process mentioned the dissociation of a perfect dislocation into a sessile Frank partial and a glissile Shockley partial when meeting a Lomer-Cottrell barrier, which is more energetically favorable in compared with the pole mechanism proposed by Venable¹² because a very particular dislocations configuration and dislocation dissociation processes are needed for the Venable's model. The reaction of Cohen and Weertman's model is:

$$a/2[101]_{1\bar{1}\bar{1}} = a/3[1\bar{1}1]_{\text{sessile}} + a/6[121]_{1\bar{1}1} \quad (1)$$

On the other hand, based on the direct observation of twin formation, Liu et al.¹³ concluded that a slightly modified version of the Fuji and Mori¹⁴ twinning model could be used to explain their in situ observation in an Fe-24Mn-0.5C wt.% TWIP steel. The key feature of the Fuji and Mori model involves the cross slip of partial dislocation, which dislocation substructure of wide overlapping stacking faults (SFs) on the conjugate planes were observed as following the reaction:

$$a/6[\bar{1}\bar{1}2]_{111} = a/6[2\bar{1}1]_{\bar{1}\bar{1}\bar{1}} + a/6[101]_{\text{stair-rod}} \quad (2)$$

Regardless the model they used to explain their observation, the cross-slip behavior is a common characteristic process between the Cohen-Weertman and the Fuji-Mori twinning model.

In addition, L. Bracke et al.¹⁵ showed that when the tensile axis is close to a <111> crystallographic orientation, such grains tend to deform by twinning followed by the Mahajan and Chin¹⁶ three-layer stacking fault mechanism described by:

$$a/2[1\bar{1}0] + a/2[101] = 3 \times a/6[2\bar{1}1] \quad (3)$$

For Fe-Mn-Si-Al TWIP steels with the SFE ranging from 18 to 23mJ/m², B. Mahato et al.^{17,18} suggested that two twinning mechanisms were prevailing simultaneously, that is, deformation twins were formed on a conjugate {111} plane with generating Shockley partial dislocations by the activation of pole mechanism and Mahajan and Chin three-layer twinning mechanism. Although, twinning mechanisms might alter and probably coexist under different conditions, it could be considered that the formation of deformation twin was relied on dislocation slip.

Only very few researches aimed to study the influence of grain size on twinning behavior. According to the R. Ueji's research¹⁹, it reported that grain refinement has a strong effect on deformation twinning in Fe-31Mn-3Al-3Si TWIP steel. They observed that the number of deformation twins was decreased significantly when the average grain size decreased down to 1.8 μm. Rajib Saha et al.²⁰ further fabricated the fully recrystallized ultrafine-grained (UFG) Fe-31Mn-3Al-3Si TWIP steel with the average grain size of 400 nm; its stress-strain curve showed that the strength and uniform elongation were enhanced simultaneously. It was commonly believed that high-strength UFG materials having single-phase structures always inevitably sacrifice its uniform elongation because of decreases in number of deformation twin but Rajib's result contradicts to this assumption. There are still many details remain unclear regarding the effect of grain size on the TWIP behavior, in particular their influence on twinning mechanism when grain size becomes less than 1 μm. The part of this study, grain size effect on twinning behavior, was investigated in a Fe-31Mn-3Al-3Si TWIP (SFE~40mJ m⁻²) steel subjected to an external stress.

Twinning models proposed in the literatures have something in common that the nucleation of mechanical twin requires achieving sufficient dislocation density and enough

stress to trigger the occurrence of deformation twin. The arrangement of highly coordinated slip of Shockley partials dislocations on $\{111\}$ slip planes appears to be the key feature in the conventional twinning mechanism; however, it seems that the conventional models were proposed without considering the role of grain boundary character. The strong interaction between dislocations and grain boundaries may have occurred at the first place before required dislocation density for twinning in grain interior was achieved. The deformed microstructure near grain boundary, such as the $\Sigma 3$ and high sigma value grain boundaries in a coarse-grained and ultrafine-grained Fe-31Mn-3Al-3Si high manganese steels with $SFE=40\text{mJ/m}^2$ was examined to reveal the correlation between deformation twinning behavior and grain boundary character.

1.1 Research objectives

The objective of this study is to increase the understanding of the deformation twinning behavior when the TWIP steel is subjective to an external stress, through the application of combination of in-situ/ex-situ TEM deformation experiments. The focus of the current study will be on deformation twinning behavior and its underlying mechanisms by considering grain size and grain boundary characters in a Fe-31Mn-3Al-3Si (wt.%) high manganese steel.

(1) Effect of grain size on deformation twinning behavior:

The investigation of the grain size effect on deformation twinning behavior will center on the deformed microstructure of individual grains sized both $>1 \mu\text{m}$ and $\leq 1 \mu\text{m}$ and $> 10 \mu\text{m}$ in conventional coarse-grain counterpart. Main objective of this part is to determine if inhibition of deformation twin nucleation is still applicable at room temperature when the average grain size is refined down to submicron regime. Also, a correlation between macroscopic discontinuous yielding behavior and grain size dependent deformation behavior will be discussed.

(2) Effect of grain-boundary characters on deformation twinning behavior in the coarse-grained steel:

As $\Sigma 3$ boundary has been regarded as a special interface to the materials engineering community, additional attention will be given to them. The response of $\Sigma 3$ boundary to plastic deformation will be directly compared with the response of high-sigma-value grain boundaries counterparts. This observation include: i) dislocations interaction with grain boundary at $\Sigma 3$ boundary, and ii) spontaneously emission of dislocations and stacking faults at high-sigma-value grain boundaries, both of which microstructural features were

examined using ex-/ in-situ deformation TEM.

(3) Microstructural response of $\Sigma 3$ boundary to plastic deformation in UFG TWIP steel:

Although the enhancement of strength and ductility by deformation twinning has been extensively described in conventional coarse-grained TWIP steels, we are not yet able to control the TWIP in UFG metals since the detailed atomistic processes of deformation twinning at grain boundaries have not been well explored. We aim to understand the microstructural response of $\Sigma 3\{111\}$ twin boundary to plastic deformation and its role during the deformation twinning process. The correlation between the local strain level and the localized atomical microstructure was found and discussed using TEM and microprobe STEM based strain mapping techniques.

1.2 Dissertation structure

Chapter 1 addresses the goal and motivation of the present research. Chapter 2 summarizes the background of the TWIP steels including the distinct strain hardening rate and several parameters controlling twin-induced plasticity. Chapter 3 describes grain size altering yielding mechanisms in UFG high-Mn austenitic steel, which has been published in Journal of Materials Science and Technology. Chapter 4 discusses the correlation between grain boundary character and deformation twinning behavior in coarse-grained high-Mn austenitic steel, which has been published in Scientific Reports. Chapter 5 describes the role of $\Sigma 3\{111\}$ twin boundary during deformation twin nucleation in UFG high-Mn austenitic steel, which is now under review in Journal of Material Science and Technology. Chapter 6 summarizes the major conclusions of the present study and how it will be beneficial to the materials science community.

Chapter 2

Background

2.1 Strain hardening of TWIP steel

The exceptional strength-ductility properties that TWIP steel possesses has drew lots of attention in materials science and engineering community for a couple decades. Compared with those formable industrial steels such as Ti-stabalized interstitial-free ferrite steel, TWIP steels exhibit an excellent ultimate strength up to 1 GPa and nearly 50 % uniform elongation. The formability of conventional Ti-stabalized interstitial-free ferrite steel is usually controlled by its crystallographic texture, grain size, and precipitation and can be improved by developing a pronounced $\langle 111 \rangle$ normal direction (ND) fiber texture as well as some limited texture hardening. To attain a higher level of strength, the grain size reduction and precipitation hardening always significantly sacrifice its ductility. **Fig. 2.1** illustrates the stress-strain relationship in a 18Mn-0.6C-1.5Al (wt.%) and an interstitial-free ferrite steel. It is clear to see that TWIP steel exhibits a much higher strain hardening rate, ultimate strength, and uniform elongation (ϵ_u) than those in interstitial-free ferric steel. Note that the strain hardening is defined by the slop of $d\sigma/d\epsilon$. This class of high strength and ductility steel has been developed in automobile industry because it can provide high strength for structural enforcement and its high ductility is expected to ease the press formation. A great energy absorption will improve car crashworthiness which is a big deal for automobile design. These exceptional characteristics are achieved by the combined deformation mechanisms involving dislocation slip, deformation twinning, and a bit of phase transformation ⁴.

Deformation by twinning has been considered to be one of distinct deformation behavior in high-manganese austenitic steel. Deformation twinning behavior taking place in the early

stage of plastic deformation results in high strain hardening rate.

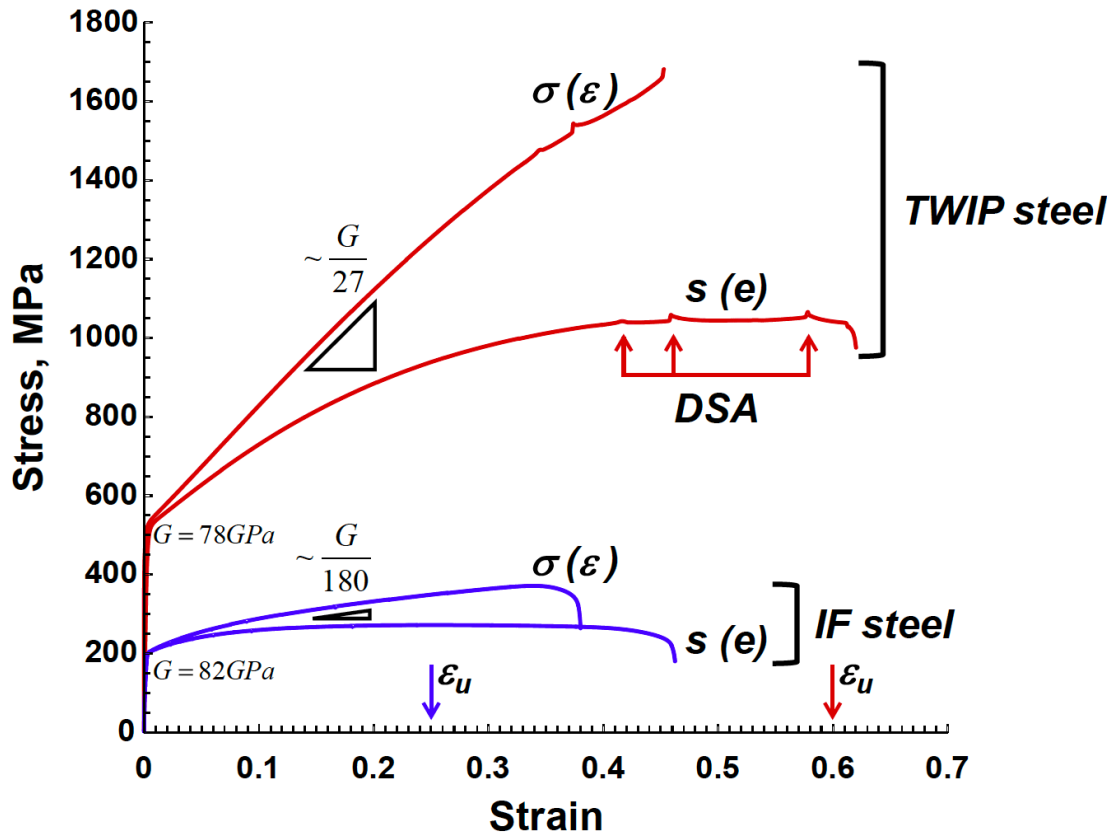


Figure 2.1 The uniaxial tensile stress-strain curves for a Ti-stabilized interstitial-free (IF) ferritic steel (bcc crystal structure) and an Fe-18Mn-0.6C-1.5Al austenitic TWIP steel (fcc crystal structure), illustrating a significant difference in mechanical properties¹. Dynamic strain aging (DSA) regions are indicated by red arrows.

Assessing the twinning mode to plastic strain, Gutierrez-Urrutia and Raabe²¹ and Saeed-Akbari²² et al., who studied Fe-22Mn-0.6C TWIP steel and Fe-(19–27)Mn-(0.3–1.2)-(0.0–3.5)Al TWIP steels, respectively, provide a detailed analysis on the correlation between strain hardening rate and the corresponding microstructural observation. They proposed a detailed interpretation of a five-stages of strain hardening. Their conclusion suggests that deformation twinning has occurred in Stage A (**Fig. 2.2**), different from the view of Kalidindi and co-workers^{23,24} suggesting that no twinning takes place in stage A that dominated by a dislocation dynamic recovery. In fact, Gutierrez-Urrutia²⁵ suggests that the yielding and deformation twinning occur

simultaneously, indicating that the critical resolved shear stress for deformation twinning equals to dislocation gliding. They further argue that the strain hardening in stage B is contributed by the evolution of dislocations assembling to a dislocation cell/wall structure. These dislocation substructures would act as a barrier to dislocation glide. In stage C, the deformation twin becomes very effective to strain hardening due to the dense deformation twin substructure, which are formed by cutting through pre-existing dislocation substructure. Based on the observations, Gutierrez-Urrutia proposed a physical model that accounts for dislocation glide and deformation twinning. They argue that the strain hardening is determined by both the deformation twin spacing and the characteristic length scale of the dislocation substructure.

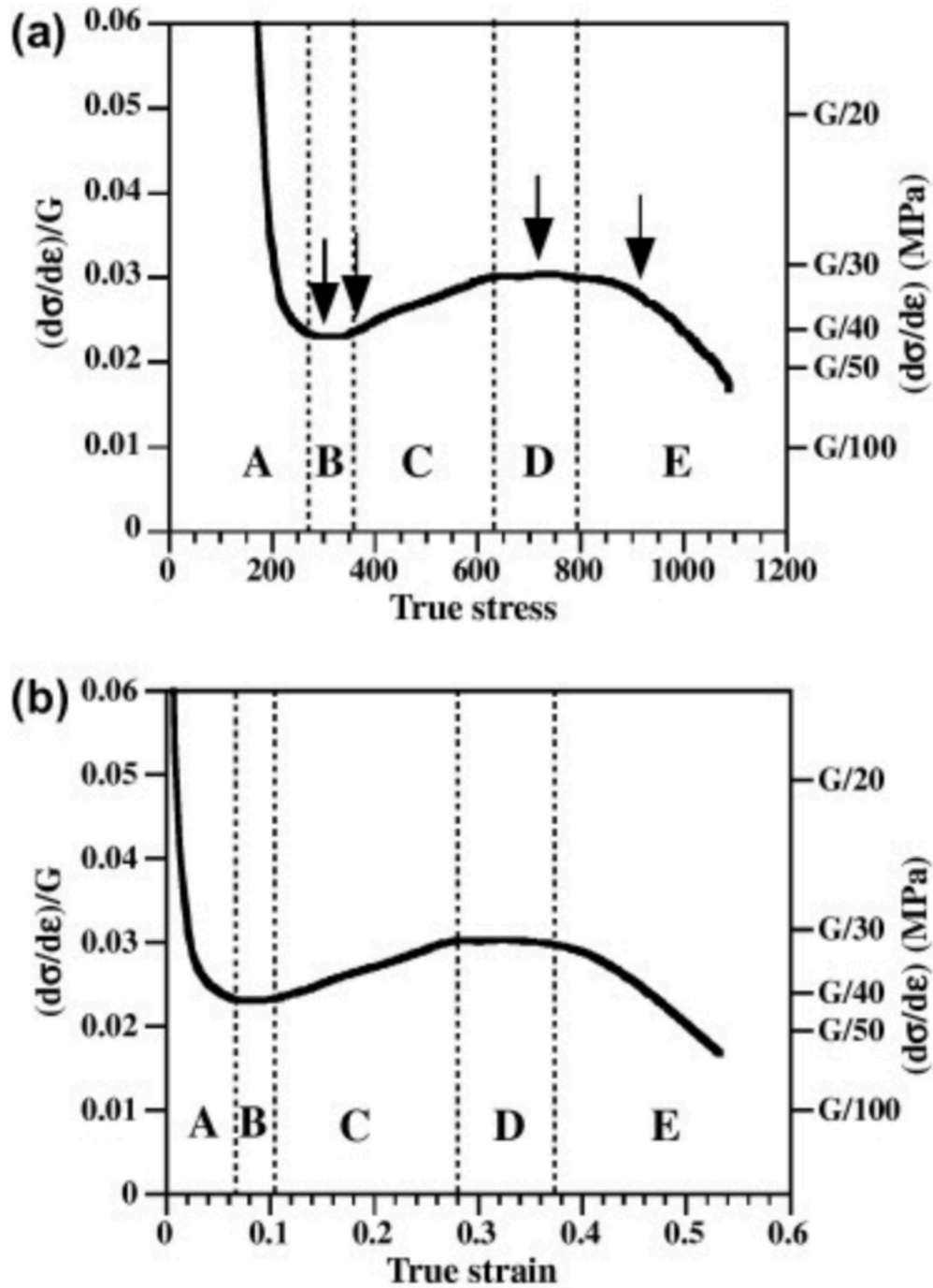


Figure 2.2 Normalized strain hardening rate (normalized by the shear modulus) vs. true stress (a) and true strain (b) of tensile deformed Fe-22 wt. Mn-0.6 wt. C TWIP steel ²¹.

The model proposed by Shiekhelsouk et al.²⁶ shows that at a strain of 15% near 90% grains contains deformation twin. As the sample is further deformed to a strain of 30%, the twin volume fraction still remains low, i.e., 6% twins at strain of 30%. This result is consistent to the previous experimental observation and implies that the total strain of deformation twin to the total strain is very low (3% in 35% strain). However, the formation of deformation twin in the early stage of plastic deformation can indirectly influence the evolution of dislocation substructure by changing the mean free path of dislocations. As a result, the dislocation mean free path decrease as dislocation density increases. The formation of deformation twin in the early true strain of 5% results in the additional reduction of dislocation mean free path. A further factor enhancing the strain hardening is TWIP steels' high dislocation storage capacity due to the strong suppression of cross-slip of dislocations resulting from the low stacking fault energy characteristic. With the considerable advance of the knowledge of TWIP steel, it is generally accepted that the strain hardening in TWIP steel is mainly attributed to “dynamic Hall-Petch effect”²⁷, where grains are progressively subdivided by deformation twins into smaller microstructural entities. Hence, deformation twin can act as a strong barrier to dislocation gliding and provide sufficient rooms for dislocation storage thus enhancing the strain hardening.

2.2 Stacking fault energy in TWIP steel

It has been largely believed that the value of stacking fault energy (SFE) plays a crucial role in controlling the required stress for the formation of deformation twin. In a particular case from a single crystal of low-SFE metal, Venables²⁸ suggests that a parabolic relationship exists between the value of SFE and the twin nucleation stress. Furthermore, many polycrystalline alloys having low-SFE such as 80/20 brass and MP35N exhibit an initiation of deformation twin nucleation under a uniaxial compression test. Although these two alloys show the slightly

different values of SFE, observation suggests that nucleation of deformation twin requires a critical dislocation density. **Fig. 2.3** shows a normalized strain-hardening rate ($(d\sigma/d\varepsilon)/G$) response of alloys under a simple compression stress. The pure copper and 90/10 brass show a typical strain-hardening rate similar to the previous medium- to high- SFE alloys. However, the 316 stainless steel, 70/30 brass, and MP35N having low value of stacking fault energy exhibit a similar strain hardening response and a four-stage strain hardening behavior. **Fig. 2.4 (a)** demonstrates a detailed microstructure from an 80/20 brass deformed to -0.34. The microstructure observed by optical microscopy shows the deformation markings in several grains, which are likely deformation twins. On the other hand, **Fig. 2.4(b)** from the 90/10 brass that does not exhibit the four-stage strain hardening response. These early studies have suggested that the value of the stacking fault energy is mainly controlled by the materials' composition and the deformation behavior (strain hardening response) may directly or indirectly be associated with value of stacking fault energy.

In TWIP steel, several studies have attempted to address the correlation between the value of SFE and deformation mechanisms^{29,30}. However, the reported results could not show a clear relationship because the value of SFE were estimated in different processing method or in different temperature. Kim et al.³¹ and his coworkers present an analysis of the deformation mechanisms and the mechanical properties of Fe-xMn- 0.6C-yAl TWIP steel (wt%) by carefully controlling the variation of Mn and Al. The deformation mechanisms include the dislocation gliding, deformation twinning, or stain-induced martensite. 9 austenitic steel having different composition, SFE and the corresponding mechanical properties are listed in **Table.2.1**. The results suggest that the addition of Mn and Al could increase value of SFE. The detailed microstructural characterizations show that the Fe-15Mn-0.6C-1.5Al, Fe-18Mn-0.6C-1.5Al

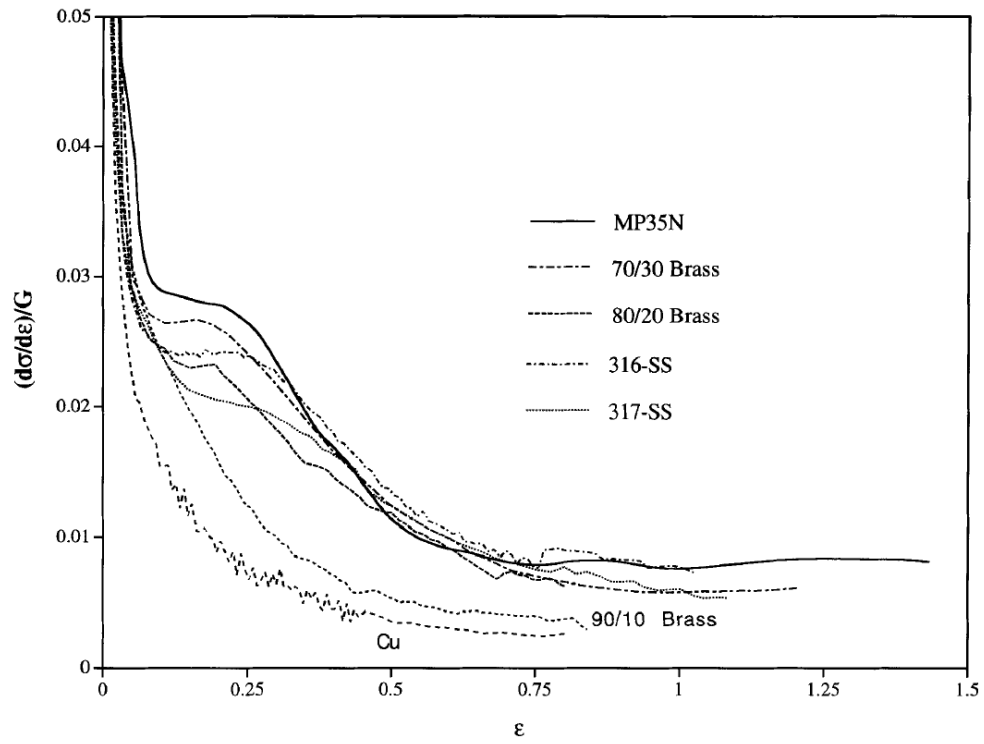
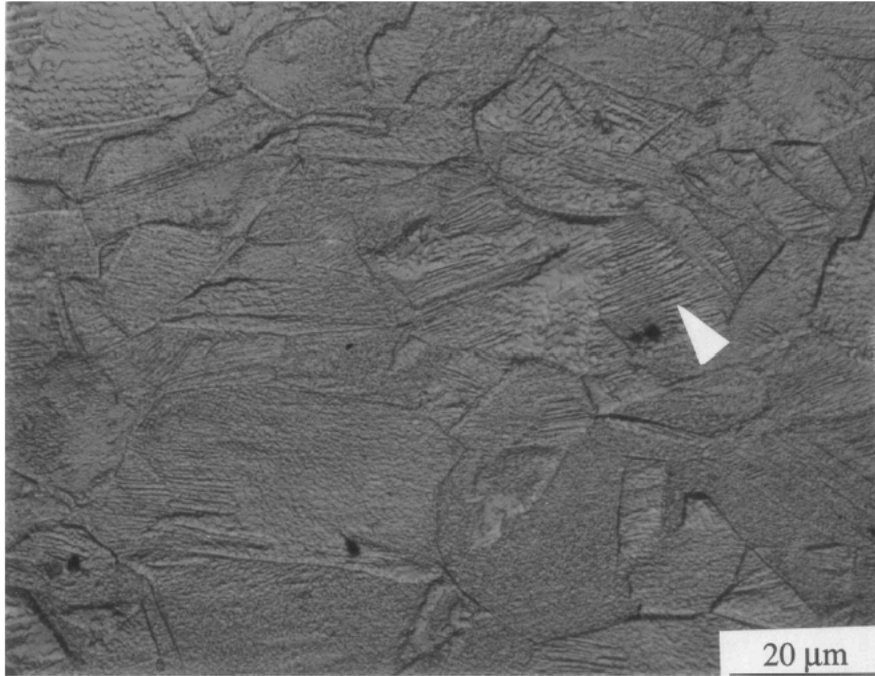
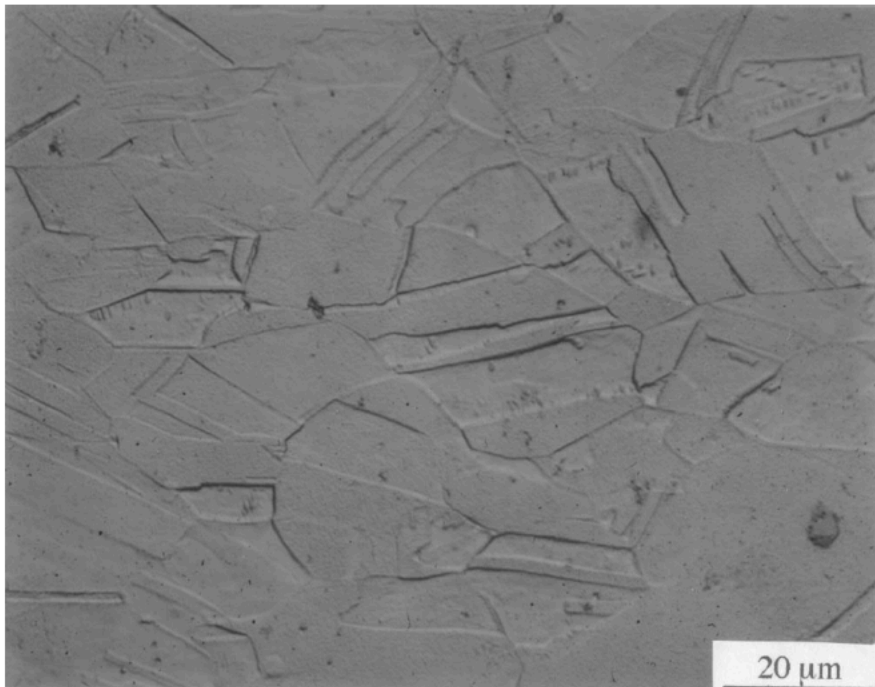


Figure 2.3 Normalized strain hardening rate for several different fcc materials having grain size in a range of 30 μm to 40 μm ³².



(a)



(b)

Figure 2.4 Optical micrographs of the sample deformed to true strain of -0.34 (a) 25 μm 20/80 brass. (b) 30 μm 10/90 brass ³².

, Fe-18Mn-0.6C and Fe-12Mn-0.6C-1.5Al steels demonstrate deformation twinning while the Fe-12Mn-0.6C and Fe-15Mn-0.6C steels show deformation twinning as well as a small amount of strain-induced martensitic transformation. The deformation mechanism appears to be controlled by the SFE which value is highly dependent on their chemical composition. The Schematic in **Fig. 2.5** shows the SFE range for deformation twinning and the strain-induced martensite transformation. The upper limit for strain-induced martensite transformation was estimated to be 13 mJ/m². Therefore, it is possible to allow a TWIP steel having SFE=10-13 mJ/m² to be deformed simultaneously by deformation twinning and martensite transformation. On the other hand, as the SFE can be continuously increased to a level of 50 mJ/m² or more. The dislocation gliding rather than deformation twinning would gradually take over the entire deformation process.

In the contrast to the effect of Al addition to the TWIP steel, the addition of Si has been reported to have an effect of decreasing the value of SFE. Jeong et al.³³ suggest that the SFE decreased by 4 mJ/m² per 1 wt.% Si. The addition of Si also increases yield strength mainly due to solid solution hardening, and high strength owing to maintaining high strain hardening. The decrease in SFE in Si-containing TWIP steel promotes not only the nucleation of primary deformation twin but also the secondary deformation in the early stage of plastic deformation, reflecting a more pronounced strain hardening effect than the one in Fe-18Mn-0.6C TWIP steel counterparts. The relative crystallographic relationship between two deformation twin systems were characterized and analyzed by TEM as shown in **Fig. 2.5**. **Fig. 2.6(a)** indicates that deformation twin was nucleated in the true strain of 0.02 in the Si-containing TWIP having SFE of 13.8 mJ m⁻².

Table 2.1

The overview of the mechanical properties and the values of SFE in the Fe-xMn-0.6C-yAl TWIP steel³¹.

Composition (mass %)	YS (MPa)	UTS (MPa)	Total elon- gation (%)	Critical strain for the onset of serrations (%)	SFE (mJ/m ²)
Fe18Mn0.6C	484.1	1105.6	60.4	2.3	14.25
Fe18Mn0.6C1.5Al	498.3	960.1	59.3	18.6	27.53
Fe18Mn0.6C3Al	498.8	848.9	49.7	24.7	40.12
Fe15Mn0.6C	509.3	1124.1	51.3	1.6	12.38
Fe15Mn0.6C1.5Al	479.5	976.0	57.6	17.1	25.80
Fe15Mn0.6C2Al	488.2	938.9	58.4	18.9	30.12
Fe12Mn0.6C	485.6	837.8	16.1	1.1	11.84
Fe12Mn0.6C1.5Al	491.9	899.5	30.3	17.5	25.52
Fe12Mn0.6C2Al	477.6	914.6	40.7	16.9	29.86

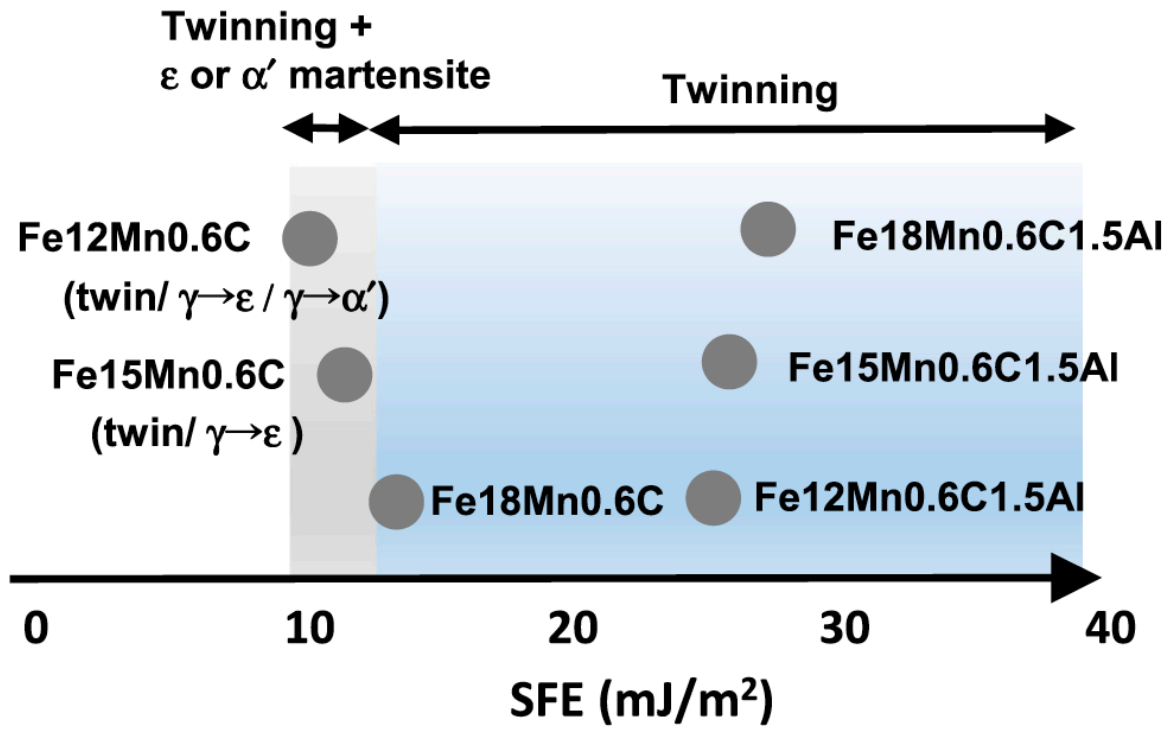


Figure 2.5 Schematic showing the range of SFE for deformation twinning and martensite transformation in the Fe-xMn-yAl TWIP steel³¹.

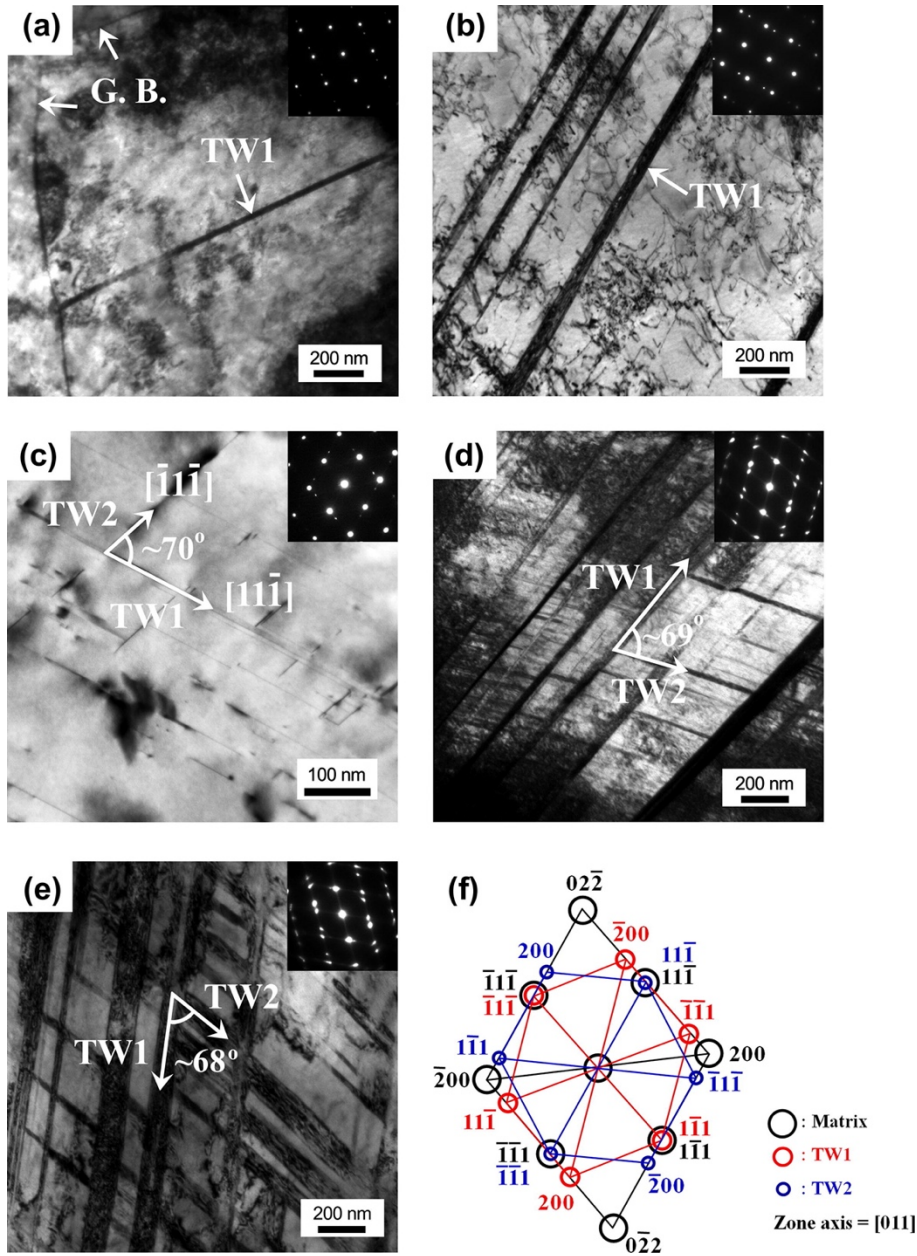


Figure 2.6 Bright-field TEM images of the T618–Si TWIP steel at various true strains of (a) 0.02, (b and c) 0.05, (d) 0.1 and (e) 0.25. TW1, TW2 and G.B. are the primary and secondary mechanical twins and grain boundaries, respectively. The insets of each image show the SAED patterns of the mechanical twins. (f) Index of the SAED patterns of the mechanical twins at a true strain of 0.05³³.

2.3 Effect of geometrical relationship between grain orientation and tensile axis in TWIP steel

Another parameter that will effectively control the deformation twinning process is the grain orientation with respect to the loading direction. The propensity of deformation twinning in grains is strongly dependent on the crystallographic orientation. The initial deformation mode could vary from dislocation slip to the formation of stacking fault, i.e., the deformation mode is controlled by motion of perfect dislocations or Shockley partial dislocations. The ECCI and TEM techniques were employed to characterize the development of deformation twinning behavior in TWIP steels under tensile deformation. I. Gutierrez-Urrutia et al.³⁴ investigate the effect of grain orientation on deformation twinning in a coarse-grained Fe-22Mn-0.6C (wt.%) TWIP steel. The study reported that deformation twinning occurred frequently in grains having $\langle 111 \rangle$ crystallographic direction parallel to the tensile direction, where Schmidt factor for deformation twinning is larger than Schmidt factor for dislocation glide. The inverse pole figure (IPF) in **Fig.2.7(a)**. clearly demonstrates that deformation twins are mostly observed in the $\langle 111 \rangle$ grains parallel to tensile axis in the early stage of plastic deformation. **Fig. 2.7(b)** shows that in the highly deformed steel, most grains show deformation twinning except grains having $\langle 100 \rangle$ orientation.

The grain orientation dependent deformation twinning behavior is commonly explained in terms of Schmidt law²⁶:

$$\tau_{tw} = \sigma \cos\phi \cos\lambda$$

, where $m = \cos\phi \cos\lambda$ is the Schmidt factor, σ is the uniaxial tensile stress, and τ_{tw} corresponded to the resolved shear stress in MPa. When the grains exhibit a Schmidt factor m for twinning is

larger than the m for dislocation gliding, those grains are expected to be strained by deformation twinning.

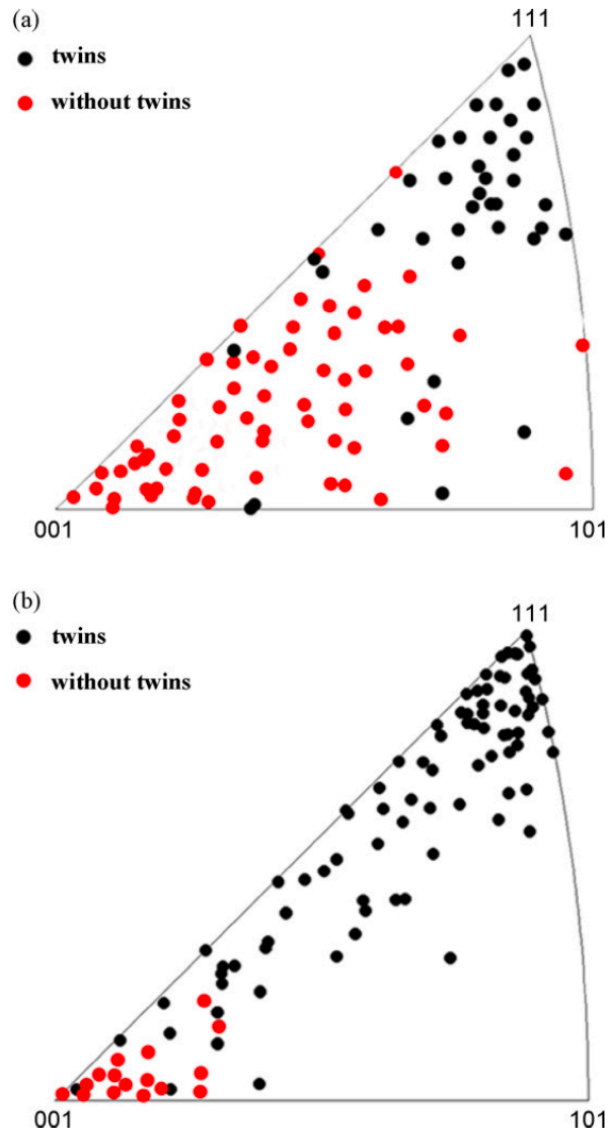


Figure 2.7 Inverse polar figure along tensile axis direction of Fe-22Mn-0.6C (wt.%) TWIP steel with grain size of 50 μm showing grain orientation with deformation twin (black dots) and without deformation twin (red dots): (a) tensile-strained to 0.05 logarithmic strain, (b) tensile-strained to 0.3 logarithmic strain ³⁴.

2.4 Grain size effect in TWIP steel

The formation of deformation twin has been considered to be conducted by dislocation activity which creates an environment for a dislocation-mediated deformation twinning process.

For example, Venables' pole mechanism¹², the Cohen-Weertman deviation process¹¹, or the Mahajan-Chin stacking fault process¹⁶ were proposed based on the highly coordinated dislocation dissociation reaction within multiple {111} slip planes. The critical stress required to initiate nucleation of deformation twin is defined to be twinning stress. Under a tensile deformation, deformation twin tends to nucleate from the grains where their <111> orientation is parallel or nearly parallel to the tensile axis. This orientation dependent deformation twinning behavior suggests that the in-grain dislocation dynamic could play a role in deformation twinning process. Since the dislocation activity was strongly correlated with the grain size, several studies have discussed the effect of grain size on the critical twinning stress. However, Bauziz et al.²⁷ suggest that the nucleation of deformation twin was independent of grain size at least in the grain size range of 1.3-25 μm. The magnitude of the corresponding applied stress is 550 MPa ($\tau_T = 180$ MPa). The conventional twinning theories generally predict the critical resolved shear stress for twinning is proportional to the value of intrinsic stacking fault energy (γ_{isf}):

$$\tau_T = \frac{\gamma_{isf}}{2 \cdot b_p}$$

, where b_p is the Burgers vector of Shockley partial dislocations.

Grain size reduction is generally believed to have a negative effect on nucleation of deformation twin. Meyers et al. proposed a modified equation with a grain-size dependent term:

$$\tau_T = \frac{\gamma_{isf}}{b_p} + \frac{K_T}{\sqrt{D}}$$

, where D is the grain diameter.

The influence of grain size on the critical resolved shear stress has not been entirely understood yet, but I. Gutierrez-Urrutia reported that the critical resolved shear stress increase with the grain size reduction in a Fe-22Mn-0.6C (wt.%) TWIP steel having average size in the

range of 3~50 μm . Ueji et al.¹⁹ show that nucleation of deformation twin becomes difficult in a Fe-31Mn-3Al-3Si (wt.%) TWIP steel with average grain size $\sim 1.8 \mu\text{m}$. **Fig. 2.8** indicates that (1) deformation twin can be found in the grains where $\langle 111 \rangle$ orientation is close to the tensile axis in coarse-grained sample. (2) The deformation twins are rarely observed even in the $\langle 111 \rangle$ grain//tensile axis. The deformation twinning behavior appear to be significantly suppressed in the few-micron grain size regime.

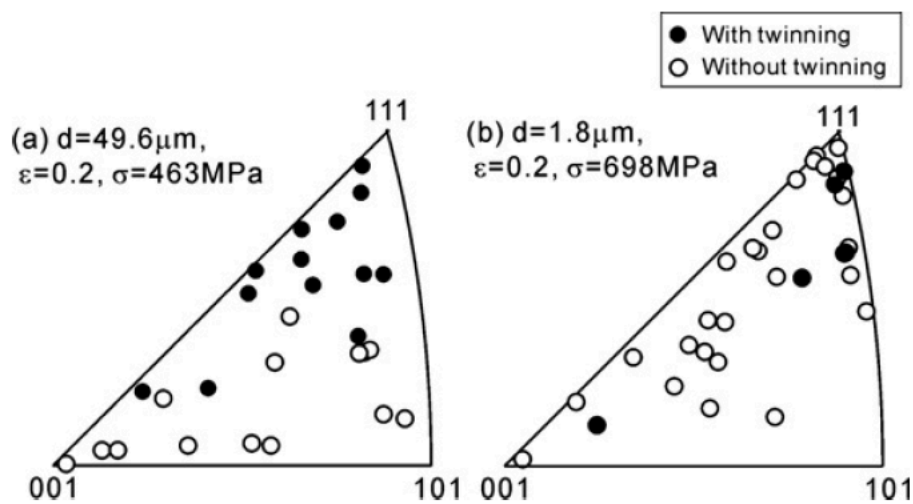


Figure 2.8 Inverse pole figures showing the crystallographic orientation dependences of the deformation twinning. Data point indicates the orientation of the grains parallel to tensile axis. Filled/open marks denote with/without twinning, respectively¹⁹.

References

1. De Cooman, B. C., Estrin, Y. & Kim, S. K. Twinning-induced plasticity (TWIP) steels. *Acta Mater.* **142**, 283–362 (2018).
2. Vercammen, S., Blanpain, B., De Cooman, B. C. C. & Wollants, P. Cold rolling behaviour of an austenitic Fe-30Mn-3Al-3Si TWIP-steel: The importance of deformation twinning. *Acta Mater.* **52**, 2005–2012 (2004).
3. Bouaziz, O., Allain, S., Scott, C. P., Cugy, P. & Barbier, D. High manganese austenitic twinning induced plasticity steels: A review of the microstructure properties relationships. *Curr. Opin. Solid State Mater. Sci.* **15**, 141–168 (2011).
4. Allain, S., Chateau, J.-P. & Bouaziz, O. A physical model of the twinning-induced plasticity effect in a high manganese austenitic steel. *Mater. Sci. Eng. A* **387–389**, 143–147 (2004).
5. Rémy, L. The interaction between slip and twinning systems and the influence of twinning on the mechanical behavior of fcc metals and alloys. *Metall. Trans. A* **12**, 387–408 (1981).
6. Remy, L. & Pineau, A. Twinning and strain-induced F.C.C. → H.C.P. transformation in the FeMnCrC system. *Mater. Sci. Eng.* **28**, 99–107 (1977).
7. Lee, T.-H., Shin, E., Oh, C.-S., Ha, H.-Y. & Kim, S.-J. Correlation between stacking fault energy and deformation microstructure in high-interstitial-alloyed austenitic steels. *Acta Mater.* **58**, 3173–3186 (2010).
8. Pierce, D. T. *et al.* The influence of manganese content on the stacking fault and austenite/ ϵ -martensite interfacial energies in Fe–Mn–(Al–Si) steels investigated by experiment and theory. *Acta Mater.* **68**, 238–253 (2014).

9. Pierce, D. T., Jiménez, J. A., Bentley, J., Raabe, D. & Wittig, J. E. The influence of stacking fault energy on the microstructural and strain-hardening evolution of Fe–Mn–Al–Si steels during tensile deformation. *Acta Mater.* **100**, 178–190 (2015).
10. Idrissi, H., Renard, K., Ryelandt, L., Schryvers, D. & Jacques, P. J. On the mechanism of twin formation in Fe–Mn–C TWIP steels. *Acta Mater.* **58**, 2464–2476 (2010).
11. Cohen, J. B. & Weertman, J. A dislocation model for twinning in f.c.c. metals. *Acta Metall.* **11**, 996–998 (1963).
12. Venables, J. A. On dislocation pole models for twinning. *Philos. Mag.* **30**, 1165–1169 (1974).
13. Liu, J. B., Liu, X. H., Liu, W., Zeng, Y. W. & Shu, K. Y. Transmission electron microscopy observation of a deformation twin in TWIP steel by an ex situ tensile test. *Philos. Mag.* **91**, 4033–4044 (2011).
14. Fujita, H. & Mori, T. A formation mechanism of mechanical twins in F.C.C. Metals. *Scr. Metall.* **9**, 631–636 (1975).
15. Bracke, L., Kestens, L. & Penning, J. Direct observation of the twinning mechanism in an austenitic Fe-Mn-C steel. *Scr. Mater.* **61**, 220–222 (2009).
16. Mahajan, S. & Chin, G. Y. Formation of deformation twins in f.c.c. crystals. *Acta Metall.* **21**, 1353–1363 (1973).
17. B. Mahato *et al.* Simultaneous twinning nucleation mechanisms in an Fe–Mn–Si–Al twinning induced plasticity steel. *Acta Mater.* **132**, 264–275 (2017).
18. Mahato, B. *et al.* Simultaneous twinning nucleation mechanisms in an Fe–Mn–Si–Al twinning induced plasticity steel. *Acta Mater.* **132**, 264–275 (2017).

19. Ueji, R. *et al.* Tensile properties and twinning behavior of high manganese austenitic steel with fine-grained structure. *Scr. Mater.* **59**, 963–966 (2008).
20. Saha, R., Ueji, R. & Tsuji, N. Fully recrystallized nanostructure fabricated without severe plastic deformation in high-Mn austenitic steel. *Scr. Mater.* **68**, 813–816 (2013).
21. Gutierrez-Urrutia, I. & Raabe, D. Dislocation and twin substructure evolution during strain hardening of an Fe–22 wt.% Mn–0.6 wt.% C TWIP steel observed by electron channeling contrast imaging. *Acta Mater.* **59**, 6449–6462 (2011).
22. Saeed-Akbari, A., Mosecker, L., Schwedt, A. & Bleck, W. Characterization and Prediction of Flow Behavior in High-Manganese Twinning Induced Plasticity Steels: Part I. Mechanism Maps and Work-Hardening Behavior. *Metall. Mater. Trans. A* **43**, 1688–1704 (2012).
23. Asgari, S., El-Danaf, E., Kalidindi, S. R. & Doherty, R. D. Strain hardening regimes and microstructural evolution during large strain compression of low stacking fault energy fcc alloys that form deformation twins. *Metall. Mater. Trans. A* **28**, 1781–1795 (1997).
24. Kocks, U. F. & Mecking, H. Physics and phenomenology of strain hardening: the FCC case. *Prog. Mater. Sci.* **48**, 171–273 (2003).
25. Gutierrez-Urrutia, I., Zaefferer, S. & Raabe, D. The effect of grain size and grain orientation on deformation twinning in a Fe–22wt.% Mn–0.6wt.% C TWIP steel. *Mater. Sci. Eng. A* **527**, 3552–3560 (2010).
26. SHIEKHEL SOUK, M., FAVIER, V., INAL, K. & CHERKA OUI, M. Modelling the behaviour of polycrystalline austenitic steel with twinning-induced plasticity effect.

- Int. J. Plast.* **25**, 105–133 (2009).
27. Bouaziz, O., Allain, S. & Scott, C. Effect of grain and twin boundaries on the hardening mechanisms of twinning-induced plasticity steels. *Scr. Mater.* **58**, 484–487 (2008).
 28. Venables, J. . The nucleation and propagation of deformation twins. *J. Phys. Chem. Solids* **25**, 693–700 (1964).
 29. Frommeyer, G., Brüx, U. & Neumann, P. Supra-ductile and high-strength manganese-TRIP/TWIP steels for high energy absorption purposes. *ISIJ Int.* **43**, 438–446 (2003).
 30. Dumay, A., Chateau, J. P., Allain, S., Migot, S. & Bouaziz, O. Influence of addition elements on the stacking-fault energy and mechanical properties of an austenitic Fe-Mn-C steel. *Mater. Sci. Eng. A* (2008) doi:10.1016/j.msea.2006.12.170.
 31. Kim, J. K. & De Cooman, B. C. Stacking fault energy and deformation mechanisms in Fe-xMn-0.6C-yAl TWIP steel. *Mater. Sci. Eng. A* **676**, 216–231 (2016).
 32. El-Danaf, E., Kalidindi, S. R. & Doherty, R. D. Influence of grain size and stacking-fault energy on deformation twinning in fcc metals. *Metall. Mater. Trans. A* **30**, 1223–1233 (1999).
 33. Kang, S., Lee, Y.-K., Jin, J.-E., Jung, Y.-S. & Jeong, K. The effects of Si on the mechanical twinning and strain hardening of Fe–18Mn–0.6C twinning-induced plasticity steel. *Acta Mater.* **61**, 3399–3410 (2013).
 34. Gutierrez-Urrutia, I., Zaefferer, S. & Raabe, D. The effect of grain size and grain orientation on deformation twinning in a Fe-22wt.% Mn-0.6wt.% C TWIP steel. *Mater. Sci. Eng. A* (2010) doi:10.1016/j.msea.2010.02.041.

Chapter 3

Grain size altering yielding mechanisms in ultrafine grained high-Mn austenitic steel: advanced TEM investigations

Chang-Yu Hung^{a,*}, Yu Bai^b, Nobuhiro Tsuji^{b,c}, Mitsuhiro Murayama^{a,d*}

^a Department of Materials Science and Engineering, Virginia Tech, Blacksburg, VA 24061, USA

^b Department of Materials Science and Engineering, Kyoto University, Yoshidahonmachi, Sakyo-ku, Kyoto 606-8501, Japan

^c Elements Strategy Initiative for Structural Materials, Kyoto University, Yoshidahonmachi, Sakyo-ku, Kyoto 606-8501, Japan

^d Institute for Materials Chemistry and Engineering, Kyushu University, Kasuga, Fukuoka 8168580, Japan

This chapter has been published in Journal of Materials Science and Technology, 2021, Volume 86, Pages 192-203. <https://doi.org/10.1016/j.jmst.2021.01.031>

Abstract

The underlying mechanism of discontinuous yielding behavior in an ultrafine-grained (UFG) Fe-31Mn-3Al-3Si (wt.%) austenitic TWIP steel was investigated by the use of advanced TEM technique with taking the plastic deformation mechanisms and their correlation with grains size near the macroscopic yield point into account. Typical yield drop mechanisms such as the dislocation locking by the Cottrell atmosphere due to the presence of interstitial impurities cannot explain the origin of this phenomenon in the UFG high-Mn austenitic TWIP steel. Here, we experimentally revealed that the plastic deformation mechanisms in the early stage of deformation, around the macroscopic yield point, show an obvious association with grain size. More specifically, the main mechanism shifts from the conventional slip in grain interior to twinning nucleated from grain boundaries with decreasing the grain size down to less than 1 μm . Our observation indicates that the grain size dependent deformation mechanisms transition is also deeply associated with the discontinuous yielding behavior as it could govern the changes in the grain interior dislocation density of mobile dislocations around the macroscopic yield point.

3.1 Introduction

High-Mn austenitic twinning-induced plasticity (TWIP) steels aiming to achieve high strength - large ductility balance have been developed for last two decades¹⁻³. High deformation twinning activity is commonly observed when the stacking fault energy (SFE) of a TWIP steel is in the range of 12-55 mJ·m⁻² at room temperature⁴⁻⁹. Currently, deformation twins are considered to be responsible to strain hardening rate enhancement, the key factor to gain a high strength - large ductility balance, because deformation twins can act as strong obstacles to dislocation movement thus leading to a strong strain hardening effect. Therefore, the majority of studies regarding the strain hardening effect have been conducted based on the dislocation mean free path approach⁹⁻¹⁵, although the details of underlying mechanism of the strain hardening have still not been fully understood yet.

So far, the low yield strength of high-Mn austenitic TWIP steels due to their face centered cubic (FCC) structure limits their practical application. To improve the yield strength without changing chemical composition, grain refinement techniques have been applied and achieving the early success¹⁶⁻²³. A series of studies in the mechanical properties of a UFG high-Mn TWIP steel having fully recrystallized austenite microstructure and the average grain size smaller than 1 μm^{20,24,25} have reported that the stress-strain curve of this steel exhibits both high strength and large tensile ductility. Interestingly the UFG TWIP steel also shows the discontinuous yielding characterized by obvious yield-drop instead of the continuous yielding normally observed in FCC metals and alloys. It is known that the discontinuous yielding is not uniquely observed in this UFG TWIP steel, but it rather commonly occurs in UFG materials regardless of the crystal structure and chemical composition²⁶⁻²⁸. Nevertheless, investigations in the underlying

mechanisms of the discontinuous yielding accompanied with yield-drop in UFG metals, especially interstitial free metals and alloys, are still ongoing. For example, Bai et al. [16] is proposing that the reason for the discontinuous yielding in the UFG Fe-31Mn-3Al-3Si TWIP steel is attributable to the lack of dislocations in each recrystallized ultrafine grain, which can be consistent to the enhanced deformation twinning.

In contrast to the yield strength improvement, finer grain size is known to make deformation twinning in FCC materials less frequent²⁹ and it also likely lower the tensile ductility³⁰. Ueji et al.¹⁸ and Gutierrez-Urrutia et al.³¹ reported that grain refinement has a suppressing effect on deformation twinning in TWIP steel. Gutierrez-Urrutia et al. examined a Fe-22Mn-0.6C (SFE $\sim 22 \text{ mJ}\cdot\text{m}^{-2}$) TWIP steel and concluded that deformation twinning becomes less frequent but is not fully inhibited with decreasing the average grain size down to 3 μm . Ueji et al. observed that the number of deformation twins is decreased significantly with decreasing the average grain size to 1.8 μm in a Fe-31Mn-3Al-3Si (SFE $\sim 40 \text{ mJ}\cdot\text{m}^{-2}$) TWIP steel. It is estimated that the deformation twinning inhibition by grain refinement is less significant in a lower SEF steel by comparing these two cases. On the other hand, Bai, Kitamura, and Tsuji et al.^{16,17,32} recently demonstrated that the deformation twin nucleation from grain boundaries in a ultrafine grained (UFG) Fe-31Mn-3Al-3Si TWIP steel is rather enhanced by grain refinement when the grain size becomes less than 1 μm .

Concerning the deformation twin nucleation mechanisms in conventional coarse grained high-Mn austenitic TWIP steels, multiple mechanisms have been proposed based on microstructure investigations by transmission electron microscopy (TEM). In brief, Idrissi et al.³³ observed a high density of sessile Frank dislocations within deformation twins in a Fe-20Mn-1.2C TWIP steel and concluded that the deformation twin nucleation is attributed

to the pole mechanism proposed by Cohen and Weertman ³⁴ with a deviation. The dislocation reaction of the Cohen - Weertman model is:

$$\frac{a}{2}[101]_{\bar{1}\bar{1}\bar{1}} = \frac{a}{3}[1\bar{1}1]_{\text{sessile}} + \frac{a}{6}[121]_{\bar{1}\bar{1}\bar{1}} \quad (1)$$

Liu et al. ³⁵ concluded that a slightly modified version of the Fujita and Mori ³⁶ deformation twinning model can explain the nucleation of deformation twins in a 24Mn-0.5C TWIP steel. The Fujita - Mori model involves a cross slip of piled-up partial dislocation, which is expressed by:

$$\frac{a}{6}[\bar{1}\bar{1}2]_{111} = \frac{a}{6}[\bar{2}\bar{1}1]_{\bar{1}\bar{1}\bar{1}} + \frac{a}{6}[101]_{\text{stair-rod}} \quad (2)$$

Bracke et al. ³⁷ showed that grains having its $\langle 111 \rangle$ crystallographic orientation close to the tensile axis are likely deformed by twinning followed by the Mahajan - Chin ³⁸ three-layer stacking fault mechanism:

$$\frac{a}{2}[1\bar{1}0] + \frac{a}{2}[101] = 3 \times \frac{a}{6}[2\bar{1}1] \quad (3)$$

In the carbon free Fe-Mn-Si-Al alloy system, while Mahato et al. ^{39,40} suggested that two dissimilar mechanisms, the pole mechanism and the Mahajan - Chin three-layer mechanism, cooperate simultaneously; Idrissi et al. ⁴¹ claimed that the Fujita - Mori cross-slip mechanism is mandatory for the deformation twin nucleation. This argument suggests that the operative twin nucleation mechanism(s) might be affected by local environment including alloy chemistry, but local environmental factors changing the dominancy were not well documented. On the other hand, a sufficient dislocation density in the grain interior and a local stress concentration around the nucleation site seem to be the essential prerequisites to trigger the deformation twin nucleation for all these proposed mechanisms.

It is expected that in-grain dislocation sources would not be active in the UFG high-Mn austenitic TWIP steels due to the grain size constraint. Then, these deformation twin

nucleation mechanisms for conventional coarse-grained materials may not be directly applicable. As mentioned above, contradicting reports whether smaller grain size suppressing or enhancing the deformation twinning nucleation imply that the grain size effect on deformation twinning in UFG TWIP steels could be very size-sensitive if exists, and the grain size around $1\mu\text{m}$ is likely the tipping point. In fact, a microstructural observation using electron channeling contrast imaging in a scanning electron microscope (SEM-ECCI) by Bai et al.^{16,32} suggests that the deformation twinning nucleation mainly occurred at grain boundaries instead of the grain interior.

In summary, the plastic deformation behavior of UFG high-Mn TWIP steels and its governed mechanisms are expected to have a grain size dependence, and these may be different from the governed mechanisms in the conventional grain sized counterparts. Therefore, the aim of this study is to investigate the underlying mechanism of discontinuous yielding behavior in an UFG Fe-31Mn-3Al-3Si TWIP steel (the average grain size $0.79 \pm 0.39\ \mu\text{m}$) with taking particular attention to the deformed microstructures in around $1\mu\text{m}$ size grains at the near-yielding strain level (engineering strain = 0.02, 0.03, 0.046, 0.062). The plastic deformation behavior in a conventional coarse-grained counterpart (the average grain size $15.4 \pm 5.2\ \mu\text{m}$) will be compared to gain a better understanding of the plastic deformation mechanisms in the early stage of deformation, and their potential correlation with the grain size.

3.2 Materials and Experimental Methods

3.2.1 Sample fabrication

TWIP steel samples with two different grain sizes, $15.4 \pm 5.2\ \mu\text{m}$ and $0.79 \pm 0.39\ \mu\text{m}$, were fabricated for this study. The chemical composition of the steel was Fe-31Mn-3Al-3Si

wt.%. First, as-received TWIP steel was rolled from 12 mm to 1 mm (92% reduction) by multi-pass cold rolling. Second, further annealing processes were carried out in a salt bath at 950°C for 15 minutes (coarse-grained) and at 700°C for 5 minutes (UFG) followed by water cooling.

3.2.2 Electron backscattered diffraction characterization

After cold rolling and annealing, the microstructural features including grain boundary maps and local texture were examined using a FEI Helios 600 equipped with a TSL OIM EBSD system. The EBSD maps were measured at 30 kV acceleration voltage and 13 mm working distance. The coarse- and ultrafine-grained steels were scanned with step size of 1500 nm and 50 nm, respectively. Due to the statistical significance of grain boundary information, the larger step size was used for coarse-grained steel in order to take as many as grain boundaries into account. No data clean-up was performed except for the removal of some points with low confidence value.

3.2.3 Uniaxial tensile test

Sheet-type tensile test specimens with a gauge length of 10 mm and width of 5 mm were used for uniaxial tensile tests at room temperature for evaluating mechanical properties of the recrystallized specimens. The sheet-type tensile samples were then sliced to a specific dimension, 13 × 2 mm rectangular plate, and mechanically thinned to approximately 150 μm thick for the deformed microstructure characterization by TEM. The coarse-grained steels were tensile-deformed to 0.02 engineering strain using a testing machine (Kammrath and Weiss Module 5000 N) at a strain rate of $4.6 \times 10^{-4} \text{ s}^{-1}$ at room temperature while the ultrafine-grained steels were strained individually to 0.03, 0.046 and 0.062 engineering strains with the above strain rate and temperature.

3.2.4 Transmission electron microscopy characterization

Samples prepared for TEM analyses were cut from the center of the deformed samples, 2×2 mm square-shape foil, and then mechanically thinned to 70 μm thick. Thinning to electron transparency was achieved by using a twin-jet electropolisher (Fischione Model 110) with a 95% acetic acid - 5% perchloric acid electrolyte maintained at 17°C and the applied voltage of 38 V. The transmission electron microscopy characterization was performed using a JEOL 2100 TEM operated at 200 kV with Gatan Orius 200D and Ultrascan 1000XP cameras.

3.3 Results

To demonstrate the representative mechanical property of the UFG and coarse-grained sample, an engineering stress-strain curve obtained from room temperature tensile test is shown in **Fig. 3.1**^{17,32}. The curve represents that the UFG TWIP steel showed a high yield strength (upper yield strength) of 633 MPa and a large elongation of 60%, and a discontinuous yielding characterized by a clear yield-drop. It is worth noting that the coarse-grained sample with a yield strength of 245 MPa exhibits continuous yielding that is typical for FCC alloys.

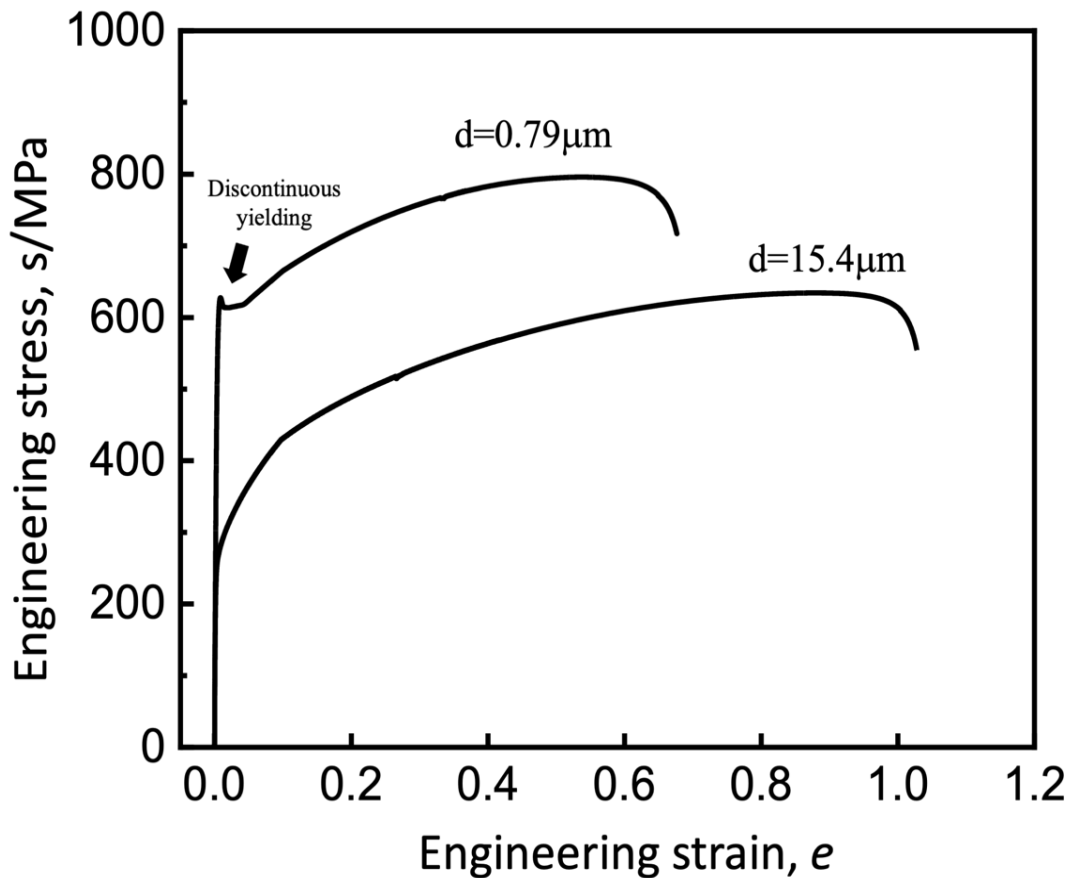


Figure 3.1 An engineering stress-strain curve of Fe-31Mn-3Al-3Si having 0.79 μm and 15.4 μm grain size. The discontinuous yielding characterized by a clear yield drop is indicated by a black arrow.

3.3.1 Pre-straining microstructure characterization

The representative microstructures of coarse-grained and UFG samples were shown in **Fig. 3.2**, indicating that the microstructure of the both steels were fully recrystallized and composed of single austenite phase. The grain boundary maps of the pre-straining samples graphically indicated the misorientation angles in **Fig. 3.2(a, b)**; high-angle boundaries, higher than 15° , and annealing twin boundaries, known as $\Sigma 3$ coherent boundary, are specified by red and green colors. Both samples showed a fully recrystallized microstructure with a high ratio of high-angle boundaries. It is worth mentioning that the majority of the boundaries are the annealing twin boundary and its ratio is more than 30% of the total (0.3

out of 1) as indicated in **Fig. 3.2**(c, d). EBSD was also used to confirm the average grain size including annealing twins; the average grain size with standard deviation of two samples are $15.4 \pm 5.2 \mu\text{m}$ and $0.79 \pm 0.39 \mu\text{m}$, respectively. The grain size distribution is quite homogeneous in both samples opposing to some earlier results reported bimodal microstructures⁴²⁻⁴⁴. The reconstructed stereographic triangle (inverse pole figure – IPF map) was calculated by the harmonic method through the OIM analysis software. The IPF map indicated that the frequency of occurrence of the crystal orientation parallel to the rolling direction (RD), i.e., the maximum texture intensity (I_{max}) for ultrafine-grained sample was slightly higher than that of the coarse-grained counterpart (**Fig. 3.2**(e-f)). It should be noted that the maximum texture intensity (I_{max}) of both steels were low, although relatively stronger $\{111\}$ and $\{001\}$ fibers oriented along RD are present. No well-developed texture was observed.

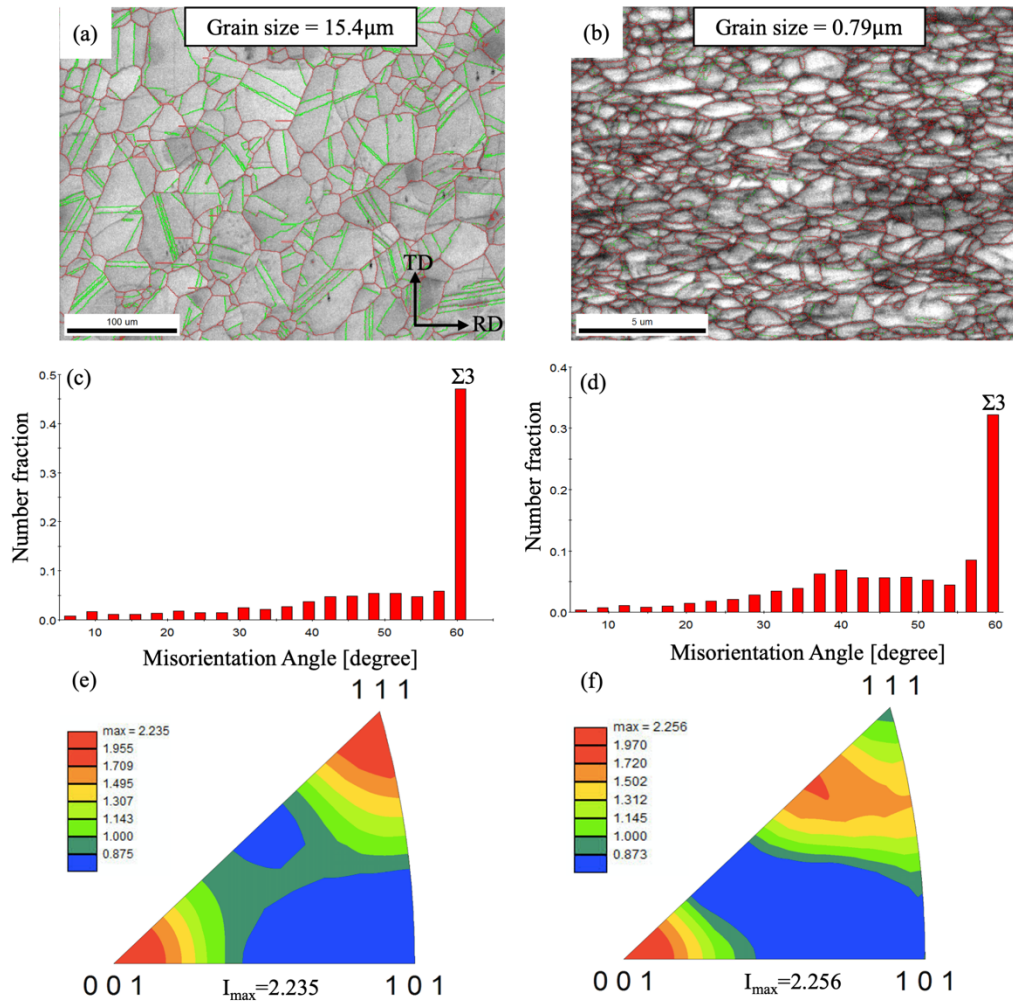
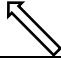







Figure 3.2 EBSD maps of fully recrystallized coarse-grained and UFG- samples: (a-b) grain boundary map, (c-d) misorientation distribution histogram, (e-f) grain orientation distribution in the rolling direction. (a), (c), and (e) are from the coarse-grained ($15.4 \pm 5.2 \mu\text{m}$) sample; (b), (d), and (f) are from the UFG ($0.79 \pm 0.39 \mu\text{m}$) sample. Red lines in (a-b) represent high angle boundaries with rotation angle (θ), $15^\circ \leq \theta < 60^\circ$, and green lines represent $\Sigma 3$ boundaries. The number fraction in (c-d) is defined as the ratio of a certain grain boundary to total number of the grain boundaries such as 0.45 (out of 1.0) for $\Sigma 3$ boundaries in the coarse-grained sample, 0.3 for $\Sigma 3$ boundaries in the UFG sample. The maximum texture intensity is relatively small for both samples (e, f) indicating that no strong texture is present.

Table 3.1 List of symbols used in TEM images

Symbol	Description
	g-vector direction
	streak (in electron diffraction pattern)
	dislocation gliding direction
	stacking fault
	twin boundary
	dislocation

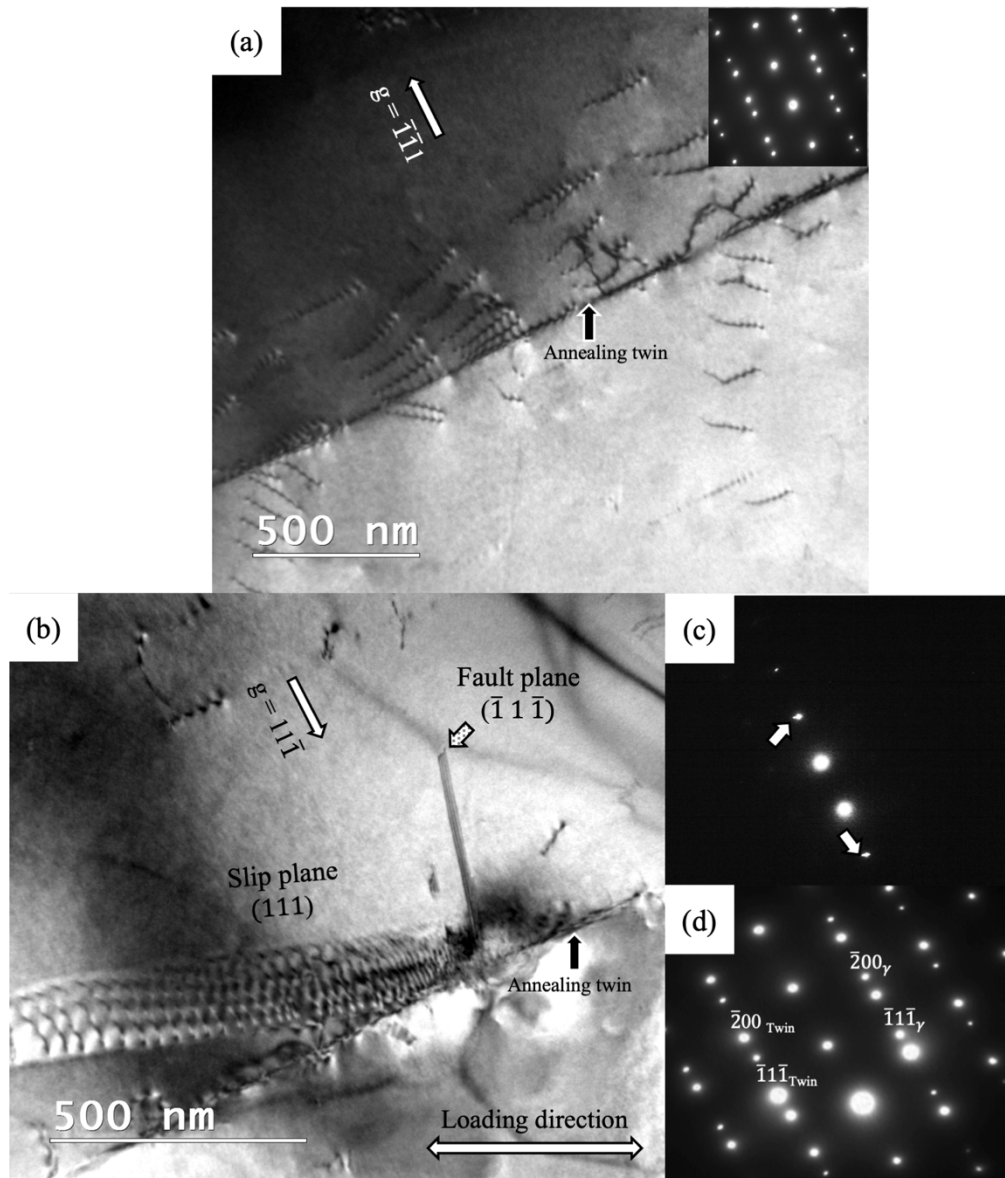


Figure 3.3 Bright field (BF) TEM images show the microstructures and defects in the coarse-grained sample deformed to engineering strain = 0.02. (a) planar array of dislocations gliding and generating slip transfers across an annealing twin boundary, taken in a two-beam condition with the operative reflection g_{111} . Some dislocations cross-slipped on the annealing twin boundary are indicated by black arrow. (b) Piled-up dislocations being impinged on a twin boundary, taken in a two-beam condition with the operative reflection $g_{11\bar{1}}$. (c) A selected area electron diffraction (SAED) pattern from the upper grain showing a streak contrast due to the shape factor of the planar fault. (d) A SAED pattern from the twin boundary. The diffraction spots of the matrix and twin were indexed according to $[011]_{fcc}$ zone axis.

3.3.2 Deformation microstructure characterization

Symbols used in TEM images hereafter are listed in Table 3.1. Each of symbols indicates the direction of g-vector excited to image, streak in electron diffraction pattern, dislocation gliding direction, stacking faults, and twins.

3.3.2.1 Coarse-grained TWIP steel: deformed to 0.02 engineering strain

A bright field (BF) TEM image of **Fig. 3.3(a)** illustrates planar array of dislocations gliding and generating slip transfers across an annealing twin boundary. Slip transfer across grain boundary could take place when the line of intersection that incoming and outgoing slip plane make with grain boundary is colinear and the Burgers vectors of screw dislocations of incoming and outgoing system are identical⁴⁵. This slip transfer reaction is not commonly observed in the present work. On the other hand, it was found that the slip transfer across the annealing twin boundary in **Fig. 3.3(a)** appeared different from that in **Fig. 3.3(b)**. **Fig. 3.3(b)** shows the piled-up dislocations being impinged on an annealing twin boundary (labeled “Annealing twin”) and a planar defect (arrow filled with dots) nucleated from the area near the grain boundary into the original crystal. These two BF TEM images were taken at a two-beam condition with the operative reflection (a) $g_{\bar{1}\bar{1}1}$ and (b) $g_{11\bar{1}}$, respectively. Thus, the slip plane and fault plane in **Fig. 3.3(b)** were identified to be (111) and $(\bar{1}\bar{1}\bar{1})$, and the annealing twin plane was $(\bar{1}\bar{1}1)$, which was confirmed by a selected area electron diffraction pattern (SAED) taken from a $[011]_{fcc}$ zone axis (**Fig. 3.3(d)**). Due to the shape factor of the planar defect in **Fig. 3.3(b)**, a set of weak streaks were found in a SAED pattern taken from the corresponding area (**Fig. 3.3(c)**). The fringe contrast observed in **Fig. 3.3(b)** and streaks in the SAED pattern suggest that the most possible candidate for this planar defect is a stacking fault, which could be induced by a

local stress field associated with piled-up dislocations impinged on the annealing twin boundary.

In order to understand the dislocation reaction resulting in the stacking faults formation in **Fig. 3.3(b)**, the nature of dislocations near annealing twin boundaries was characterized by two-beam analysis ($\mathbf{g} \cdot \mathbf{b}$ criterion) using multiple diffraction conditions near a $[011]_{\text{fcc}}$ zone axis as shown in **Fig. 3.4**.

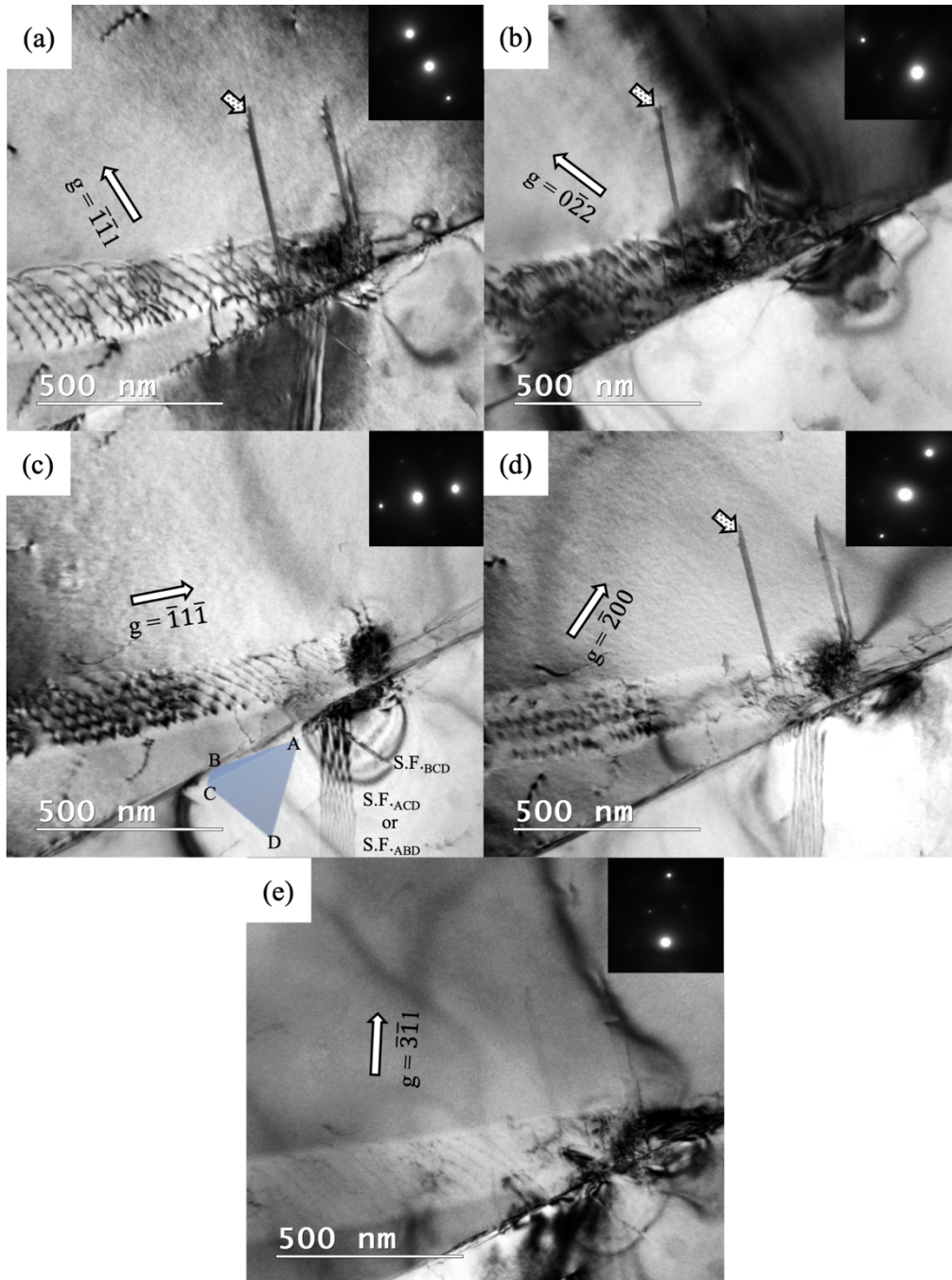


Figure 3.4 A series of $\mathbf{g} \cdot \mathbf{b}$ analyses performed to a grain in the coarse-grained sample deformed to engineering strain = 0.02. Images were taken under five different diffraction conditions around a $[011]_{\text{fcc}}$ zone axis. The dark linear contrasts from the partial dislocations on the tip of stacking fault are indicated by arrows filled with dots. The piled-up dislocations are designated to be perfect dislocations with the burgers vector of $\frac{a}{2} [0\bar{1}1]$ while the burgers vector of the emitted partial dislocations is $\frac{a}{6} [\bar{2}\bar{1}1]$. A Thompson tetrahedron added in (c) indicates two emitted stacking faults from the grain boundary to the adjacent grain. The inclined stacking fault is found to be on plane ACD or ABD, while the edge-on stacking fault is found to be on plane BCD. The operative reflections are (a) $\mathbf{g}_{\bar{1}\bar{1}1}$, (b) $\mathbf{g}_{0\bar{2}2}$, (c) $\mathbf{g}_{\bar{1}\bar{1}1}$, (d) $\mathbf{g}_{\bar{2}00}$ and (e) $\mathbf{g}_{\bar{3}\bar{1}1}$.

Table 3.2 The $\mathbf{g} \cdot \mathbf{b}$ for perfect dislocations on (111) and partials dislocation on ($\bar{1}\bar{1}\bar{1}$) associated with operative reflection of **Fig. 3.4**.

Operative reflections	Piled-up dislocations			Partial dislocations on S.F.		
	$[10\bar{1}]$	$[0\bar{1}1]$	$[\bar{1}10]$	$[121]$	$[\bar{2}\bar{1}1]$	$[1\bar{1}\bar{2}]$
$(\bar{1}\bar{1}1)$	± 1	± 1	0	$\pm \frac{1}{3}$	$\pm \frac{2}{3}$	$\pm \frac{1}{3}$
$(0\bar{2}2)$	± 1	± 2	± 1	$\pm \frac{1}{3}$	$\pm \frac{2}{3}$	$\pm \frac{1}{3}$
$(\bar{1}\bar{1}\bar{1})$	0	± 1	± 1	0	0	0
$(\bar{2}00)$	± 1	0	± 1	$\pm \frac{1}{3}$	$\pm \frac{2}{3}$	$\pm \frac{1}{3}$
$(\bar{3}\bar{1}1)$	± 2	± 1	± 1	$\pm \frac{2}{3}$	$\pm \frac{1}{3}$	$\pm \frac{2}{3}$

The analysis is to determine the Burgers vector of piled-up dislocations and leading Shockley partial dislocations formed from this annealing twin boundary. The $\mathbf{g} \cdot \mathbf{b}$ values of perfect dislocations on a (111) slip plane and emitted Shockley partial dislocations on a ($\bar{1}\bar{1}\bar{1}$) fault plane are summarized in **Table 3.2**. The piled-up dislocations were visible in the two-beam condition with $\mathbf{g}=\bar{1}\bar{1}1$ and $\mathbf{g}=\bar{1}\bar{1}\bar{1}$ whereas the same dislocations became invisible with $\mathbf{g} = \bar{2}00$. For the two-beam condition with $\mathbf{g}=\bar{3}\bar{1}1$ as shown in **Fig. 3.4(e)**, the piled-up dislocations were still visible but their image contrast became weak compared to the strong contrast with $\mathbf{g}=0\bar{2}2$. Based on the $\mathbf{g} \cdot \mathbf{b}$ values in **Table 3.2**, the piled-up dislocations can be designated to be $[0\bar{1}1]$ perfect dislocations. The Burgers vector analysis of Shockley partial dislocations bounding stacking fault was also conducted with the invisibility criterion proposed by Tunstall and Goodhew ⁴⁶. The contrast of partial dislocations is visible when $\mathbf{g} \cdot \mathbf{b}_p = \pm \frac{2}{3}$, but they turn to be invisible in $\mathbf{g} \cdot \mathbf{b}_p = \pm \frac{1}{3}$, where \mathbf{b}_p is the Burgers vector of the Shockley partial dislocations. Since the fault plane formed from boundary is ($\bar{1}\bar{1}\bar{1}$), the Shockley partial dislocations emitted from the grain boundary could be $\frac{a}{6}[\bar{2}\bar{1}1]$, $\frac{a}{6}[121]$ or $\frac{a}{6}[1\bar{1}\bar{2}]$. Changes in contrast of partial dislocations under different two-beam conditions can be seen through **Fig. 3.4(a-e)**. According to the $\mathbf{g} \cdot \mathbf{b}_p$ value listed in **Table 3.2**, the value of $\mathbf{g} \cdot \frac{a}{6}[\bar{2}\bar{1}1]$ is $\pm \frac{2}{3}$ for $\bar{1}\bar{1}1$, $0\bar{2}2$ and $\bar{2}00$ reflection while the

value of $\mathbf{g} \cdot \frac{a}{6} [\bar{2}\bar{1}1]$ is $\pm \frac{1}{3}$ for $\bar{3}\bar{1}1$ reflection. Based on the invisibility criterion of $\mathbf{g} \cdot \mathbf{b}_p$, the contrast of partial dislocations shown in **Fig. 3.4(e)** was invisible, while the dark-line contrast of partial dislocations on the tip of the stacking fault (arrows filled with dots) in **Fig. 3.4(a, b, d)** was visible. With at least three non-coplanar two-beam examinations for $\mathbf{g} \cdot \mathbf{b}_p$ values listed in **Table 3.2**, the nature of $\frac{a}{6} [\bar{2}\bar{1}1]$ partial dislocations can be confirmed. Besides, **Fig. 3.4(c)** indicates that more than one fault planes were revealed at the neighboring grain. Considering the inset projection of Thompson tetrahedron in **Fig. 3.4(c)**, a stacking fault lying on an inclined plane (plane ACD or plane ABD) and an edge-on fault lying on plane BCD were observed, i.e., more than one deformation twin nuclei were formed at an annealing twin boundary at the early stage of plastic deformation. According to the deformation twin nucleation mechanisms proposed^{39,40,47-49}, these stacking faults could be a precursor of deformation twin for the coarse-grained sample.

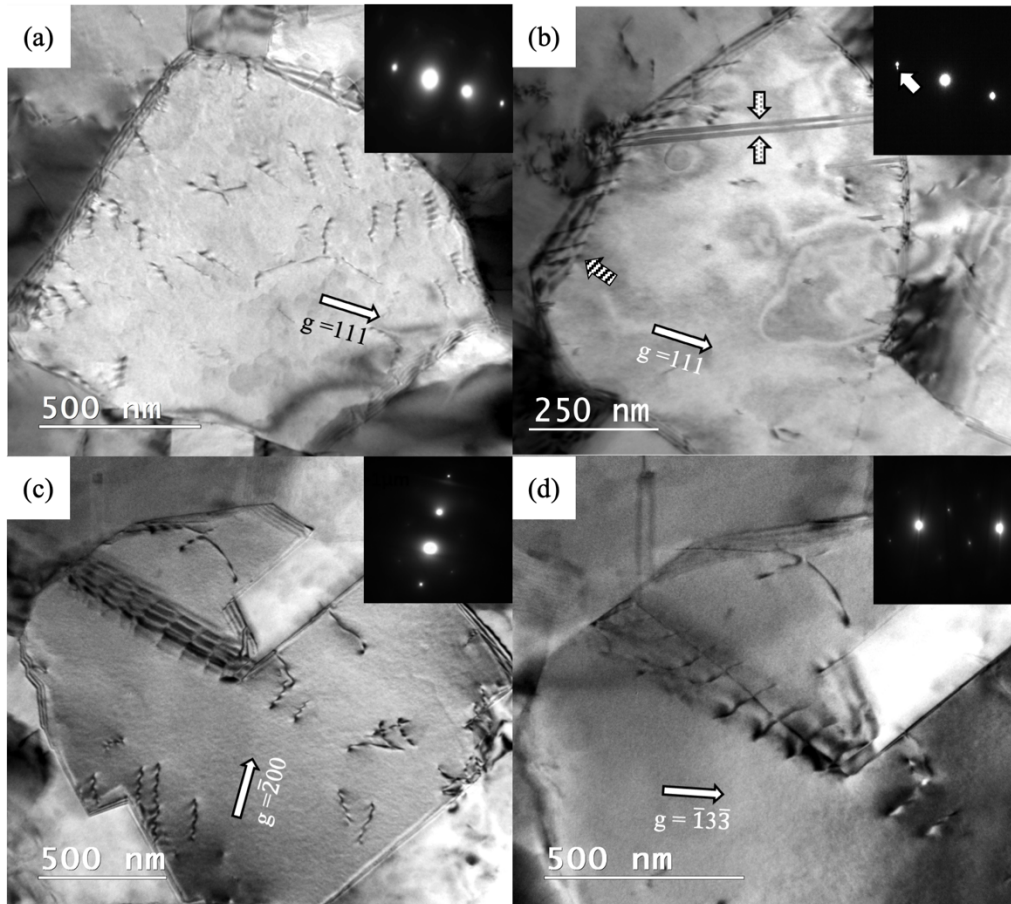


Figure 3.5 BF TEM images showing the microstructure and defects in the UFG sample deformed to engineering strain = 0.03. (a) Piled-up dislocations observed in an over-1 μ m grain. (b) Two stacking faults generated at a grain boundary (arrows filled with dots) and dislocations formed at a grain boundary (striped arrow) in an under-1 μ m grain (size nearly 700 nm). (c) Overlapping stacking faults near a grain boundary and few dislocations in the grain interior in an around-1 μ m grain (size nearly 1.2 μ m). (d) A magnified view of (c) indicating partial dislocations slipping on fault planes. The operative reflections are (a) g_{111} , (b) g_{111} , (c) g_{200} and (d) $g_{\bar{1}33}$.

3.3.2.2 UFG TWIP steel: deformed to 0.03 engineering strain

BF TEM images in **Fig. 3.5** show the deformed microstructures of an UFG sample tensile tested to 0.03 engineering strain. By taking advantage of its grain size distribution, dislocation behavior in over-1 μ m, around-1 μ m and under-1 μ m grains in the UFG sample were examined. First, piled-up dislocations being impinged on a grain boundary in an over-1 μ m grain (**Fig. 3.5(a)**) were similar to those observed in the coarse-grained counterpart (**Fig. 3.3(a, b)**), however, neither the stacking fault formation nor the dislocation cross slip

was observed. Second, stacking faults started nucleating from grain boundaries without having dislocation pile-ups were observed (arrows filled with dots) in an under-1 μm grain (**Fig. 3.5(b)**). Some extrinsic grain boundary dislocations (striped arrow) were also revealed in here. The grain size somehow changes the dislocation activities in submicron grains.

Figure 3.5(c) and (d) represent an around-1 μm grain showing a pair of overlapping stacking faults nearly normal to the incident electron beam direction. In this grain size, not only emitted partial dislocations bounding stacking faults but also few dislocations in the grain interior were observed. In order to confirm the grain size difference influences the dislocation activities and deformation twinning behavior, the ultrafine-grained steels deformed to 0.046 and 0.063 engineering strains were further examined.

3.3.2.3. Ultrafine-grained TWIP steel: deformed to 0.046 engineering strain

BF TEM images of grains having three different sizes in the UFG sample deformed to 0.046 engineering strain were shown in **Fig. 3.6**. In an over-1 μm grain (**Fig. 3.6(a)**), multiple slip systems were activated, but no deformation twin was identified neither in the grain interior nor the vicinity of grain boundaries. Dislocations appear to be generated from the interior of the grain as indicated by striped arrows, and these are believed to be generated by the regular multiplication (Frank-Read mechanism). In contrast, the deformation behavior of an around-1 μm grain shown in **Fig. 3.6(b)** is quite different. To identify the number of dislocations in the grain interior, this grain was examined from a $[011]_{\text{fcc}}$ zone axis. As a result, the number of dislocations in the grain interior was low, whereas nanometer size deformation twins formed at grain boundaries were found, as a representative one being circled in **Fig. 3.6(b)**. The inset image in **Fig. 3.6(b)** is a high-resolution TEM image taken from a $[011]_{\text{fcc}}$ zone axis, confirming the atomic structure of

the deformation twin.

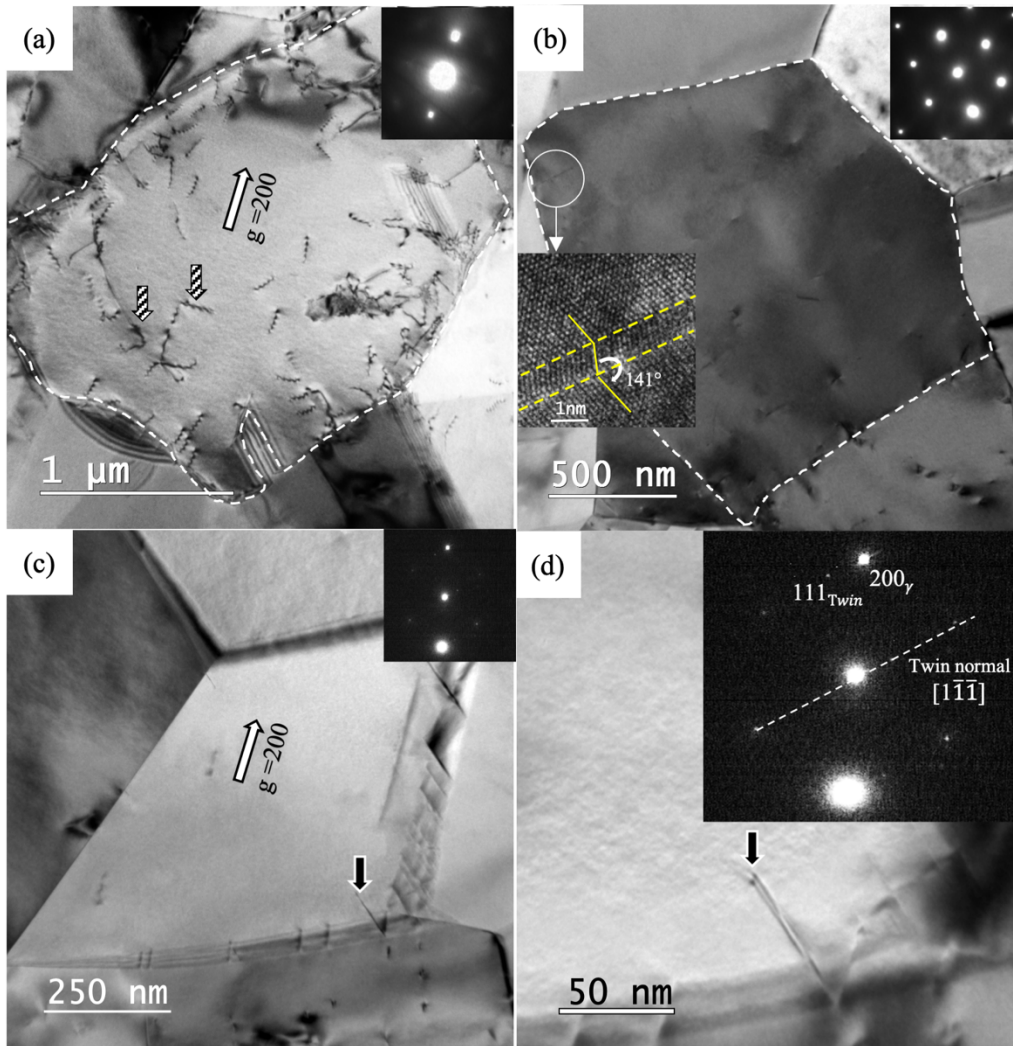


Figure 3.6 BF TEM images showing the microstructure and defects in the UFG sample deformed to engineering strain = 0.046. (a) Dislocations (striped arrows) appear to be generated from grain interior Frank-read sources in an over-1 μm grain (size nearly 2 μm). (b) A nearly 1 nm thick deformation twin in an around-1 μm grain (size nearly 1.4 μm). The inset HRTEM image shows the atomic structure of the thin deformation twin. (c) Grain boundaries decorated by several deformation twins in an under-1 μm grain (size smaller than 500 nm), (d) a magnified view of a deformation twin (black arrow) in (c), and a corresponding SAED pattern taken near a $[0\bar{1}\bar{1}]_{fcc}$ zone axis showing reflections from the deformation twin.

An under-1 μm grain (<500 nm) shown in **Fig. 3.6(c)** demonstrates planer defects nucleated from grain boundaries. The grains interior was likely free of dislocations, which infers that the dislocation sources at grain interior in this grain size range were lacked or no

longer predominant even though the size of grain has not been approached to the proposed threshold grain size that makes the in-grain dislocation glides impossible (100 nm for high-SFE alloys). A magnified view of a planar defect on a grain boundary indicated by black arrow is shown in **Fig. 3.6(d)** together with several others having a similar contrast. The one indicated by black arrow is identified as a deformation twin by analyzing SAED pattern taken near a $[0\bar{1}1]_{fcc}$ zone axis, shown as the inset of **Fig. 3.6(d)**. The indexed $(111)_{Twin}$ extra spot arising from the planar defect confirmed the occurrence of deformation twinning at grain boundaries, where the twin axis $[1\bar{1}\bar{1}]$ is also indicated for a visual aid.

3.3.2.4 Ultrafine-grained TWIP steel: deformed to 0.062 engineering strain

The detailed dislocations and deformation twins distributions were shown in **Fig. 3.7**. In an around-1 μm size grain (**Fig. 3.7(a)**), wavy and tangled dislocations were clearly visible in a two-beam BF TEM image with the operative g-vector $\mathbf{g} = 111$. The interplay between various dislocations resided in conjugate $\{111\}$ slip planes might be potential nucleation sites for new deformation twins by several possible mechanisms associated with dislocation evolution such as the pole mechanism, the stair-rod cross-slip mechanism, etc.^{36,50}. However, due to the insufficient number of dislocations in the grain interior, further dislocation reaction to form deformation twin nuclei was not likely to be plausible. More than one deformation twins were generated from grain boundaries of another around-1 μm grain, as shown in an inset SAED in **Fig. 3.7(b)**. Two twins (black arrows) could be induced by the impingement of a deformation twin on an annealing twin boundary (white circle). They appear to travel across the annealing twin lamellae. **Fig. 3.7(c)** and **(d)** show the formation of overlapping stacking faults, which should be related to the continuous emission of partial dislocations lying on successive $\{111\}$ planes. The variation of stacking

fault's fringe contrast observed in **Fig. 3.7(c)** and **Fig. 3.7(d)** (arrow filled with dots) provide supportive evidences of overlapping stacking faults being a precursor of deformation twins, which has been mentioned in several earlier studies^{33,39,40}.

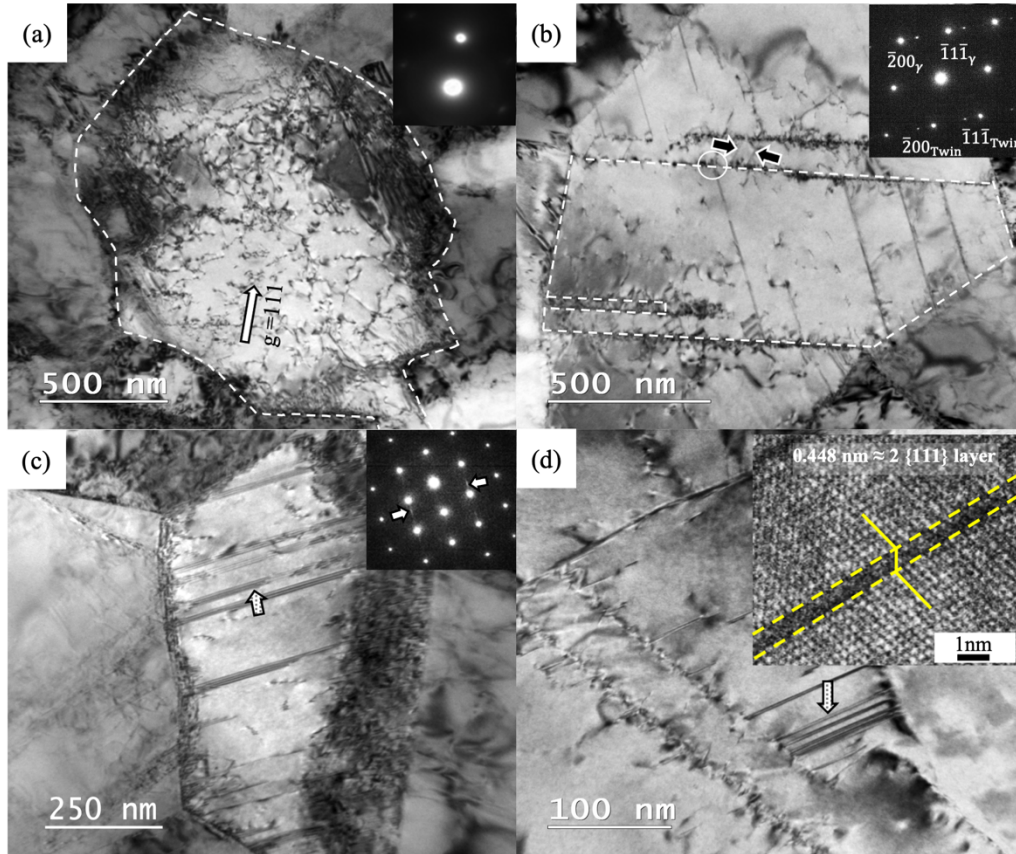


Figure 3.7 The microstructures and defects in the UFG sample deformed to engineering strain = 0.062. (a) Two beam BF TEM image shows wavy and tangled dislocations on multiple slip planes in an around-1 μm grain. The operative reflection is g_{111} . (b) BF TEM image shows various deformation twins in another around-1 μm grain. The inset $[011]_{\text{fcc}}$ zone axis SAED pattern is taken from a fine twin. Deformation twins induced by the impingement (white circle) occurred between deformation twin and annealing twin were observed. (c) BF TEM image shows high density of overlapping stacking faults (arrow filled with dots) in an under-1 μm grain (size nearly 500 nm). Streak contrast (white arrows) in the corresponding SAED pattern taken from a $[01\bar{1}]_{\text{fcc}}$ zone axis is due to the shape factor of the overlapping stacking faults. (d) BF TEM image shows multiple stacking faults (arrow filled with dots) in an under-1 μm grain (size nearly 300 nm). The inset HRTEM image shows a two-layer thick stacking fault (thickness is 0.448 nm, i.e., $2 \times \{111\}$ planes).

3.4 Discussion

The main finding of this research concerning the influence of grain size on plastic deformation mechanisms associated with yielding, i.e., at the early stage of plastic

deformation, is that the stacking fault and deformation twin nucleation is not significantly inhibited even in the submicron grain size range at room temperature. As compared with experimental results by Bai et al. [16] and Kitamura [17], TEM observations in this study are consistent to their SEM-ECCI observations and *in-situ* synchrotron radiation X-ray diffraction measurements, suggesting that the lack of initial mobile dislocations in individual grains and inactive grain interior dislocation source in ultrafine grains appear to be responsible to the high upper yield strength. At or after yielding, to initiate or develop a further plastic deformation in the UFG sample, carriers of plastic deformation or a new deformation mode have to be nucleated or initiated, i.e., the nucleation of stacking faults and deformation twin at grain boundary. As a result, the flow stress might drop at that moment to release the elastic energy stored in the steel ³². In this study, the formation of planar defects such as stacking faults and deformation twins were observed in both coarse-grained and UFG samples, whereas the dislocation substructure in those samples were quite different.

3.4.1 Stacking fault nucleation in the coarse-grained TWIP steel

Considering the case in **Fig. 3.3(b)** in which dislocations traveled toward the annealing twin boundary, the incoming dislocations would be blocked by the grain boundary and inevitably resulted in the dislocation pile-ups unless the incoming dislocations have a specific Burgers vector that would allow the incoming dislocations cross-slip to the adjacent grain. This is schematically illustrated in **Fig. 3.8**, where the specific Burgers vector corresponds to \overline{CD} in the Thompson tetrahedron. As the plastic deformation proceeded, localized stress concentration fields will gradually build up in/near the grain boundary regions. This would stimulate subsequent reaction that the incoming dislocations to

dissociate into partial dislocations on the conjugate slip planes of the original grain due to its low SFE characteristic. According to the image series analysis in **Fig. 3.4**, the Burgers vector of piled-up dislocations, \mathbf{b} and the emitted Shockley partial dislocations, \mathbf{b}_p are designated to be $\frac{a}{2} [0\bar{1}1]_{111}$ and $\frac{a}{6} [\bar{2}\bar{1}1]_{\bar{1}\bar{1}\bar{1}}$, respectively. As the process of incoming dislocations interacting with the annealing twin boundary gradually builds up a large stress field in/near the boundary regions, the entry of additional incoming dislocations lying on plane ACD would be obstructed and the perfect dislocations may start to dissociate into two Shockley partial dislocations, $\frac{a}{2} [0\bar{1}1]_{111} = \frac{a}{6} [\bar{1}\bar{1}2]_{111} + \frac{a}{6} [1\bar{2}1]_{111}$ due to the local stress concentration and alloy's relatively low-SFE characteristic. Based on the Fujita-Mori deformation twinning model ³⁶, the cross-slip of Shockley partial dislocations enables one of Shockley partials on the primary slip plane to dissociate into a stair-rod sessile

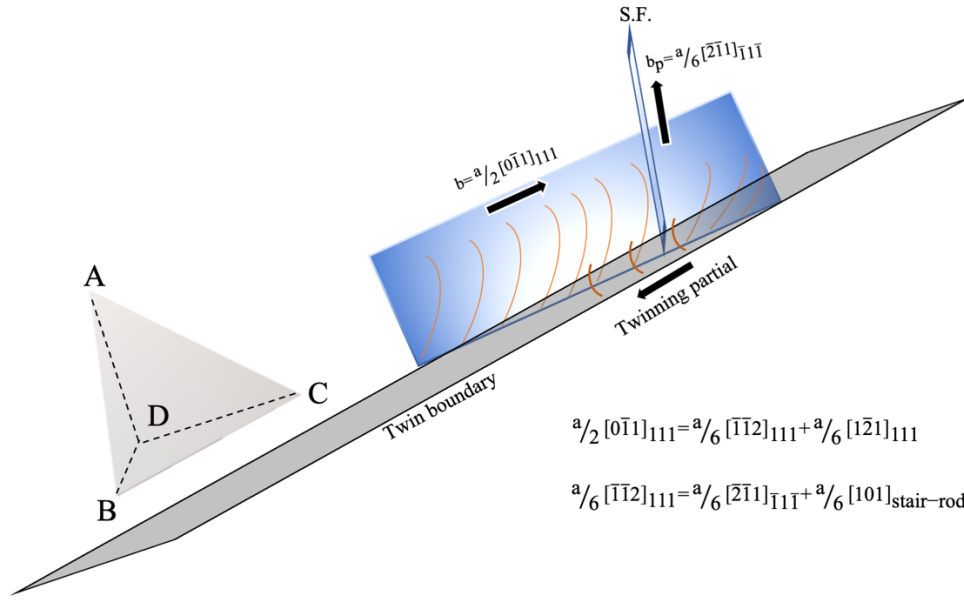


Figure 3.8 A schematic illustration shows the precursor of deformation twin initiated at the area near grain boundary as a result of piled-up dislocations and an annealing twin boundary interaction. The Burgers vectors \mathbf{b} and \mathbf{b}_p were designated to be $\frac{a}{2} [0\bar{1}1]_{111}$ and $\frac{a}{6} [\bar{2}\bar{1}1]_{\bar{1}\bar{1}\bar{1}}$, respectively. The Fujita-Mori twinning model associated with cross-slip of partial dislocations appears to be the main twinning mechanism in this coarse-grained TWIP sample.

dislocation and a glissile $\frac{a}{6}\langle 112 \rangle$ -type partial dislocation on conjugate slip planes (the ABD plane in **Fig. 3.8**), which can reasonably reduce the repulsive force and also explain the present deformation twin nuclei formation in coarse-grained size range (over 10 μm).

The possible reaction shows here:

$$\frac{a}{6} [\bar{1}\bar{1}2]_{111} = \frac{a}{6} [\bar{2}\bar{1}1]_{\bar{1}\bar{1}\bar{1}} + \frac{a}{6} [101]_{\text{stair-rod}} \quad (4)$$

Shockley partial dislocations with Burgers vector $\frac{a}{6} [\bar{2}\bar{1}1]_{\bar{1}\bar{1}\bar{1}}$ then can glide away from an annealing twin boundary and will cross slip into a conjugate slip plane trailing a wide stacking fault as shown in **Fig. 3.8**. This result is similar to several past studies^{31,51,52} indicating that localized stress induced by piled-up dislocations could possibly trigger the formation of deformation twin.

The role of dislocation pile-ups at a grain boundary to cause macroscopic continuous yielding was addressed by C.W. Sinclair et al.⁵³. When the number of the incoming dislocations reaches the critical value at a grain boundary, the effective dislocation storage efficiency at the boundary becomes zero so that the contribution of backstress to the total flow stress becomes negligible. In the present study, the stacking fault nucleation governed by the cross-slip of partial dislocations and the slip transfer across the boundary cause a continuous yielding behavior. However, this dislocation-based model would be insufficient to explain the discontinuous yielding in the UFG sample due to the lack of initial mobile dislocations.

3.4.2 Stacking fault and deformation twin nucleation in ultrafine grained TWIP steel

In **Figs. 3.5-7**, it was found that the initial plastic deformation behavior varied as a function of the grain size. Dislocation gliding and tangling were observed in the grain interior of over-1 μm grains, whereas stacking faults and deformation twins were nucleated at grain boundaries without the presence of dislocation pile-ups in under-1 μm grains. According to the microstructure observation of the deformed coarse-grained samples, deformation twins could subsequently nucleate from either the grain interior or near/at grain boundary regions as long as a local stress concentration caused by dislocation dynamics exists. However, this mechanism required sufficient numbers of piled-up dislocations, which were not observed in the under-1 μm grains.

The number of dislocations generated from the grain interior to reach a grain boundary highly depends on their multiplication. Dislocations in a conventional coarse grain are believed to be multiplied by Frank-Read sources. The operation of Frank-Read source activated by a critical shear stress is defined by a relationship as followed⁵⁴:

$$\tau_{F-R} = \frac{3G|\mathbf{b}|}{d} \quad (5)$$

where G denotes the shear modulus, $|\mathbf{b}|$ the magnitude of Burgers vector and d the grain size. The stress needed to activate a Frank-Read dislocation source is in inverse proportion to the size of grains. For the UFG sample with the average grain size of $0.79 \mu\text{m}$ examined in this study, the stress ($\tau_{F-R} = 40 \text{ MPa}$) required to activate Frank-Read dislocation sources is not high but still achievable. The shear stress could lead some dislocations to be bred from the interior of a grain. However, the continuous generation of dislocations from the grain interior would be inhibited due to the small grain size. A critical resolved shear stress (CRSS) model considering the information on grain boundaries as dislocation sources was described by Aoyagi et al. ^{55,56}. In their deformation model, the flow stress is described as the following equation:

$$g^{(\alpha)} = \tau_d^{(\alpha)} + \min \{ \tau_s^{(\alpha)}, \tau_m^{(\alpha)}, \tau_g^{(\alpha)} \} \quad (6)$$

Here, $g^{(\alpha)}$ is the flow stress on slip system α , $\tau_d^{(\alpha)}$ is the deformation resistance originating in accumulated dislocations, $\tau_s^{(\alpha)}$ is that originating in the grain interior dislocation sources, $\tau_m^{(\alpha)}$ is that originating in mobile dislocations, and $\tau_g^{(\alpha)}$ is that originating in grain boundaries. In their calculation, the required minimum shear stress to activate the dislocation sources at grain boundaries ($\tau_g^{(\alpha)}$) is higher than that to activate grain interior Frank-Read dislocation sources ($\tau_s^{(\alpha)}$), and independent from the misorientation angle of each grain boundary. As a result, dislocations are initially expected to be generated from the grain interior. When the dislocation density in the grain interiors reaches the saturation, the flow stress controlled by the term, $\tau_g^{(\alpha)}$, of the equation (6) will be the primary contribution to the total flow stress and it should be high enough to generate dislocations from grain boundaries. For the over-

1 μm grains, the flow stress controlled by $\tau_d^{(\alpha)}$, $\tau_s^{(\alpha)}$, and $\tau_m^{(\alpha)}$ can easily be achieved to the level to activate the grain interior dislocation sources because the number of the grain interior dislocation sources are sufficient. In this case, the value of $\tau_g^{(\alpha)}$ does not contribute the stress value; differently, dislocation accumulation and propagation at a grain boundary would happened in many similar grain boundaries, which is similar to experimental works done by Hirth et al. ⁵⁷ and MD simulation calculated by Tsuru et al. ⁵⁸. In the under-1 μm grains, the dislocation mean free path is relatively short. As a result, after relatively small numbers of dislocations were formed from the grain interior, the dislocation density and resultant internal stress in the under-1 μm grains could be high enough to deactivate the grain interior (Frank-Read) dislocation sources. Then, the transition of dislocation sources from the grain interior to the grain boundaries would occur when the applied stress related to $\tau_g^{(\alpha)}$ in equation (6) becomes large enough to activate the grain boundary sources.

The detailed deformed microstructures in the over-1 μm , around-1 μm , and under-1 μm grains were examined at several strain levels around the macroscopic yield point in the

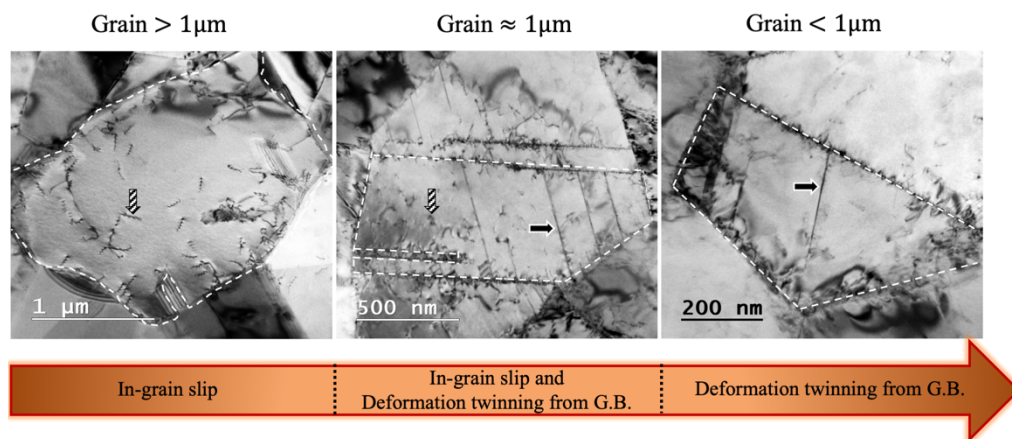


Figure 3.9 The representative initial deformed microstructure in the UFG sample shows a clear correlation between the plastic deformation mechanisms and grain size: (a) grain size > 1 μm ; slip dominant, (b) grain size \sim 1 μm : slip and twinning mixture, and (c) grain size \leq 1 μm : twinning dominant.

present study. The deformation twinning behavior could be divided into three categories based on the grain size, as summarized in **Fig. 3.9**. The dominant plastic deformation mechanism of the UFG TWIP steel around the macroscopic yield point is (a) by slip in over-1 μm grains, (b) by a mixture of slip and deformation twinning in around-1 μm grains, (c) by twinning in under-1 μm grains. It appears that dislocation sources were changed from the grain interior to grain boundaries when the gain size comes to near 1 μm , causing the emission of partial dislocations, i.e., change of deformation mode from in-grain slip to stacking faults and deformation twin nucleation at grain boundaries would releases the elastic energy stored in the sample and results in a macroscopic yield drop in the engineering stress-strain curve.

Zhu et al.⁵⁹ proposed a possible partial multiplication mechanism at a “non-equilibrium” grain boundary in nanocrystalline systems. Such grain boundary will supply leading partial dislocations on every successive $\{111\}$ slip planes for deformation twin nucleation and growth. In their model, a grain boundary dislocation having Burgers vector of $\mathbf{b}_{\text{G.B.}}$ can dissociate into two Shockley partial dislocations having Burgers vector of \mathbf{b}_1 and \mathbf{b}_2 under a proper applied stress,

$$\mathbf{b}_{\text{G.B.}} = \mathbf{b}_1 + \mathbf{b}_2 \quad (7)$$

$\mathbf{b}_{\text{G.B.}}$ represents the Burgers vector of a grain boundary dislocation. \mathbf{b}_1 and \mathbf{b}_2 represent the Burgers vector of two dissociated Shockley partial dislocations at a grain boundary. Under an applied stress in an appropriate orientation, \mathbf{b}_2 can glide into a $\{111\}$ slip plane away from the grain boundary forming a wide stacking fault. The \mathbf{b}_1 having pure screw characteristic can be cross-slip into a next parallel $\{111\}$ plane, where it undergoes as the followed dislocation reaction:

$$\mathbf{b}_1 = \mathbf{b} + (-\mathbf{b}_2) \quad (8)$$

$-\mathbf{b}_2$ stays at a grain boundary, but \mathbf{b} subsequently dissociates into \mathbf{b}_1 and \mathbf{b}_2 as followed by Equation (8). \mathbf{b}_2 having higher resolved shear stress will be stimulated to slip. The slip of \mathbf{b}_2 promotes twin formation, and \mathbf{b}_1 returns back and stays at the grain boundary due to the insufficient resolved shear stress to drive it over the grain. According to Zhu's model, an appropriate crystal grain orientation and localized applied stress seem critical to promote Shockley partial dislocations to glide away but trailing screw dislocations to stay at the grain boundary.

The shift of plastic deformation mechanisms, or carriers of plastic deformation, suggests that the types and density of plastic deformation carriers, and their behaviors are also under a strong influence of grain size. For example, the difference in the grain interior dislocation density and how their multiplication occurs are both critical to determine the yielding behavior. It is generally accepted that grain size around $1\mu\text{m}$ is likely the tipping point for the plastic deformation behavior of UFG materials, and some previous studies indicated the inhibition of deformation twin nucleation in an UFG TWIP steel around this grain size. The current study did not observe such inhibition, however some other materials parameters such as SFE and/or grain boundary character are likely involved in the twin nucleation process. The change of dislocation sources from the grain interior Frank-Read sources to grain boundaries with decreasing the grain size discussed in here in principle agrees with scale-dependent yield stress changes proposed by Ohashi et al. ⁶⁰.

3.5 Conclusions

The underlying mechanism of discontinuous yielding behavior in an UFG Fe-31Mn-3Al-3Si austenitic TWIP steel was investigated with taking particular attention to the

deformed microstructures around yielding in the UFG sample. In Comparison with the conventional coarse-grained counterpart, plastic deformation mechanisms in the early stage of deformation, around the macroscopic yield point, shows an obvious grain size dependence.

1. In the coarse-grained sample, piled-up dislocations being impinged on an annealing twin boundary induces stacking faults nucleation at the twin boundary, while the screw dislocations generating slip transfer across a twin boundary appears not effective to the stacking fault nucleation. The formation of stacking faults associated with dislocation cross-slip is confirmed by a series of $\mathbf{g} \cdot \mathbf{b}$ analyses. The stacking faults could be a precursor of deformation twin.
2. In the UFG sample, the initial plastic deformation behavior in each of different-size grains is unique. Dislocations appear to be generated from the in-grain sources in the over-1 μm grains, whereas stacking faults/deformation twins were directly nucleated at grain boundaries in the under-1 μm grains. The deformation twin formation is not inhibited in submicron grains. Grain size around 1 μm is likely the tipping point to alter the main dislocation sources from the in-grain Frank-Read sources to grain boundaries (e.g. **Fig. 3.6(a-b)**), which grain boundary dislocations were observed in the early stage of plastic deformation (to 0.03 engineering strain) then appears to lead the subsequent deformation twin nucleation.
3. In the UFG sample, the lack of initial mobile dislocations in each grain and inactive grain interior dislocation source in ultrafine grains appear to be responsible to the high upper yield strength. After yield point, the elastic energy stored in the steel would be released by the initiation of new deformation modes, i.e., the nucleation of stacking faults and deformation twin at grain boundary. The shift of deformation mechanism from in-grain slip to

deformation twinning at grain boundary results in the macroscopic yield drop in the engineering stress-strain curve.

4. Zhu's model ⁵⁹ is likely applicable to the deformation twinning mechanism for the grains $\leq 1\mu\text{m}$ in the ultrafine-grained steels. The current study did not observe the inhibition of deformation twin nucleation in this size range, suggesting that some other materials parameters such as SFE and/or grain boundary character ought to be involved in the twin nucleation process.

Acknowledgements

The authors would like to thank W. T. Reynolds at Virginia Tech for useful discussions. This study was partly supported by Nanoscale Characterization and Fabrication Laboratory (NCFL), Institute for Critical Technology and Applied Science (ICTAS), Virginia Tech and used shared facilities at the Virginia Tech National Center for Earth and Environmental Nanotechnology Infrastructure (NanoEarth), a member of the National Nanotechnology Coordinated Infrastructure (NNCI), supported by NSF (ECCS 1542100, 2025151). N.T. and M.M. greatly appreciate the financial support by the JST CREST (JPMJCR1994). M.M. acknowledges a financial support by JSPS KAKENHI Grant Numbers (19H02029, 20H02479). N.T. acknowledges a financial support by Elements Strategy Initiative for Structural Materials (ESISM, No. JPMXP0112101000), the Grant-in-Aid for Scientific Research (S) (No. 15H05767), and the Grant-in-Aid for Scientific Research (A) (No. 20H00306), all through the Ministry of Education, Culture, Sports, Science and Technology (MEXT), Japan.

References

1. De Cooman, B. C., Estrin, Y. & Kim, S. K. Twinning-induced plasticity (TWIP) steels. *Acta Mater.* **142**, 283–362 (2018).
2. Vercammen, S., Blanpain, B., De Cooman, B. C. C. & Wollants, P. Cold rolling behaviour of an austenitic Fe-30Mn-3Al-3Si TWIP-steel: The importance of deformation twinning. *Acta Mater.* **52**, 2005–2012 (2004).
3. Bouaziz, O., Allain, S., Scott, C. P., Cugy, P. & Barbier, D. High manganese austenitic twinning induced plasticity steels: A review of the microstructure properties relationships. *Curr. Opin. Solid State Mater. Sci.* **15**, 141–168 (2011).
4. Allain, S., Chateau, J.-P. & Bouaziz, O. A physical model of the twinning-induced plasticity effect in a high manganese austenitic steel. *Mater. Sci. Eng. A* **387–389**, 143–147 (2004).
5. Rémy, L. The interaction between slip and twinning systems and the influence of twinning on the mechanical behavior of fcc metals and alloys. *Metall. Trans. A* **12**, 387–408 (1981).
6. Remy, L. & Pineau, A. Twinning and strain-induced F.C.C. → H.C.P. transformation in the FeMnCrC system. *Mater. Sci. Eng.* **28**, 99–107 (1977).
7. Lee, T.-H., Shin, E., Oh, C.-S., Ha, H.-Y. & Kim, S.-J. Correlation between stacking fault energy and deformation microstructure in high-interstitial-alloyed austenitic steels. *Acta Mater.* **58**, 3173–3186 (2010).
8. Pierce, D. T. *et al.* The influence of manganese content on the stacking fault and austenite/ ϵ -martensite interfacial energies in Fe–Mn–(Al–Si) steels investigated by experiment and theory. *Acta Mater.* **68**, 238–253 (2014).

9. Pierce, D. T., Jiménez, J. A., Bentley, J., Raabe, D. & Wittig, J. E. The influence of stacking fault energy on the microstructural and strain-hardening evolution of Fe–Mn–Al–Si steels during tensile deformation. *Acta Mater.* **100**, 178–190 (2015).
10. Curtze, S. & Kuokkala, V. T. Dependence of tensile deformation behavior of TWIP steels on stacking fault energy, temperature and strain rate. *Acta Mater.* **58**, 5129–5141 (2010).
11. Kang, S., Jung, J., Kang, M., Woo, W. & Lee, Y. K. The effects of grain size on yielding, strain hardening, and mechanical twinning in Fe-18Mn-0.6C-1.5Al twinning-induced plasticity steel. *Mater. Sci. Eng. A* **652**, 212–220 (2016).
12. Byun, T. S., Hashimoto, N. & Farrell, K. Temperature dependence of strain hardening and plastic instability behaviors in austenitic stainless steels. *Acta Mater.* **52**, 3889–3899 (2004).
13. Kang, S., Lee, Y.-K., Jin, J.-E., Jung, Y.-S. & Jeong, K. The effects of Si on the mechanical twinning and strain hardening of Fe–18Mn–0.6C twinning-induced plasticity steel. *Acta Mater.* **61**, 3399–3410 (2013).
14. Gutierrez-Urrutia, I. & Raabe, D. Dislocation and twin substructure evolution during strain hardening of an Fe–22 wt.% Mn–0.6 wt.% C TWIP steel observed by electron channeling contrast imaging. *Acta Mater.* **59**, 6449–6462 (2011).
15. Tian, Y. Z. *et al.* Significant contribution of stacking faults to the strain hardening behavior of Cu-15%Al alloy with different grain sizes. *Sci. Rep.* **5**, 2–10 (2015).
16. Bai, Y. *et al.* Unique Yielding Behavior in Ultrafine Grained High-Mn. Submitted (2020).
17. H. Kitamura. Master thesis. (Kyoto University, 2017).

18. Ueji, R. *et al.* Tensile properties and twinning behavior of high manganese austenitic steel with fine-grained structure. *Scr. Mater.* **59**, 963–966 (2008).
19. Dini, G., Najafizadeh, A., Ueji, R. & Monir-Vaghefi, S. M. Improved tensile properties of partially recrystallized submicron grained TWIP steel. *Mater. Lett.* **64**, 15–18 (2010).
20. Bai, Y., Momotani, Y., Chen, M. C., Shibata, A. & Tsuji, N. Effect of grain refinement on hydrogen embrittlement behaviors of high-Mn TWIP steel. *Mater. Sci. Eng. A* **651**, 935–944 (2016).
21. Kang, S., Jung, J.-G., Kang, M., Woo, W. & Lee, Y.-K. The effects of grain size on yielding, strain hardening, and mechanical twinning in Fe–18Mn–0.6C–1.5Al twinning-induced plasticity steel. *Mater. Sci. Eng. A* **652**, 212–220 (2016).
22. Tian, Y. Z. *et al.* A novel ultrafine-grained Fe–22Mn–0.6C TWIP steel with superior strength and ductility. *Mater. Charact.* **126**, 74–80 (2017).
23. Gutierrez-Urrutia, I. & Raabe, D. Grain size effect on strain hardening in twinning-induced plasticity steels. *Scr. Mater.* **66**, 992–996 (2012).
24. Saha, R., Ueji, R. & Tsuji, N. Fully recrystallized nanostructure fabricated without severe plastic deformation in high-Mn austenitic steel. *Scr. Mater.* **68**, 813–816 (2013).
25. Tian, Y. Z. *et al.* Enhanced Strength and Ductility in an Ultrafine-Grained Fe-22Mn-0.6C Austenitic Steel Having Fully Recrystallized Structure. *Metall. Mater. Trans. A Phys. Metall. Mater. Sci.* **45**, 5300–5304 (2014).
26. Tian, Y. Z. *et al.* Two-stage Hall-Petch relationship in Cu with recrystallized structure. *J. Mater. Sci. Technol.* **48**, 31–35 (2020).

27. Tian, Y. Z. *et al.* Remarkable transitions of yield behavior and Lüders deformation in pure Cu by changing grain sizes. *Scr. Mater.* **142**, 88–91 (2018).
28. Yu, C. Y., Kao, P. W. & Chang, C. P. Transition of tensile deformation behaviors in ultrafine-grained aluminum. *Acta Mater.* **53**, 4019–4028 (2005).
29. El-Danaf, E., Kalidindi, S. R. & Doherty, R. D. Influence of grain size and stacking-fault energy on deformation twinning in fcc metals. *Metall. Mater. Trans. A Phys. Metall. Mater. Sci.* **30**, 1223–1233 (1999).
30. Meyers, M. A., Vohringer, O. & Lubarda, V. A. the Onset of Twinning in Metals. *Acta Mater.* **49**, 4025–4039 (2001).
31. Gutierrez-Urrutia, I., Zaefferer, S. & Raabe, D. The effect of grain size and grain orientation on deformation twinning in a Fe–22wt.% Mn–0.6wt.% C TWIP steel. *Mater. Sci. Eng. A* **527**, 3552–3560 (2010).
32. Tsuji, N. *et al.* Strategy for managing both high strength and large ductility in structural materials—sequential nucleation of different deformation modes based on a concept of plaston. *Scr. Mater.* **181**, 35–42 (2020).
33. Idrissi, H., Renard, K., Ryelandt, L., Schryvers, D. & Jacques, P. J. On the mechanism of twin formation in Fe–Mn–C TWIP steels. *Acta Mater.* **58**, 2464–2476 (2010).
34. Cohen, J. B. & Weertman, J. A dislocation model for twinning in f.c.c. metals. *Acta Metall.* **11**, 996–998 (1963).
35. Liu, J. B., Liu, X. H., Liu, W., Zeng, Y. W. & Shu, K. Y. Transmission electron microscopy observation of a deformation twin in TWIP steel by an ex situ tensile test. *Philos. Mag.* **91**, 4033–4044 (2011).

36. Fujita, H. & Mori, T. A formation mechanism of mechanical twins in F.C.C. Metals. *Scr. Metall.* **9**, 631–636 (1975).
37. Bracke, L., Kestens, L. & Penning, J. Direct observation of the twinning mechanism in an austenitic Fe-Mn-C steel. *Scr. Mater.* **61**, 220–222 (2009).
38. Mahajan, S. & Chin, G. Y. Formation of deformation twins in f.c.c. crystals. *Acta Metall.* **21**, 1353–1363 (1973).
39. Mahato, B. *et al.* Simultaneous twinning nucleation mechanisms in an Fe–Mn–Si–Al twinning induced plasticity steel. *Acta Mater.* **132**, 264–275 (2017).
40. Mahato, B. *et al.* An effective stacking fault energy viewpoint on the formation of extended defects and their contribution to strain hardening in a Fe-Mn-Si-Al twinning-induced plasticity steel. *Acta Mater.* **86**, 69–79 (2015).
41. Idrissi, H., Renard, K., Schryvers, D. & Jacques, P. J. TEM investigation of the formation mechanism of deformation twins in Fe–Mn–Si–Al TWIP steels. *Philos. Mag.* **93**, 4378–4391 (2013).
42. Azizi-Alizamini, H., Militzer, M. & Poole, W. J. A novel technique for developing bimodal grain size distributions in low carbon steels. *Scr. Mater.* **57**, 1065–1068 (2007).
43. Wang, T. S., Zhang, F. C., Zhang, M. & Lv, B. A novel process to obtain ultrafine-grained low carbon steel with bimodal grain size distribution for potentially improving ductility. *Mater. Sci. Eng. A* **485**, 456–460 (2008).
44. Fan, G. J., Choo, H., Liaw, P. K. & Lavernia, E. J. Plastic deformation and fracture of ultrafine-grained Al–Mg alloys with a bimodal grain size distribution. *Acta Mater.* **54**, 1759–1766 (2006).

45. Lee, T. C., Robertson, I. M. & Birnbaum, H. K. TEM in situ deformation study of the interaction of lattice dislocations with grain boundaries in metals. *Philos. Mag. A* **62**, 131–153 (1990).
46. Tunstall, W. J. & Goodhew, P. J. Electron microscope image contrast of double loops in quenched aluminium. *Philos. Mag.* **13**, 1259–1272 (1966).
47. Casillas, G., Gazder, A. A., Pereloma, E. V. & Saleh, A. A. Evidencing extrinsic stacking faults in twinning-induced plasticity steel. *Mater. Charact.* **123**, 275–281 (2017).
48. Kim, J. K., Kwon, M. H. & De Cooman, B. C. On the deformation twinning mechanisms in twinning-induced plasticity steel. *Acta Mater.* **141**, 444–455 (2017).
49. Jacques, P. J., Schryvers, D., Idrissi, H., Renard, K. & Ryelandt, L. On the mechanism of twin formation in Fe–Mn–C TWIP steels. *Acta Mater.* **58**, 2464–2476 (2010).
50. Venables, J. A. On dislocation pole models for twinning. *Philos. Mag.* **30**, 1165–1169 (1974).
51. Dini, G., Najafizadeh, A., Ueji, R. & Monir-Vaghefi, S. M. Tensile deformation behavior of high manganese austenitic steel: The role of grain size. *Mater. Des.* **31**, 3395–3402 (2010).
52. Shterner, V., Timokhina, I. B., Rollett, A. D. & Beladi, H. The Role of Grain Orientation and Grain Boundary Characteristics in the Mechanical Twinning Formation in a High Manganese Twinning-Induced Plasticity Steel. *Metall. Mater. Trans. A* **49**, 2597–2611 (2018).
53. Sinclair, C. W., Poole, W. J. & Bréchet, Y. A model for the grain size dependent work

- hardening of copper. *Scr. Mater.* **55**, 739–742 (2006).
54. Han, W. Z., Zhang, Z. F., Wu, S. D. & Li, S. X. Combined effects of crystallographic orientation, stacking fault energy and grain size on deformation twinning in fcc crystals. *Philos. Mag.* **88**, 3011–3029 (2008).
 55. Aoyagi, Y., Tsuru, T. & Shimokawa, T. Crystal plasticity modeling and simulation considering the behavior of the dislocation source of ultrafine-grained metal. *Int. J. Plast.* **55**, 43–57 (2014).
 56. Aoyagi, Y., Shimokawa, T., Shizawa, K. & Kaji, Y. Simulation on Nanostructured Metals Based on Multiscale Crystal Plasticity Considering Effect of Grain Boundary. *Mater. Sci. Forum* **706–709**, 1751–1756 (2012).
 57. Hirth, J. P. The influence of grain boundaries on mechanical properties. *Metall. Trans.* **3**, 3047–3067 (1972).
 58. Tsuru, T., Aoyagi, Y., Kaji, Y. & Shimokawa, T. Influence of Competition between Intragranular Dislocation Nucleation and Intergranular Slip Transfer on Mechanical Properties of Ultrafine-Grained Metals. *Mater. Trans.* **54**, 1580–1586 (2013).
 59. Zhu, Y. T., Liao, X. Z. & Wu, X. L. Deformation twinning in nanocrystalline materials. *Prog. Mater. Sci.* **57**, 1–62 (2012).
 60. Ohashi, T., Kawamukai, M. & Zbib, H. A multiscale approach for modeling scale-dependent yield stress in polycrystalline metals. *Int. J. Plast.* **23**, 897–914 (2007).

Chapter 4

A Correlation Between Grain Boundary Character and Deformation Twin Nucleation Mechanism in Coarse-grained High-Mn Austenitic Steel

Chang-Yu Hung^{a,*}, Yu Bai^b, Tomotsugu Shimokawa^c, Nobuhiro Tsuji^{b,d},

Mitsuhiro Murayama^{a,e*}

^a Department of Materials Science and Engineering, Virginia Tech, Blacksburg, VA 24061, USA

^b Department of Materials Science and Engineering, Kyoto University, Yoshida-honmachi, Sakyo-ku, Kyoto 606-8501, Japan

^c Department of Mechanical Engineering, Kanazawa University, Kanazawa, Ishikawa, 920-1192, Japan

^d Elements Strategy Initiative for Structural Materials (ESISM), Kyoto University, Yoshida-honmachi, Sakyo-ku, Kyoto 606-8501, Japan

^e Institute for Materials Chemistry and Engineering, Kyushu University, Kasuga, Fukuoka 816-8580, Japan

This Chapter has been published in Scientific Reports, 2021, Volume 11, Article number: 8648.

This chapter is licensed under a Creative Commons Attribution 4.0 International License. To view a copy of this license, visit <http://creativecommons.org/licenses/by/4.0>.

Abstract

In polycrystalline materials, grain boundaries are known to be a critical microstructural component controlling material's mechanical properties, and their characters such as misorientation and crystallographic boundary planes would also influence the dislocation dynamics. Nevertheless, many of generally used mechanistic models for deformation twin nucleation in fcc metal do not take considerable care of the role of grain boundary characters. Here, we experimentally reveal that deformation twin nucleation occurs at an annealing twin ($\Sigma 3\{111\}$) boundary in a high-Mn austenitic steel when dislocation pile-up at $\Sigma 3\{111\}$ boundary produced a local stress exceeding the twinning stress, while no obvious local stress concentration was required at relatively high-energy grain boundaries such as $\Sigma 21$ or $\Sigma 31$. A periodic contrast reversal associated with a sequential stacking faults emission from $\Sigma 3\{111\}$ boundary was observed by in-situ transmission electron microscopy (TEM) deformation experiments, proving the successive layer-by-layer stacking fault emission was the deformation twin nucleation mechanism, different from the previously reported observations in the high-Mn steels. Since this is also true for the observed high Σ -value boundaries in this study, our observation demonstrates the practical importance of taking grain boundary characters into account to understand the deformation twin nucleation mechanism besides well-known factors such as stacking fault energy and grain size.

4.1 Introduction

Deformation by twinning in face centered cubic (fcc) metals has been studied extensively since 1950's, however, besides the stacking fault energy (SFE), the details of governing factors to determine the operative deformation twin nucleation mechanism have yet to be shown. Austenitic high-manganese (Mn) steels with a single fcc matrix phase are one of representative alloy systems for the twinning induced plasticity (TWIP) ¹⁻⁵, and it is suitable to study the SFE - deformation behavior correlation due to its ability to tune the SFE by adjusting the alloys' chemical compositions and its industrial value. Recent in-situ transmission electron microscopy studies ⁶⁻⁸ have demonstrated that deformation mechanism in high-Mn steels changes according to the SFE of the alloys. Deformation twin nucleation associated with both perfect and Shockley partial dislocations was observed in a low SFE high-Mn alloy (SFE ~ 12 mJ/m²), whereas plastic deformation was governed by planar dislocation glide in a high SFE counterpart (SFE ~ 85 mJ/m²). It is commonly believed that high-Mn steels are roughly categorized into three groups based on their SFE, i.e., low-SFE (< 20 mJ/m²), medium-SFE ($20 \sim 40$ mJ/m²) and high-SFE (> 40 mJ/m²). The level of SFE changes the deformation twinning nucleation by changing dislocation dissociation behavior thus it influences the strain hardening response of high-Mn TWIP steels. On the other hand, the high SFE case indicates that the SFE may not be the sole governing factor when compared these results with the deformation behavior of pure fcc metals such as copper (SFE ~ 70 mJ/m²).

Similarly, grain size is known to influence the operative deformation mode of the high-Mn TWIP steels by altering the nucleation site of carriers of plastic deformation, i.e., dislocations, deformation twins, and martensitic transformation ⁹⁻¹². The reasons for the deformation mode change are not fully understood, but may be attributed to the nature of grain boundaries and their

role of deformation twin nucleation, in addition to the volume confinement effect on the grain-interior dislocation source activity, known as dislocation source hardening ^{13,14}.

So far, there are five proposed deformation twin nucleation mechanisms applicable to high-Mn TWIP steels: that are Venables pole mechanism ¹⁵, Fujita-Mori stair-rod cross-slip mechanism ¹⁶, Cohen-Weertman-Frank cross-slip mechanism ¹⁷, Miura-Takamura-Narita primary slip mechanism ¹⁸, and Mahajan-Chin three-layer faults mechanism ¹⁹. They are based on microstructure investigations by transmission electron microscopy (TEM) and commonly indicate a) a sufficient dislocation density in a grain and/or local stress concentration as essential prerequisites, and b) an arrangement of highly coordinated Shockley partial dislocations glide on $\{111\}$ slip planes, are the key features of the deformation twinning process. Meanwhile, none of these mechanisms extensively argued the role of grain boundary, i.e., grain boundary characters. Historically, experimental observations focused on deformation twin nucleation behavior on $\{111\}$ twin boundaries, because the annealing twin boundaries are most likely sites for deformation twin nucleation based on electron backscattered diffraction (EBSD) analyses ²⁰. However, a recent work indicates that the deformation twins are nucleated from the vicinity of a grain boundary rather than exactly at the grain boundary based on a series of selected area electron diffraction (SAED) analyses ²¹. Generally speaking, grain boundary structure and misorientation affect various physical properties of materials including plasticity ²²⁻³⁰. The structural units and their sequences within a grain boundary also significantly affect the dislocation nucleation process, thus these factors are expected to be influential to the nucleation site of carriers of plastic deformation as much as the SFE and grain size. A recent computational study indicates that intergranular interactions could influence the local strain distribution and strain transfer near grain boundary ³¹, leaving open questions, i.e., whether the grain boundary

character such as misorientation and boundary plane structure would regulate i) the deformation twinning nucleation mechanisms associated with a grain boundary and ii) dislocation dynamics and the deformation twinning precursor structure near/at the grain boundary.






This study aims to clarify the correlation between the grain boundary character and deformation twin nucleation mechanism, and to directly observe the nucleation process of deformation twin precursor in near/at grain boundary region. A coarse-grained Fe-31Mn-3Al-3Si (wt.%) high manganese TWIP steel ($SFE = 40 \text{ mJ}\cdot\text{m}^{-2}$) was used as a model alloy for medium SFE high-Mn steel, the deformation twin nucleation mechanism at a low-energy $\Sigma 3\{111\}$ and several high sigma-value boundaries were investigated.

4.2 Results

EBSA analyses showed that nearly 40% grain boundaries in this alloy were identified as $\Sigma 3\{111\}$ (twin) boundary by taking more than 200 grain boundaries into account. The $\Sigma 3\{111\}$ boundaries indicated were determined as the $[111]/60^\circ$ axis/angle pair, which were basically annealing twin boundary. A histogram in Supplementary **Fig. S1** indicates the population of coincidence site lattice (CSL) boundaries having a certain axis/angle pair obtained by EBSA analysis³². Besides $\Sigma 3\{111\}$, the sum of all other CSL boundaries ($\Sigma 5$ to $\Sigma 49$) over the total boundaries was estimated to be 6%. Since $\Sigma 3\{111\}$ boundary is the dominant type boundary in this alloy and also predominantly discussed in previous studies, its deformation behavior will be carefully examined and compared with that of high-sigma value counterparts.

Symbols used in TEM images are listed in **Table 4.1**. Each of symbols indicates the direction of reciprocal lattice g-vector excited to image, streak in electron diffraction pattern, dislocation gliding direction, stacking faults, and dislocations.

Table 4.1. List of symbols used in TEM images

Symbol	Description
	g-vector direction
	streak (in electron diffraction pattern)
	dislocation gliding direction
	stacking fault
	dislocation

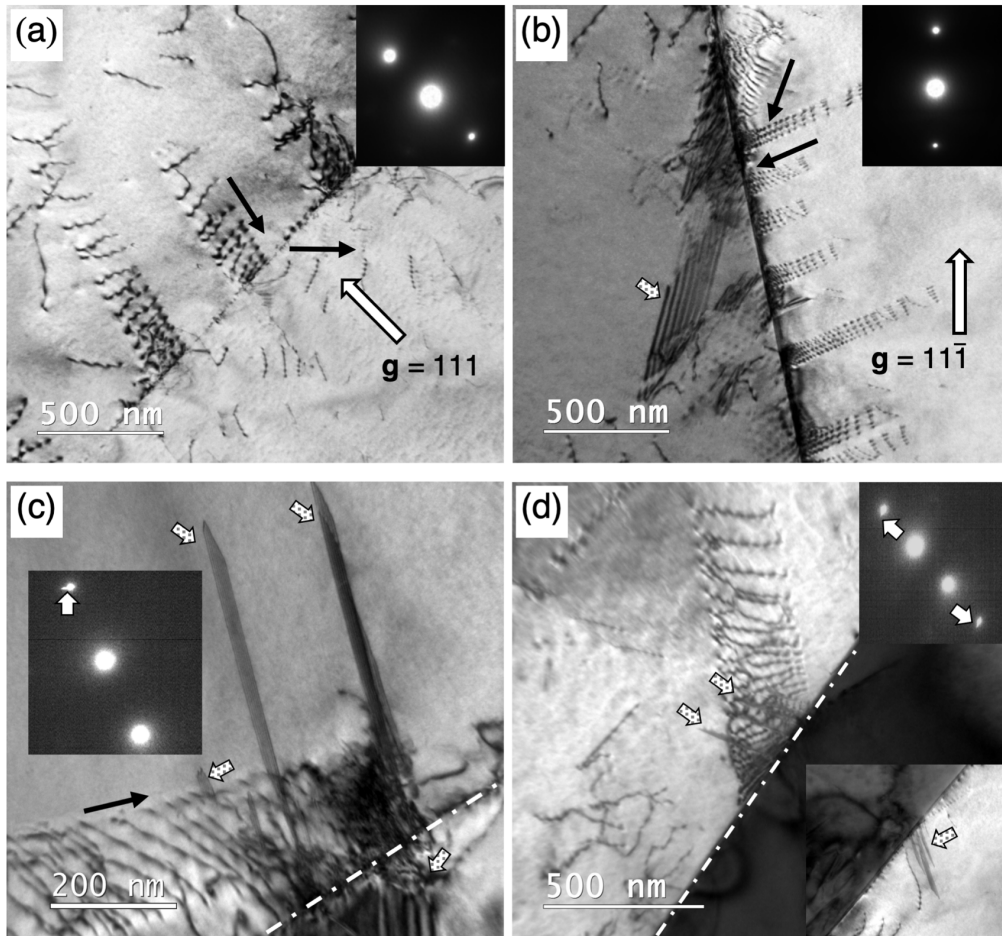


Figure 4.1 BF TEM micrographs showing the representative microstructure and structural defects in the TWIP steel deformed to engineering strain of 0.01 (a, b) and 0.02 (c-d). (a) Dislocations gliding and inducing the slip transfer from the starting grain to the twinned grain, taken in a two-beam condition for $g = 111$. (b) A stacking fault near the annealing twin boundary (indicated by an arrow filled with dots) and several dislocations in the right-side grain impinged the annealing twin boundary, taken in a two-beam condition for $g = 11\bar{1}$. (c, d) Dislocations pile-ups and stacking faults nucleation observed near an annealing twin boundary. The emitted stacking faults are indicated by the arrows filled with dots. The corresponding SAED patterns in (c, d) show a fine streak (white arrows), attributed to the shape factor of a planar fault.

Annealing twin ($\Sigma 3\{111\}$) boundaries

Bright field (BF) TEM images of $\Sigma 3\{111\}$ (annealing twin) boundaries after deformed to engineering tensile strains of 0.01 and 0.02 were taken at different two-beam diffraction conditions in **Fig. 4.1**. Each image shows different grain boundary – dislocation interactions in or near boundaries. **Fig. 4.1(a)**, the operative reciprocal lattice vector $\mathbf{g} = 111$, illustrates dislocations gliding and inducing the slip transfer from the upper-left starting grain to the lower-right twinned grain, i.e., a continuous slip transfer across the $\Sigma 3\{111\}$ boundary. In contrast, **Fig. 4.1(b)**, the operative reciprocal lattice vector $\mathbf{g} = 11\bar{1}$, shows a stacking fault (indicated by an arrow filled with dots) near a $\Sigma 3\{111\}$ boundary in the left grain and dislocations impinged on the opposite side of the boundary, i.e., the formation of stacking faults. It should be noted that the dislocations' gliding direction shown in black arrows were estimated from the changes in their curvature.

The continuous slip transfer across grain boundary could take place when the line of intersection defined by incoming and outgoing slip planes on the grain boundary is colinear and the Burgers vectors of screw dislocations of incoming and outgoing slip systems are identical³³. On the other hand, the stacking fault nucleation at the site where the non-screw dislocations impinged may take place when non-screw dislocations get incorporated into the grain boundary^{34,35}. It is worth noting that the continuous slip transfer across a $\Sigma 3\{111\}$ boundary was rarely observed in this study compared with the stacking fault nucleation. This may suggest that dislocations reached and impinged at annealing twin boundary tend to have an edge component rather than pure screw.

At an engineering strain of 0.02, larger number of planar defect like contrasts were observed near grain boundaries. The planar defects in **Fig. 4.1(c, d)** (arrows filled with dots) were clarified

to be stacking faults by examining their fringe contrast and weak streaks arising in selected area electron diffraction (SAED) patterns. The formation of stacking faults in this strain level was observed on the both sides of a $\Sigma\{111\}$ grain boundary. These deformation induced stacking faults are expected to transform into deformation twins through a sequential formation of Shockley partial dislocations on the $\{111\}$ slip planes if the sample will continuously be deformed as reported by previous studies^{36,37}.

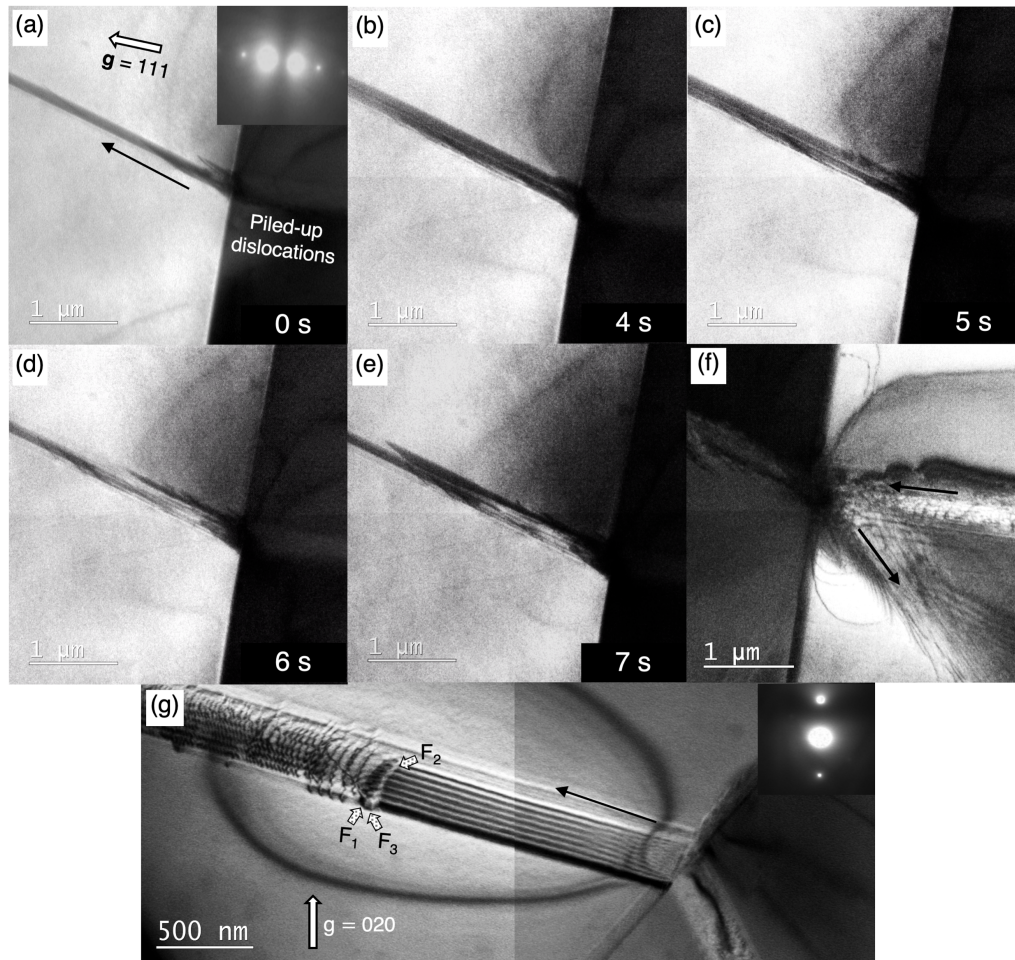


Figure 4.2 Selected frames of an in-situ deforming TEM test video data (see the original video, Supplementary **Video S1** online) showing a near annealing twin boundary region. The video was recorded in the two-beam condition for $g = 111$. (a) The initial stage of stacking faults emission event. (b-e) A continuous emission of stacking faults from the $\Sigma 3\{111\}$ boundary. The periodic contrast change was observed during the deformation. (f) The adjacent grain shows piled-up dislocations impinging on the $\Sigma 3\{111\}$ boundary and a local stress concentration field near grain boundary region. (g) A magnified view shows another stacking fault nucleated from a different $\Sigma 3\{111\}$ boundary taken in the two-beam condition for $g = 020$, near a $[102]_{fcc}$ zone axis. The fringe contrast changes were indicated by the arrows filled with dots (F_1, F_2, F_3).

Fig. 4.2 (a-e) are selected frames extracted from an in-situ TEM tensile test video (see the original video from the Supplementary **Video S1** online) and **(f)** is an additional BF TEM image taken at the end of the test with holding the applied stress. In the initial stage of deformation, a sequential stacking fault nucleation from a $\Sigma 3\{111\}$ boundary was observed **(a-e)**. This successive overlapping stacking fault emission event was evident based on the periodic changes

in the image contrast and forward moving leading Shockley partial dislocation contrast (e.g., **Fig.4.2(e)**). Consequently, this sequential stacking fault nucleation will generate the three-layered stacking faults, which is the precursor of a deformation twin. This process is schematically illustrated in Supplementary **Fig. S2** in Supplementary information. A localized stress concentration field caused by piled-up dislocations exists on the opposite side of the grain boundary as shown in **Fig. 4.2(f)**. Several secondary slip systems were activated as a result of piled-up dislocations interacted with the $\Sigma 3\{111\}$ boundary, reflecting the cumulative effect of the residual grain boundary dislocation buildup.

Fig. 4.2(g) shows a magnified view of a similar stacking fault nucleated from a different $\Sigma 3\{111\}$ boundary taken in a two-beam condition near a $[10\bar{2}]_{\text{fcc}}$ zone axis with the operative reciprocal lattice vector $\mathbf{g} = 020$. The two-beam imaging condition exhibits a periodic dark / bright fringe in this wide stacking fault with few exceptions in the outer most fringes, i.e., F_1, F_2 , and F_3 . A periodic contrast reversal can be observed when the emission of closely spaced overlapping stacking faults lying on parallel (111) planes occurred from a grain boundary because of the phase angle change³⁸. Every third set of fringes results in no-contrast because the phase angle α is changed by $\pm 2/3\pi$ every time a single-layered stacking fault passing by, i.e., $\alpha = 3 \times \pm 2/3\pi = \pm 2\pi$. The fault scheme- F_1 represents a single-layered stacking fault while an opposite (bright) contrast of F_2 corresponds to two-layered stacking fault. The F_3 showing zero contrast represents the three-layered stacking faults. This image, therefore, supports the nucleation process illustrated in Supplementary **Fig. S2** in Supplementary information and we conclude the reason for the periodic contrast reversal in Supplementary **Video S1** online is attributed to the layer-by-layer emission of individual leading Shockley partial dislocations lying on adjacent slip planes from the $\Sigma 3\{111\}$ boundary.

The formation of three-layered stacking faults on consecutive (111) planes changes the stacking sequence of original FCC of ABCABCABC to ABABCABCA, ABACABCAB and ABACBCABC sequentially. In the first step, an intrinsic stacking fault is formed, i.e., changed the local FCC structure into the HCP one. The subsequent formation of second and third stacking faults are emitted onto one/two atomic layers above the former (111) plane in the second and third steps, respectively. As a result, a deformation twin having two (111) atomic layers was formed, indicated by red dash line in Supplementary **Fig. S2** (step-3)). The corresponding stacking fault images combined with each transformation schematic clearly elaborate how the emitted layer-by-layer leading Shockley partial dislocations evolve to a deformation twin.

High-angle boundaries

A non- $\Sigma 3$ {111} grain boundary acting as a dislocation source was observed in **Fig. 4.3**. These two beam BF-TEM images were taken from the grains on the both side of a high-angle grain boundary. The operative reciprocal lattice vectors were (a) $\mathbf{g} = 11\bar{1}$ and (b) $\mathbf{g} = 111$ and the engineering strain was 0.02. Both images indicated that dislocations or a stacking fault were nucleated from the grain boundary without the presence of a local stress concentration field near the nucleation site. The grain boundaries in **Fig. 4.3(a)** and **(b)** were identified to have a [459] / 44.2° axis/angle pair that is basically identical to $\Sigma 21$ boundary ([112] / 44.2°) as shown in the inset atomic structure model³⁹. The nucleation of stacking faults in/near the $\Sigma 21$ boundary could occur without having a local stress concentration field such as dislocation pile-ups in contrast to

the case of $\Sigma 3$ boundaries.

Figure 4.4 shows a propagation of deformation twinning across two dissimilar grain boundaries. The images were taken at the engineering strain of 0.046. Three grains were separated by two grain boundaries, i.e., a $\Sigma 3$ boundary lies between the grain I and II, whereas a high angle tilt $\Sigma 31$ boundary separates grains II and III. The twin planes of these deformation twins were identified to be $(11\bar{1})$ from the corresponding SAED pattern in **Fig. 4.4(c)**. Two deformation twins were attached to the well-defined $\Sigma 31$ boundary having a $[11\bar{1}] / 18^\circ$ axis

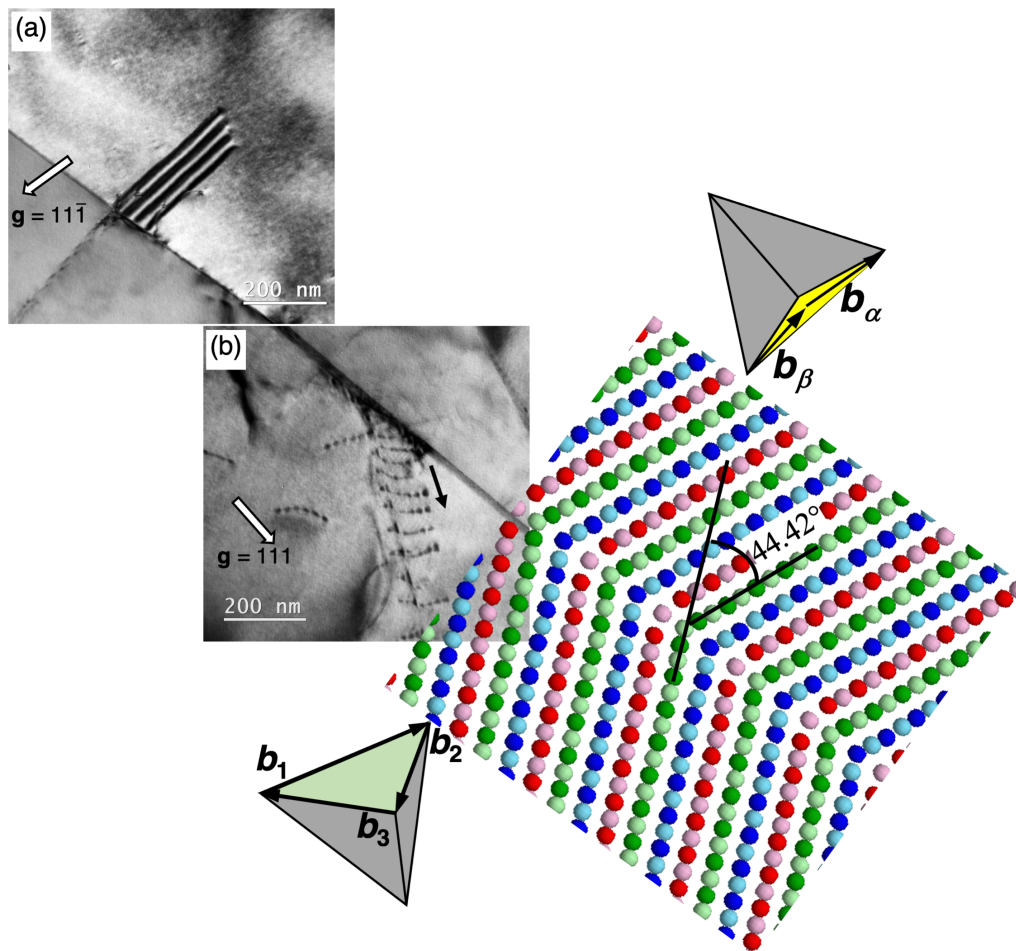


Figure 4.3 An experimentally observed $\Sigma 21$ boundary is superimposed onto the $[112]$ $\Sigma 21$ boundary structure model extracted from the ref. ³⁹. This $\Sigma 21$ boundary was defined to have a $[112] / 44.42^\circ$ axis/angle pair, which grain-boundary structure is composed of one structural unit A from $\Sigma 1$ boundary and two structural unit B from $\Sigma 11$ boundary. The perfect dislocation having Burgers vector of b_1 or b_2 or b_3 was emitted to bottom grain, while the partial dislocation having Burgers vector of b_α or b_β was emitted to the top grain.

angle pair. We assume that the $\Sigma 31$ boundary here serves as a heterogeneous nucleation site for the deformation twins because the coherent $\Sigma 3\{111\}$ boundary having a stable structural configuration is not energetically favorable to act as a dislocation source^{39,40} thus it requires a local stress concentration field to nucleate a stacking fault which does not exist here.

On the other hand, the emission of stacking faults in the grain-I could be a result of the deformation twin impingement on the $\Sigma 3\{111\}$ boundary, which would generate a local stress concentration. This is similar to the stacking faults nucleation associated with dislocation pile-ups against a $\Sigma 3\{111\}$ boundary (**Fig. 4.1(b, d)**). In response to the localized stress at the grain boundary, the incoming Shockley partial dislocations originated from the $\Sigma 31$ boundary could dissociate into the grain boundary dislocations which can be seen in **Fig. 4.4(b)**, and Shockley partial dislocations trailing a stacking fault in the adjacent grain-I. The identification of the stacking fault was based on its fringe contrast and weak streaks in SAED pattern in **Fig. 4.4(a)**. It appears that stress localization caused by planar defects impingement at the $\Sigma 3\{111\}$ boundary could be accommodated by emitting new planar defects to the adjacent grain.

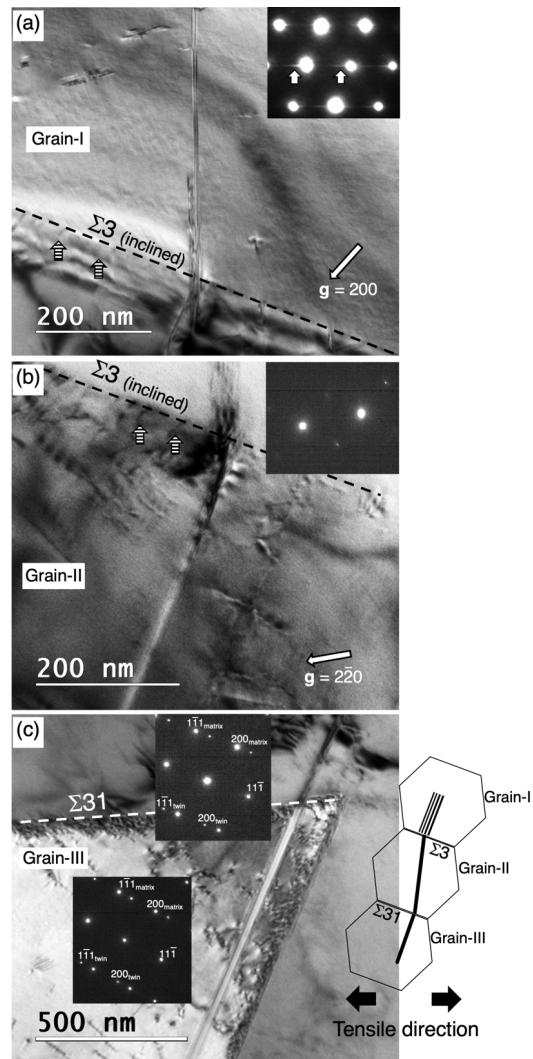


Figure 4.4 (a) A BF TEM image shows a stacking fault in the impingement region of an inclined $\Sigma 3\{111\}$ boundary. The inset SAED pattern shows faint streaks ascribed to the shape factor of the stacking fault. (b) A deformation twin emitted from the $\Sigma 31$ boundary impinging on the $\Sigma 3\{111\}$ boundary. Several impingement-induced grain boundary dislocations are indicated by striped arrows. (c) Deformation twins were nucleated from a $\Sigma 31$ boundary. The inset $[0\bar{1}\bar{1}]$ zone axis SAED patterns were taken from each of fine deformation twins. A schematic illustration is provided to indicate the geometrical relationship of two twinned grains (Grain-II and Grain-III) and one grain having a stacking fault (Grain-I).

Similar to the $\Sigma 21$ boundary's case, a $\Sigma 73$ boundary where the adjoining lattices are tilted by 41.4° rotation angle about the $[010]$ axis, was found to act as a dislocation source during plastic deformation as shown in the selected frames from an in-situ TEM deformation test video in **Fig. 4.5** (see the original video in Supplementary **Video S2** online). The misorientation of this grain boundary was identified from the EBSD analysis implemented prior to the in-situ deformation experiment. The experiment was conducted in a two-beam condition with the operative reciprocal lattice vector $\mathbf{g} = 200$ near a $[001]_{\text{fcc}}$ zone axis, and at a slightly higher magnification than **Fig. 4.2** to clarify the details of the nucleation behavior (see Supplementary **Video S2** online). In **Fig. 4.5(a)**, an intrinsic stacking fault with a dark outer fringe was observed.

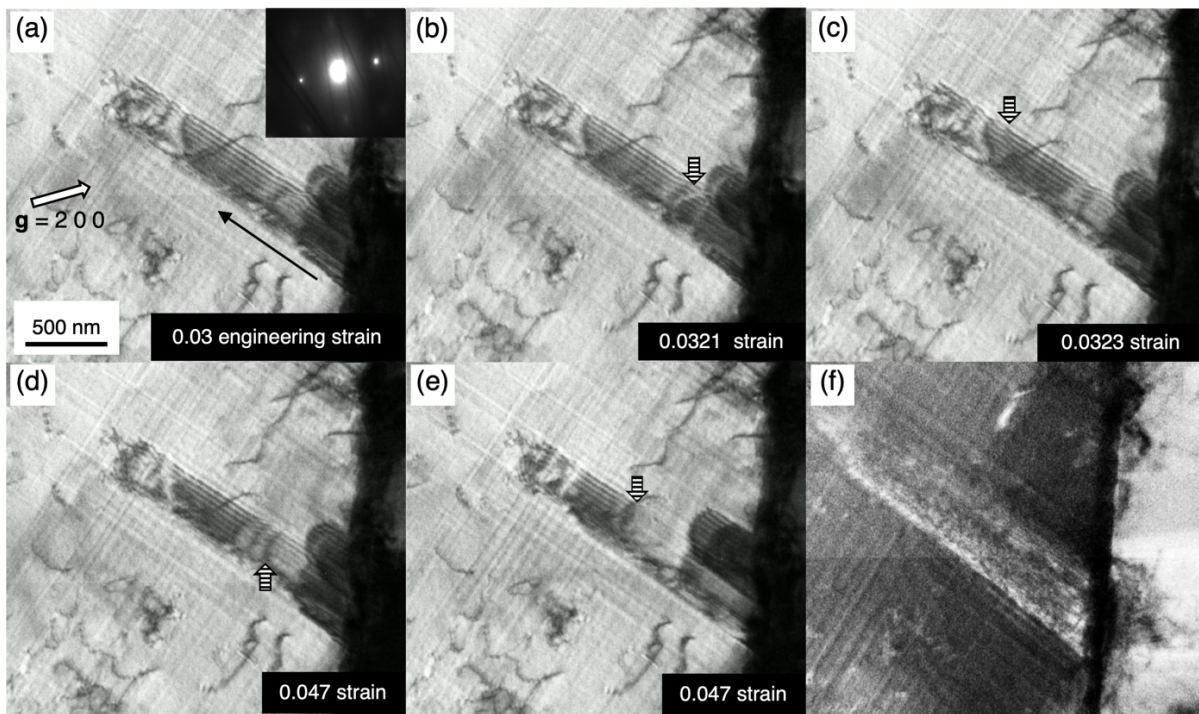


Figure 4.5 Selected frames of an in-situ deformation TEM test video (see Supplementary **Video S2** online) showing near a $\Sigma 73$ boundary region where the continuous stacking fault emission occurred. The images were recorded in a two-beam condition for $\mathbf{g} = 200$. (a) An intrinsic stacking fault having the dark outer fringe. (b, c) A leading partial dislocation emitted from the grain boundary gliding away on an adjacent slip plane, indicated by striped arrow. It results in two stacking faults overlapped (reversal fringe contrast, i.e., white outer fringe). (d, e) The third leading partial dislocation emitted from the grain boundary into the adjacent fault plane (indicated by the striped arrows) caused a three-layer deformation twin being out of contrast. (f) A near grain boundary region of the adjacent grain shows no dislocation pile-ups. A faint contrast induced by the grain boundary itself was visible.

During the plastic deformation, another leading Shockley partial dislocation (striped arrow) on the adjacent parallel fault plane was generated from the grain boundary (**Fig. 4.5(b)**). As the leading Shockley partial dislocation continuously glide away from grain boundary (**Fig. 4.5(c)**), the outer fringe contrast turned from dark to bright, i.e., two stacking faults were overlapped. Soon after that, the next emission of leading Shockley partial dislocation made the fringe contrast none (**Fig. 4.5(d, e)**) due to an effective transition vector value $R = 3 \times 1/3 (111)$ is equivalent to that of a perfect lattice. These successive emission events are fast and a three-layered stacking fault, the precursor of deformation twin, formed as a consequence. Our two in-situ TEM experiments indicate that the mechanism of the deformation twin precursor is identical in both $\Sigma 3 \{111\}$ and $\Sigma 73$ boundaries; both are by the sequential stacking fault emission mechanism.

4.3 Discussion

The deformation behavior of this medium-SFE TWIP steel at/near grain boundaries appears to be similar to that in low SFE (SFE ~ 12 mJ/m²) TWIP steels rather than the high SFE (SFE ~ 85 mJ/m²) counterparts⁶, i.e., the main carrier of plastic deformation is deformation twins and stacking faults rather than dislocation in these areas, and the deformation twin nucleation was associated with both perfect and Shockley partial dislocations. Our observations indicate that the deformation twins having two (111) atomic layers were formed by a sequential emission of stacking faults from grain boundaries, which is different from the conventional Mahajan-Chin three-layer mechanism¹⁹.

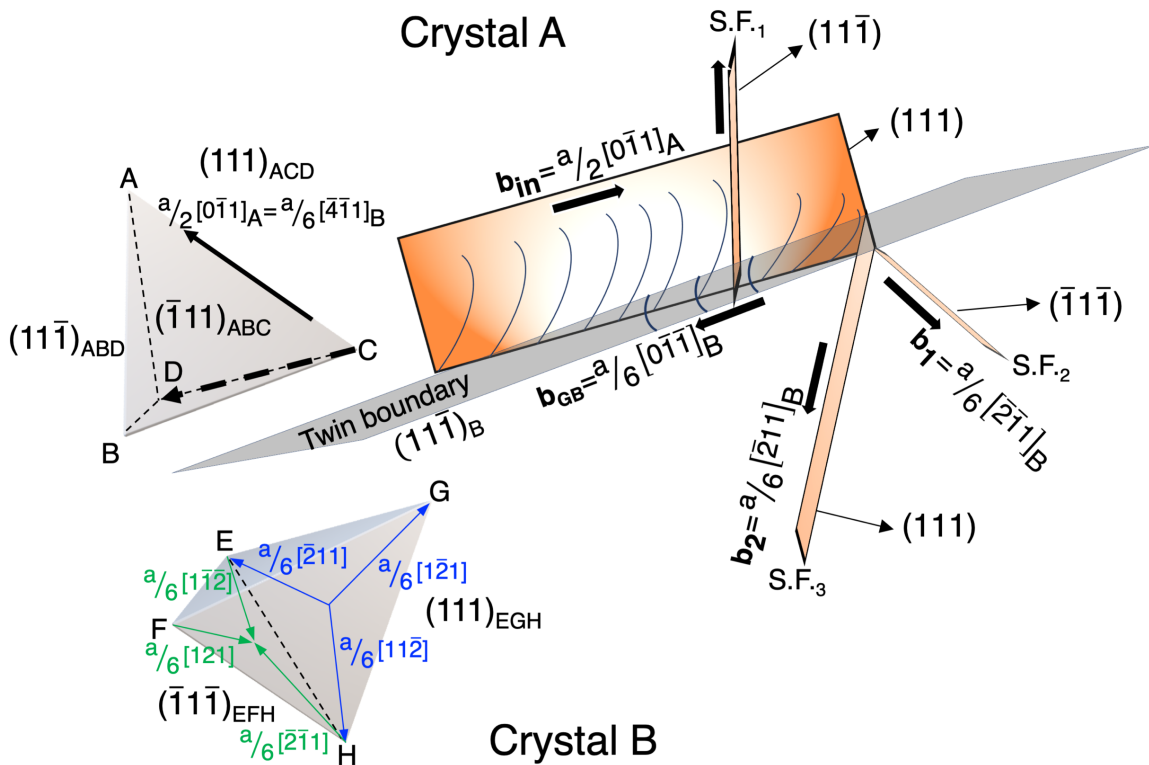


Figure 4.6 A schematic illustration shows the precursors of deformation twin are initiated at a near grain boundary region as a result of the impingement between piled-up dislocations and an annealing twin boundary. The stacking fault S.F.₁ is formed by a cross-slip dislocation reaction. S.F.₂ and S.F.₃ are formed by a grain boundary stress relaxation reaction. The Burgers vector of incoming dislocations b_{in} was designated to be $a/2 [0\bar{1}1]_A$ or $a/6 [\bar{4}\bar{1}1]_B$ after a proper matrix transformation, whereas the Burgers vectors of b_1 and b_2 were assumed to be two Shockley partial dislocations ($a/6 [\bar{2}\bar{1}1]_B$ and $a/6 [\bar{2}\bar{1}1]_B$) that are emitted to minimize the magnitude of Burgers vector of grain boundary dislocations.

Piled-up dislocations at a grain boundary could trigger twin formation to accommodate the localized stress concentration⁴¹⁻⁴⁴, and annealing twin ($\Sigma 3$) boundary appears to be the most favorable deformation twin nucleation site especially those in a grain which a $\langle 111 \rangle_{fcc}$ orientation is parallel to the tensile axis²⁰. The piled-up dislocations assisted deformation twin nucleation at a $\Sigma 3 \{111\}$ boundary can be a two-step process, i.e., Step-1: a stress concentration relaxation event at the annealing twin boundary when a group of dislocations are piled-up, which followed by Step-2: emitting stacking faults on successive slip planes that will be evolving into a deformation twin.

The first step can be explained by the dislocation - $\Sigma 3\{111\}$ boundary interaction schematically summarized in **Fig. 4.6**, which is basically representing the case in **Fig. 4.1(c)**. Incoming dislocations interacting with a $\Sigma 3\{111\}$ boundary leave more than one stacking fault on the both sides of the $\Sigma 3\{111\}$ boundary. It has been a generally accepted understanding that a coherent $\Sigma 3\{111\}$ boundary is not acting as a proactive dislocation source because of its coherent atomic arrangement^{39,40,45-49}, which is different from grain boundaries consisting of long-period structure units. However, the interaction between $\Sigma 3\{111\}$ boundary and incoming dislocations (\mathbf{b}_{in}) could trigger different reactions at the grain boundary. As seen in **Fig. 4.6**, dislocations approaching the $\Sigma 3\{111\}$ boundary could make cross-slip and transfer to the adjacent grain only when the incoming dislocations contain a specific Burgers vector, illustrated as \overline{CD} in the Thompson tetrahedron ABCD. Otherwise, the incoming dislocations (\mathbf{b}_{in}) would be obstructed by the $\Sigma 3\{111\}$ boundary and inevitably encounter an energy barrier of which strength is related to the SFE of the alloy, thus, a certain amount of energy is required to compress Shockley partial dislocations at the boundary. The process of compressing a pair of Shockley partial dislocations into a perfect dislocation on the $\Sigma 3\{111\}$ boundary gradually builds up a large stress field in/near the boundary regions, which obstructs the entry of additional incoming dislocations thereby stimulating the dislocation pile-ups and will lead to two possible deformation twinning behavior. First, the incoming dislocations may start to dissociate into Shockley partial dislocations on the conjugate slip planes of the original grain due to the alloy's relatively low SFE characteristic, which could be the case appeared in **Fig. 4.1 (c-d)** and **Fig. 4.2(f)**. The nucleation of stacking faults of S.F.1 in the original grain is the result of dislocation dissociation, i.e., the incoming dislocations dissociate into the Shockley partial dislocations lying on the conjugate slip plane by the Cohen-Weertman or Fujita-Mori cross-slip twinning mechanism, suggesting that the

deformation twinning behavior could occur in the vicinity of grain boundaries.

Second, the leading piled-up dislocation attached to the $\Sigma 3\{111\}$ boundary is required to dissociate its Burgers vector into multiple components in order to decrease the dislocation pile-up caused elastic strain energy in the neighbor grain region. A theoretical study of dislocation - $\Sigma 3\{111\}$ boundary interaction in aluminum, copper, and nickel by molecular dynamics simulation indicates that the outgoing slip mechanism to an adjacent grain, associated with dislocation decomposition in a $\Sigma 3\{111\}$ boundary, depends on the relationship between the mechanical factor, i.e., resolved driving force, and the material factor, i.e., lattice resistance for re-nucleating partial dislocations determined by the plane fault energies³⁵. Although the actual internal and external stress components around the $\Sigma 3\{111\}$ boundary are not measurable easily, the outgoing Shockley partial dislocations (\mathbf{b}_1 and \mathbf{b}_2) into Crystal-B along with S.F.2 and S.F.3 (**Fig. 4.6**) must receive a larger resolved driving force than that on the Shockley partial dislocation on the $\Sigma 3$ boundary due to the stress concentration by the dislocation pile-up. It suggests that creating partial dislocations into an adjacent grain seems to be a more favorable path in response to the localized stress field induced by the dislocation pile-ups at the $\Sigma 3\{111\}$ boundary.

Minimizing the magnitude of Burgers vector of the residual dislocations left in a grain boundary is generally believed to be the most dominant criterion to determine which slip system will be activated from the grain boundary in response to a local stress concatenation^{33,50-52}. After a strong dislocation - grain boundary interaction, the grain boundary dislocations having a large magnitude of Burgers vector would be unfavorable, thus the dissociated leading Shockley partial dislocations were emitted from the grain boundary in response to the unstable grain boundary structure. The Burgers vector of residual grain boundary dislocations can be determined by the

following relationship:

$$\mathbf{b}_{GB} = \mathbf{b}_{in} - \mathbf{b}_{out} \quad (5)$$

, where \mathbf{b}_{GB} is the difference between the incoming and outgoing dislocations' Burgers vectors, \mathbf{b}_{in} and \mathbf{b}_{out} , respectively. The \mathbf{b}_{in} , $a/2 [0\bar{1}1]_A$ in Crystal-A or $a/6 [\bar{4}\bar{1}1]_B$ after a proper coordinate transformation in Crystal-B, can be characterized by the $\mathbf{g}\cdot\mathbf{b}$ criterion. On the other hand, the \mathbf{b}_{out} in the adjacent grain cannot be resolved but the \mathbf{b}_1 and \mathbf{b}_2 must be the Shockley partial dislocations lying on $(\bar{1}1\bar{1})$ and (111) , respectively. i.e., $\pm a/6 [121]$, $\pm a/6 [\bar{2}\bar{1}1]$, or $\pm a/6 [1\bar{1}\bar{2}]$ for \mathbf{b}_1 , and $\pm a/6 [1\bar{2}1]$, $\pm a/6 [\bar{2}11]$, or $\pm a/6 [11\bar{2}]$ for \mathbf{b}_2 . While 36 possible combinations for the emitted Shockley partial dislocations are expected, two possible reactions can be considered by assuming the emitted Shockley partial dislocations would minimize the magnitude of Burgers vector of grain boundary dislocation:

$$\mathbf{b}_{GB} = a/6 [\bar{4}\bar{1}1]_B - \{a/6 [\bar{1}\bar{2}\bar{1}]_B + a/6 [\bar{2}11]_B\} = a/6 [\bar{1}01]_B \quad (6)$$

$$\mathbf{b}_{GB} = a/6 [\bar{4}\bar{1}1]_B - \{a/6 [\bar{2}\bar{1}1]_B + a/6 [\bar{2}11]_B\} = a/6 [0\bar{1}\bar{1}]_B \quad (7)$$

The $\mathbf{b}_{GB} = a/6 [\bar{1}01]_B$ in Eq. (6) contains the component perpendicular to the twin boundary $(11\bar{1})$, whereas the $\mathbf{b}_{GB} = a/6 [0\bar{1}\bar{1}]_B$ in Eq. (7) could freely slip on the twin plane. Thus, the Eq. (7) would be the most possible reaction in response to accommodate the incoming dislocations at the grain boundary.

Now, the second step of the deformation twin nucleation, consisting of the sequential emission of stacking faults on the successive slip planes, can be explained by the ratio of the intrinsic stacking fault energy and unstable stacking fault energy, $\gamma_{isf}/\gamma_{usf}$ ⁵³. The movement of leading Shockley partial dislocation requires to overcome the energy barrier γ_{usf} , while trailing Shockley partial dislocation encounters a much lower energy barrier associated with $\gamma_{usf} - \gamma_{isf}$. The effect of trailing Shockley partial dislocations on deformation twinning can be mitigated

when the difference between γ_{isf} and γ_{usf} is large enough to promote the formation of wide stacking faults as the deformation proceeded. The γ_{isf} of our alloy is around 40 mJ m^{-2} while the γ_{usf} is hard to estimate experimentally. However, the formation of stacking fault in the neighboring slip planes would experience the energy barrier which value may be similar to γ_{usf} ^{5,54,55}. A universal energy relationship of the planar fault energy barriers in many FCC metals would be:

$$\gamma_{utf} \cong \frac{1}{2} \cdot \gamma_{isf} + \gamma_{usf} \quad (8)$$

, where γ_{utf} is the energy needed to transform an intrinsic stacking fault to an extrinsic stacking fault. For low SFE metals, the $1/2 \gamma_{isf}$ term becomes negligible so that the γ_{utf} will be similar to γ_{usf} . The minimum energy path for continuous generation of planar faults such as intrinsic/extrinsic stacking faults and twins on neighboring slip planes could be achievable as long as the energy barriers γ_{usf} and γ_{utf} are conquerable. Our results indicate that dislocations pile-up is required to conquer the energy barriers at $\Sigma 3\{111\}$ boundaries whereas different types of boundaries could lower the energy barriers by its structural characteristics.

The deformation twinning behavior in high-sigma-value boundaries ($\Sigma 21$, $\Sigma 31$ and $\Sigma 73$) indicate that these boundaries could act as a dislocation source thus stacking faults and deformation twins can be nucleated directly from these in response to tensile deformation, which is different from what was observed in $\Sigma 3\{111\}$ boundary. Thus, the grain boundary character undoubtedly affects the deformation twin nucleation behavior, in addition to the SFE and geometrical grain orientation relative to the loading axis.

A grain boundary with a specific orientation can be constructed by combing delimiting grain boundaries⁵⁶; for example, a $[001]\Sigma 17$ tilt boundary can be composed from one structural unit

from $\Sigma 1$ boundary and two units from $\Sigma 5$ boundary, which is designated to be the $|ABB|$ periodic structure⁵⁷. The grain boundaries constructed by long-periodic structural units usually have a higher grain boundary energy^{39,40,49,58}. Computational studies^{39,57,58} demonstrate that the $[112]\Sigma 21$, $[11\bar{1}]\Sigma 31$, and $[001]\Sigma 73$ tilt boundaries can be described to be long-period boundaries, i.e., the extrinsic dislocations can be introduced to the boundaries to accommodate the misorientation angle deviated from the delimiting boundaries. The delimiting grain boundaries show the weakest trend of acting as a dislocation source³⁹ and the trend becomes even stronger as the boundary structure deviating from the delimiting one. Thus, the $[112]\Sigma 21$ boundaries bordering the stable $[112]\Sigma 11$ delimiting boundary could eventually transform to a relatively stable boundary structure by emitting dislocations and minimizing the magnitude of Burgers vector of grain boundary dislocations. As schematically shown in **Fig. 4.3**, a $[112]\Sigma 21$ boundary emits dislocations to both top and bottom grains. In this process, a perfect dislocation having Burgers vector of \mathbf{b}_1 or \mathbf{b}_2 or \mathbf{b}_3 will be emitted to the bottom grain, while a Shockley partial dislocation having Burgers vector of \mathbf{b}_α or \mathbf{b}_β will be emitted to the upper grain. The rotation axis of $[112]\Sigma 21$ boundary is aligned well with the dislocation lines of Shockley partials and perfect dislocations. Since the grain boundary structure transition utilizes the Burgers vector of grain boundary dislocations associated with the misorientation of that particular grain boundary, this rotation axis – dislocation line alignment observed in the top grain makes dislocation emission easier; this event is the same as that observed in a bicrystal model with a $\Sigma 21$ boundary under a uniaxial loading test by molecular dynamics simulation³⁹. On the other hand, the emitted dislocation line in the bottom grain is not parallel to the rotation axis, so that the dislocations are emitted not by using grain boundary dislocations, but by using free volume that does not exist in coherent boundaries such as $\Sigma 3\{111$. This asymmetrical phenomenon is probably caused by the

complicated multiaxial stress state around the grain boundary.

An atomic structure model was built to reproduce the geometrical relationship between Grains-I and -II in **Fig. 4.4(a)** and to evaluate the Schmid factor for possible slip systems in this particular geometry (see Supplementary **Fig. S3**). The Schmid factor for the stacking fault in the Grain-II is calculated to be 0.244, which is the third largest among the enabled partial dislocations in the Grain-II and would be reasonable when the $[11\bar{1}]\Sigma 31$ acts as the dominate dislocation source. The Schmid factor for the stacking fault nucleated from the $\Sigma 3$ boundary to the Grain-I is relatively low. Since the slip system having the largest Schmid factor was not activated, the propagation of the slip from the Grain-II could play a critical role in this particular case to propagate plastic deformation. Also notice that the possible direction of the Burgers vector nucleated from the $\Sigma 3\{111\}$ boundary to the Grain-I is almost opposite direction of the Burgers vector approaching to the $\Sigma 3\{111\}$ boundary in the Grain-II; hence, the residual Burgers vector at the $\Sigma 3\{111\}$ boundary after the dislocation transfer becomes large under the applied tensile stress. These considerations suggest that the applied tensile stress itself is not enough to make the slip propagation from the Grain-II to Grain-I, thus the stacking fault formation at the $\Sigma 3\{111\}$ boundary requires additional driving force such as local stress concentration.

Shockley partial dislocation emission was also observed in the $[11\bar{1}]\Sigma 31$ boundary in **Fig. 4.4(b)** and the $[001]\Sigma 73$ boundary in **Fig. 4.5**. The complicated multiaxial stress applied on these long-period grain boundary structures appear to stimulate the $[11\bar{1}]\Sigma 31$ and $[001]\Sigma 73$ boundaries act as a dislocation source, but whether the grain boundary structure transition involved in the dislocation emission process or free-volume assisted dislocation emission process cannot immediately be confirmed. Since the rotation axis of $\langle 111 \rangle$ and $\langle 001 \rangle$ boundaries have no direct relation with the dislocation line direction, the mechanism of dislocation emission for

$\langle 111 \rangle$ and $\langle 001 \rangle$ boundaries would be different from that for $\Sigma 21$ boundary. However, there is still a possibility that these boundaries also utilize their grain boundary dislocations for dislocation emission, or conquering energy barriers for deformation twin nucleation.

4.4 Conclusions

In this study, how grain boundary misorientation influences deformation twinning nucleation mechanism at grain boundaries in an Fe-31Mn-3Al-3Si TWIP steel was investigated by in-situ deformation TEM experiments followed by detailed crystallographic analysis.

- 1) Deformation twin nucleation at a $\Sigma 3\{111\}$ boundary occurs when a local stress concentration field at or near the boundary exceeds a twinning stress. $\Sigma 3\{111\}$ boundary can act as a strong barrier against dislocations and planar defects motion thus a local stress concentration field needs to be introduced by dislocations or planar defects piled-up against the $\Sigma 3\{111\}$ boundary. The influence of the barrier effect causing the deformation twin nucleation depends on the characteristics of the incoming dislocations to a $\Sigma 3\{111\}$ boundary. The deformation twin nucleation at a $\Sigma 3\{111\}$ boundary would not occur when the incoming dislocations made slip transfer across it.
- 2) Deformation twin nucleation at high angle grain boundaries such as $\Sigma 21$ or $\Sigma 31$ was not accompanied with a local stress concentration field caused by structural defects. Our microstructure observations indicate that high angle grain boundaries would spontaneously emit stacking faults because their long-period structure units contain lattice dislocation components accommodating the misorientation angle deviated from the delimiting boundaries.
- 3) Successive layer-by-layer stacking fault emission is found to be the deformation twin nucleation mechanism in this study at both low and high sigma value grain boundaries.

Deformation twins having two (111) atomic layers were formed by a sequential emission of leading Shockley partial dislocations from grain boundaries in our in-situ TEM experiments, which is different from the conventional Mahajan-Chin three-layer mechanism.

4.5 Materials and Methods

The chemical composition of the alloy is 31.0 Mn, 3.0 Al, 3.0 Si, 0.005 C, 0.004 N, 0.012 S (mass %) and balance Fe. As-received alloy was a hot-forged sheet with 12 mm thickness. Multi-pass cold rolling to 1 mm thick (92% rolling reduction in thickness) was conducted followed by a heat treatment at 950°C for 15 min. The sample with average grain size of 15.4 μm then was sectioned to a specific dimension, 13 \times 2 mm rectangular piece, and thinned mechanically from 1 mm to 150 μm . The foils were tensile-deformed to 0.01, 0.02 and 0.046 engineering strain respectively using a SEM testing stage (Kammrath and Weiss Module 5000 N) at a strain rate of $4.6 \times 10^{-4} \text{ s}^{-1}$ at room temperature.

The samples for TEM analysis were cut from the center of tensile-deformed samples to a specific dimension, 2 \times 2 mm square-shape, and then mechanically thinned to 70 μm thick. Thinning to electron transparency was achieved by using a twin-jet electropolisher (E.A. Fischione Model 110) with a 95% acetic acid and 5% perchloric acid electrolyte maintained at 17°C and the applied voltage, 38V. The transmission electron microscopy was then performed using a JEOL 2100 TEM operated at 200 kV.

The sample for in-situ deformation tests in TEM were prepared as same as the samples prepared for TEM analysis. The square-shape specimen was fixed on a cartridge-type blade on a SATO Holder Duo (Mel-Build Co.)⁵⁹. The strain rate in this study was controlled at approximately $6.7 \times 10^{-5} \text{ s}^{-1}$. In-situ tensile experiments were performed on a FEI Titan 300 TEM in the bright field mode, operated at 300kV. Videos were recorded using Gatan Orius SC200D

camera and Digital Micrograph with the high-resolution streaming video plug-in.

Acknowledgements

The authors would like to thank W. T. Reynolds at Virginia Tech for his valuable comments. This study was partly supported by Nanoscale Characterization and Fabrication Laboratory (NCFL), Institute for Critical Technology and Applied Science (ICTAS), Virginia Tech and used shared facilities at the Virginia Tech National Center for Earth and Environmental Nanotechnology Infrastructure (NanoEarth), a member of the National Nanotechnology Coordinated Infrastructure (NNCI), supported by NSF (ECCS 1542100, ECCS 2025151). N.T., T.S. and M.M. greatly appreciate the financial support by the JST CREST (JPMJCR1994). M.M. acknowledges a financial support by the DOE Basic Energy Science Program (BES DE-FG02-06ER15786) for technical development of TEM in-situ deformation, and JSPS KAKENHI Grant Numbers (No. 19H02029). N.T. acknowledges a financial support by Elements Strategy Initiative for Structural Materials (ESISM, No. JPMXP0112101000), and JSPS KAKENHI (No. 15H05767, No.20H00306), all through the Ministry of Education, Culture, Sports, Science and Technology (MEXT), Japan

Supplementary information

Grain misorientation measurement

A grain boundary can be defined by a misorientation angle and an axis (axis/angle pair) of grains on both side of the grain boundary. The Seyring's method¹ was taken here as a reference. In this study, to determine the orientation relationship, the orientation matrix with respect to the reference coordinate system of each grain has to be determined from its electron diffraction pattern. First, a double-tilt TEM holder was used to tilt the sample to a certain degree, which would bring both grains into its particular zone axis. It will be verified that zone axes characterized in the neighboring grains at similar stage tilts could be mapped into each other using a transformation matrix. Then, the diffraction pattern frame (X_p Y_p Z_p) was defined with the Z-axis parallel to the zone axis, the X-axis parallel to any indexed diffraction g-vector, and the Y-axis parallel to the zone-axis \times g, which can be expressed as followed:

$$\begin{bmatrix} X_p \\ Y_p \\ Z_p \end{bmatrix} = \begin{bmatrix} g \\ \text{zone axis} \times g \\ \text{zone axis} \end{bmatrix} \quad (1)$$

A reference frame (X_R Y_R Z_R), which lies on fluorescent screen and only differs from $\begin{bmatrix} X_p \\ Y_p \\ Z_p \end{bmatrix}$ by a

right-handed rotation of φ about zone axis, where φ is the angle between X_p and X_R . The

corresponding rotation matrix is

$$R = \begin{bmatrix} \cos \varphi & \sin \varphi & 0 \\ -\sin \varphi & \cos \varphi & 0 \\ 0 & 0 & 1 \end{bmatrix} \quad (2)$$

By combining the $\begin{bmatrix} X_p \\ Y_p \\ Z_p \end{bmatrix}$ and R, the matrix equivalent to the rotation from crystal to reference can

be expressed as :

$$\begin{bmatrix} X_R \\ Y_R \\ Z_R \end{bmatrix} = R \cdot \begin{bmatrix} X_p \\ Y_p \\ Z_p \end{bmatrix} \quad (3)$$

In order to be consistent to the definition made by Bunge ², the transpose of $R \cdot \begin{bmatrix} X_p \\ Y_p \\ Z_p \end{bmatrix}$ equivalent

to grain orientation matrix M that represents the rotation from reference to crystal frame. Finally, the misorientation matrix of two neighboring grains can be determined from their orientation matrix M₁ and M₂:

$$M_{12} = M_2^{-1} * M_1 \quad (4)$$

M₁₂ then can be transformed into an axis-angle pair with a proper transformation.

[1] Seyring, M., Song, X. & Rettenmayr, M. Advance in orientation microscopy: Quantitative analysis of nanocrystalline structures. *ACS Nano* 5, 2580–2586 (2011).

[2] Engler, O; Randle, V. *Introduction to Texture Analysis: Macrotecture, Microtexture and Orientation Mapping, second ed. Taylor & Francia, CRC Press, USA (2008).*

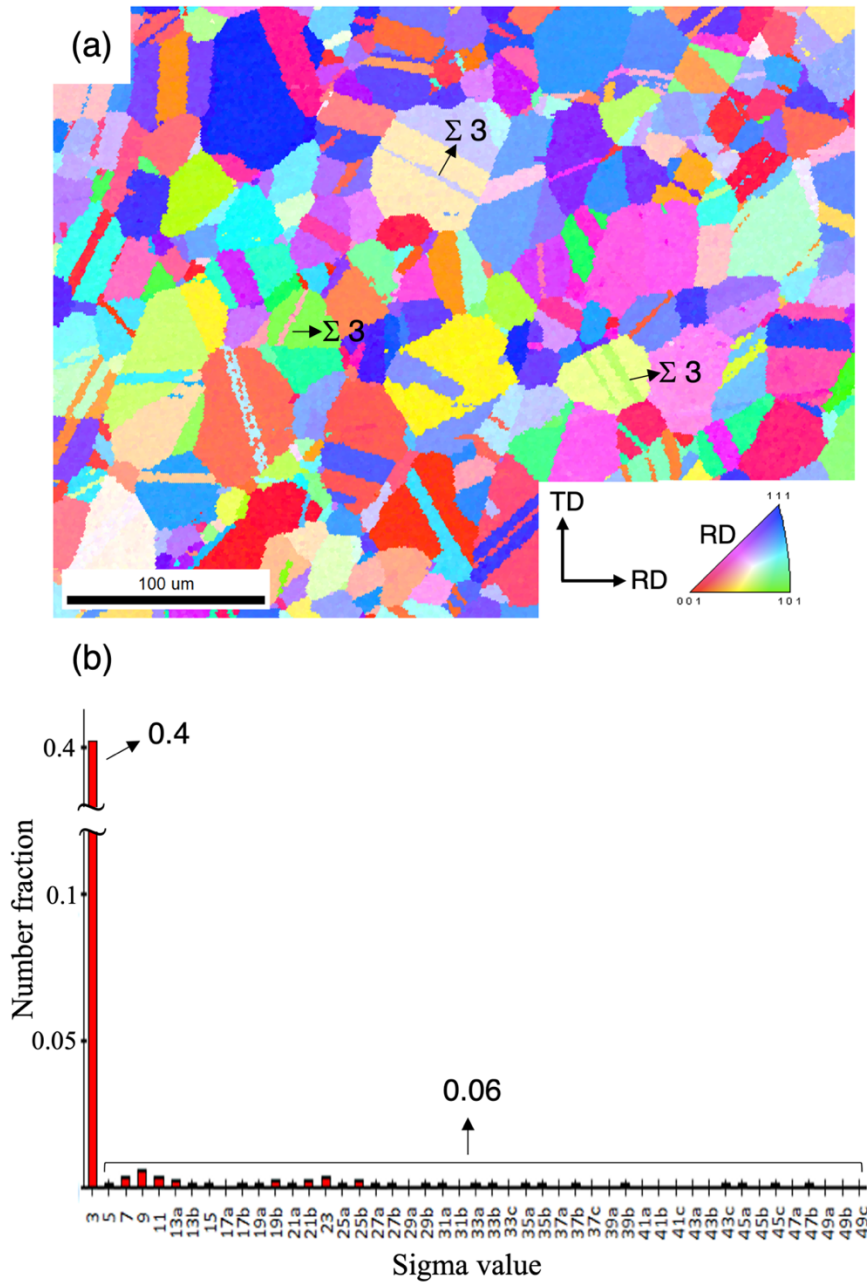


Fig. S1 The grain orientation of an as-received Fe-31Mn-3Al-3Si TWIP steel derived from EBSD. (a) An inverse pole figure (IPF) map indicates a fully recrystallized austenite single-phase structure. The crystallographic orientation is represented as parallel to sample rolling direction; three representative $\Sigma 3$ boundaries identified to have 111 / 60° axis/angle pairs are indicated by black arrows. (b) The population of coincidence site lattice (CSL) boundaries by taking more than 200 grain boundaries into account. The number fraction is defined to be the ratio of the number of a CSL grain boundary to the total number of grain boundaries; 0.4 for $\Sigma 3$ boundaries and 0.06 for the rest of CSL boundaries ranging from $\Sigma 5$ to $\Sigma 49$ sigma-value boundaries.

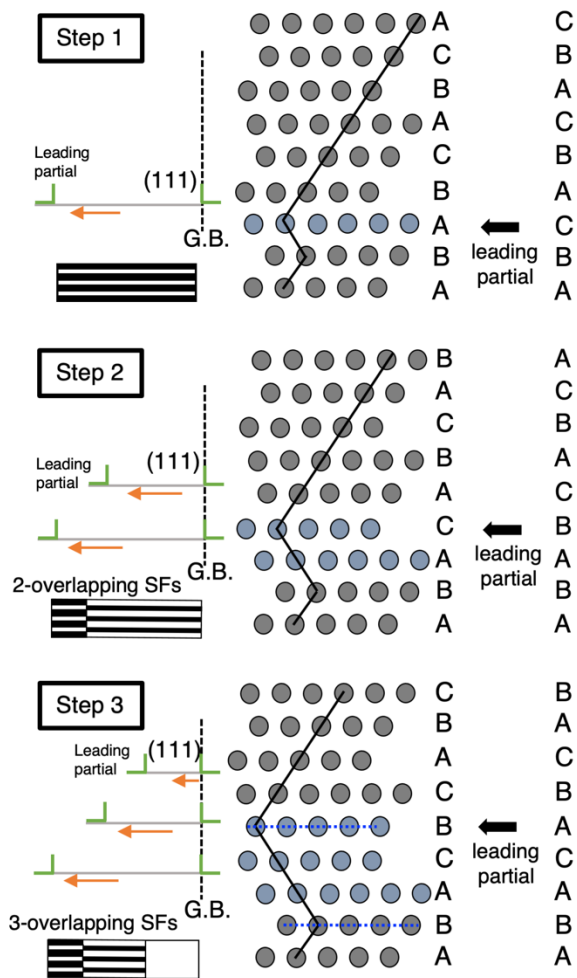


Fig. S2 Schematic illustrations show how fringe contrast reversal occurs by the successive layer-by-layer stacking fault emission. Since the planar defect was formed on a $\{111\}$ close-packed slip plane, the value of translation vector R could be a $1/3 \{111\}$ type, leading the phase angle for the F_1 , $\alpha = 4/3\pi$ equivalent to $\alpha = -2/3\pi$, to a dark outer fringe. When a second stacking fault was displaced on an adjacent fault plane, an extrinsic stacking fault would be formed with a phase angle, $\alpha = 2/3\pi$, which F_2 showed a reversal contrast when compared with F_1 . The presence of no-contrast F_3 is ascribed to three-layered stacking faults with an effective $R = 3 \cdot 1/3 (111)$, which acts like a perfect lattice vector and can therefore appear to give $2\pi g \cdot R = 0$.

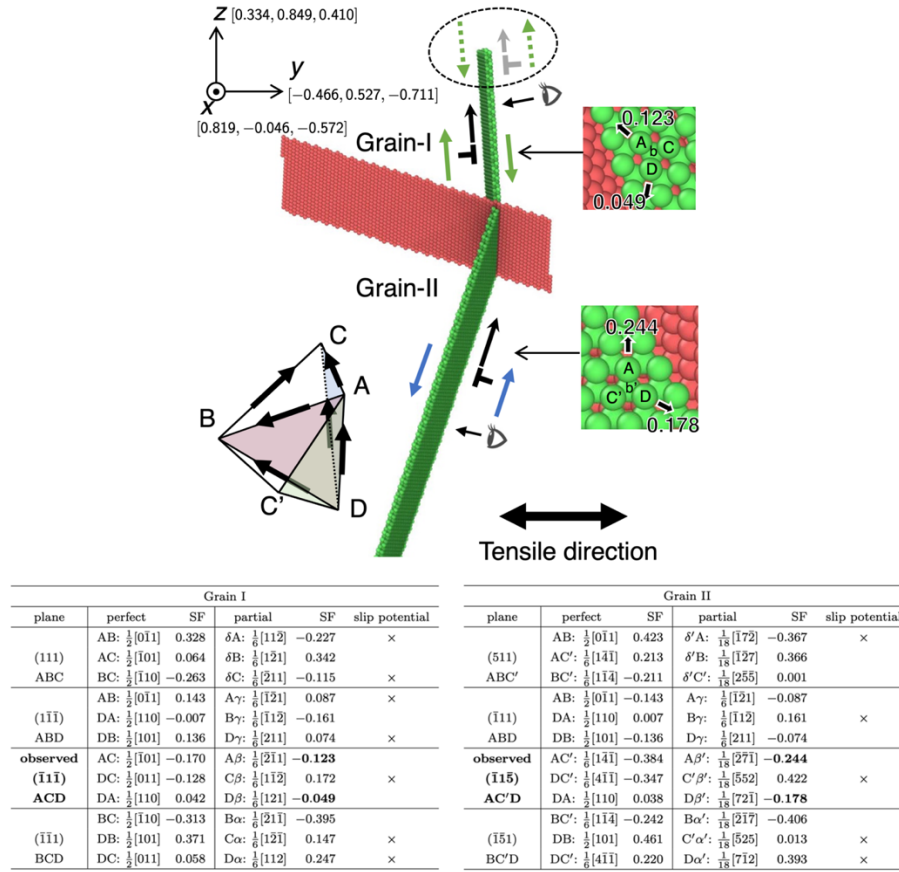


Fig. S3 An atomic structure model built to reproduce the geometrical relationship between Grains-I and -II in Fig. 4(a). The Schmid factor for each of possible slip systems are summarized in the attached tables. The notifications of AB and dA mean the slip direction from A to B and d to A, respectively, and the sign of Schmid factor corresponds to the defined slip direction. In the case of partial dislocation slips, only in either the positive or negative sliding direction can be activated due to the geometrical limitation of the crystal structure. The non-activated slip direction is checked in the column named slip potential. The Schmid factor for the observed stacking fault in the Grain-II is calculated to be 0.244 on plane AC'D. The Schmid factor for the observed stacking fault nucleated from the S3 boundary to the grain-I on plane ACD is relatively low, 0.12 and 0.049. The possible direction of the Burgers vector nucleated from the S3 boundary to the Grain-I under the uniaxial stress state is almost opposite direction of the Burgers vector approaching to the S3 boundary in the Grain-II, indicating the stacking fault nucleation in Grain-I requires the additional local stress concentration, which can realize the nucleation of a reasonable partial dislocation, as shown in a gray colored dislocation in the broken circle, which does not leave the large residual Burgers vector at the S3 boundary.

Video S1: <https://www.nature.com/articles/s41598-021-87811-w#Sec8>

Video S2: <https://www.nature.com/articles/s41598-021-87811-w#Sec8>

References

1. De Cooman, B. C., Kwon, O. & Chin, K. G. State-of-the-knowledge on TWIP steel. *Mater. Sci. Technol.* **28**, 513–527 (2012).
2. Grässel, O., Krüger, L., Frommeyer, G. & Meyer, L. W. High strength Fe-Mn-(Al, Si) TRIP/TWIP steels development - properties - application. *Int. J. Plast.* **16**, 1391–1409 (2000).
3. Bouaziz, O., Allain, S., Scott, C. P., Cugy, P. & Barbier, D. High manganese austenitic twinning induced plasticity steels: A review of the microstructure properties relationships. *Curr. Opin. Solid State Mater. Sci.* **15**, 141–168 (2011).
4. Neu, R. W. Performance and characterization of TWIP steels for automotive applications. *Mater. Perform. Charact.* **2**, 244–284 (2013).
5. De Cooman, B. C., Estrin, Y. & Kim, S. K. Twinning-induced plasticity (TWIP) steels. *Acta Mater.* **142**, 283–362 (2018).
6. Kim, S.-D. *et al.* Direct observation of dislocation plasticity in high-Mn lightweight steel by in-situ TEM. *Sci. Rep.* **9**, 15171 (2019).
7. Kim, J. K., Kwon, M. H. & De Cooman, B. C. On the deformation twinning mechanisms in twinning-induced plasticity steel. *Acta Mater.* **141**, 444–455 (2017).
8. Kwon, K. H. *et al.* Deformation behavior of duplex austenite and ϵ -martensite high-Mn steel. *Sci. Technol. Adv. Mater.* **14**, 014204 (2013).
9. Li, X., Chen, L., Zhao, Y., Yuan, X. & Kumar Misra, R. D. Influence of original austenite grain size on tensile properties of a high-manganese transformation-induced plasticity (TRIP) steel. *Mater. Sci. Eng. A* **715**, 257–265 (2018).
10. Kang, S., Jung, J.-G., Kang, M., Woo, W. & Lee, Y.-K. The effects of grain size on

- yielding, strain hardening, and mechanical twinning in Fe–18Mn–0.6C–1.5Al twinning-induced plasticity steel. *Mater. Sci. Eng. A* **652**, 212–220 (2016).
11. Gutierrez-Urrutia, I. & Raabe, D. Grain size effect on strain hardening in twinning-induced plasticity steels. *Scr. Mater.* **66**, 992–996 (2012).
 12. Ueji, R. *et al.* Tensile properties and twinning behavior of high manganese austenitic steel with fine-grained structure. *Scr. Mater.* **59**, 963–966 (2008).
 13. Mecking, H. & Kocks, U. F. Kinetics of flow and strain-hardening. *Acta Metall.* **29**, 1865–1875 (1981).
 14. Estrin, Y., Tóth, L. S., Molinari, A. & Bréchet, Y. A dislocation-based model for all hardening stages in large strain deformation. *Acta Mater.* **46**, 5509–5522 (1998).
 15. Venables, J. A. On dislocation pole models for twinning. *Philos. Mag.* **30**, 1165–1169 (1974).
 16. Fujita, H. & Mori, T. A formation mechanism of mechanical twins in F.C.C. Metals. *Scr. Metall.* **9**, 631–636 (1975).
 17. Cohen, J. B. & Weertman, J. A dislocation model for twinning in f.c.c. metals. *Acta Metall.* **11**, 996–998 (1963).
 18. S. Miura, J. Takamura & N. Narita. Orientation dependence of the flow stress for twinning in silver crystals. *Trans. JIM* **9**, 555 (1968).
 19. Mahajan, S. & Chin, G. Y. Comments on deformation twinning in silver- and copper-alloy crystals. *Scr. Metall.* **9**, 815–817 (1975).
 20. Shterner, V., Timokhina, I. B., Rollett, A. D. & Beladi, H. The Role of Grain Orientation and Grain Boundary Characteristics in the Mechanical Twinning Formation in a High Manganese Twinning-Induced Plasticity Steel. *Metall. Mater.*

- Trans. A* **49**, 2597–2611 (2018).
21. Hong, J., Kang, S., Jung, J. & Lee, Y. The mechanism of mechanical twinning near grain boundaries in twinning-induced plasticity steel. *Scr. Mater.* **174**, 62–67 (2020).
 22. Shimokawa, T. & Tsuboi, M. Atomic-scale intergranular crack-tip plasticity in tilt grain boundaries acting as an effective dislocation source. *Acta Mater.* **87**, 233–247 (2015).
 23. Shimokawa, T., Tanaka, M., Kinoshita, K. & Higashida, K. Roles of grain boundaries in improving fracture toughness of ultrafine-grained metals. *Phys. Rev. B* **83**, 214113 (2011).
 24. Mishin, Y., Asta, M. & Li, J. Atomistic modeling of interfaces and their impact on microstructure and properties. *Acta Mater.* **58**, 1117–1151 (2010).
 25. Tschopp, M. A. & McDowell, D. L. Dislocation nucleation in $\Sigma 3$ asymmetric tilt grain boundaries. *Int. J. Plast.* **24**, 191–217 (2008).
 26. Spearot, D., Jacob, K. & McDowell, D. Dislocation nucleation from bicrystal interfaces with dissociated structure. *Int. J. Plast.* **23**, 143–160 (2007).
 27. Tschopp, M. A., Tucker, G. J. & McDowell, D. L. Structure and free volume of $\langle 110 \rangle$ symmetric tilt grain boundaries with the E structural unit. *Acta Mater.* **55**, 3959–3969 (2007).
 28. Spearot, D. E., Jacob, K. I. & McDowell, D. L. Nucleation of dislocations from [001] bicrystal interfaces in aluminum. *Acta Mater.* **53**, 3579–3589 (2005).
 29. Schuh, C. A., Kumar, M. & King, W. E. Analysis of grain boundary networks and their evolution during grain boundary engineering. *Acta Mater.* **51**, 687–700 (2003).
 30. Randle, V. *The role of coincidence site lattice in grain boundary engineering*. Maney

Publishing (1996).

31. Jung, J. *et al.* Continuum understanding of twin formation near grain boundaries of FCC metals with low stacking fault energy. *npj Comput. Mater.* **3**, 21 (2017).
32. Grimmer, H., Bollmann, W. & Warrington, D. H. Coincidence-site lattices and complete pattern-shift in cubic crystals. *Acta Crystallogr. Sect. A* **30**, 197–207 (1974).
33. Lee, T. C., Robertson, I. M. & Birnbaum, H. K. TEM in situ deformation study of the interaction of lattice dislocations with grain boundaries in metals. *Philos. Mag. A* **62**, 131–153 (1990).
34. Zhu, T. & Gao, H. Plastic deformation mechanism in nanotwinned metals: An insight from molecular dynamics and mechanistic modeling. *Scr. Mater.* **66**, 843–848 (2012).
35. Jin, Z. H. *et al.* Interactions between non-screw lattice dislocations and coherent twin boundaries in face-centered cubic metals. *Acta Mater.* **56**, 1126–1135 (2008).
36. Mahato, B. *et al.* An effective stacking fault energy viewpoint on the formation of extended defects and their contribution to strain hardening in a Fe-Mn-Si-Al twinning-induced plasticity steel. *Acta Mater.* **86**, 69–79 (2015).
37. Idrissi, H., Renard, K., Schryvers, D. & Jacques, P. J. TEM investigation of the formation mechanism of deformation twins in Fe–Mn–Si–Al TWIP steels. *Philos. Mag.* **93**, 4378–4391 (2013).
38. Williams, D. B. & Carter, C. B. *Transmission Electron Microscopy. Transmission Electron Microscopy: A Textbook for Materials Science* (Springer US, 2009).
doi:10.1007/978-0-387-76501-3.
39. Shimokawa, T. Asymmetric ability of grain boundaries to generate dislocations under tensile or compressive loadings. *Phys. Rev. B* **82**, 174122 (2010).

40. Sangid, M. D., Ezaz, T., Sehitoglu, H. & Robertson, I. M. Energy of slip transmission and nucleation at grain boundaries. *Acta Mater.* **59**, 283–296 (2011).
41. Rémy, L. Twin-slip interaction in f.c.c. crystals. *Acta Metall.* **25**, 711–714 (1977).
42. Hirth, J. P. The influence of grain boundaries on mechanical properties. *Metall. Trans.* **3**, 3047–3067 (1972).
43. Wang, J., Beyerlein, I. J. & Tomé, C. N. Reactions of lattice dislocations with grain boundaries in Mg: Implications on the micro scale from atomic-scale calculations. *Int. J. Plast.* **56**, 156–172 (2014).
44. Zhu, Y. T. *et al.* Dislocation–twin interactions in nanocrystalline fcc metals. *Acta Mater.* **59**, 812–821 (2011).
45. Beladi, H., Nuhfer, N. T. & Rohrer, G. S. The five-parameter grain boundary character and energy distributions of a fully austenitic high-manganese steel using three dimensional data. *Acta Mater.* **70**, 281–289 (2014).
46. Zhang, L., Lu, C. & Tieu, K. A review on atomistic simulation of grain boundary behaviors in face-centered cubic metals. *Comput. Mater. Sci.* **118**, 180–191 (2016).
47. Ratanaphan, S. *et al.* Atomistic simulations of grain boundary energies in austenitic steel. *J. Mater. Sci.* **54**, 5570–5583 (2019).
48. Rittner, J. D. & Seidman, D. N. $\langle 110 \rangle$ symmetric tilt grain-boundary structures in fcc metals with low stacking-fault energies. *Phys. Rev. B* **54**, 6999–7015 (1996).
49. Sangid, M. D., Sehitoglu, H., Maier, H. J. & Niendorf, T. Grain boundary characterization and energetics of superalloys. *Mater. Sci. Eng. A* **527**, 7115–7125 (2010).
50. Clark, W. A. T. *et al.* On the criteria for slip transmission across interfaces in

- polycrystals. *Scr. Metall. Mater.* **26**, 203–206 (1992).
51. Kacher, J. & Robertson, I. M. Quasi-four-dimensional analysis of dislocation interactions with grain boundaries in 304 stainless steel. *Acta Mater.* **60**, 6657–6672 (2012).
 52. Bachurin, D. V., Weygand, D. & Gumbsch, P. Dislocation–grain boundary interaction in $\langle 111 \rangle$ textured thin metal films. *Acta Mater.* **58**, 5232–5241 (2010).
 53. Tadmor, E. B. & Hai, S. A Peierls criterion for the onset of deformation twinning at a crack tip. *J. Mech. Phys. Solids* **51**, 765–793 (2003).
 54. Wang, L. *et al.* New twinning route in face-centered cubic nanocrystalline metals. *Nat. Commun.* **8**, 2142 (2017).
 55. Jin, Z. H., Dunham, S. T., Gleiter, H., Hahn, H. & Gumbsch, P. A universal scaling of planar fault energy barriers in face-centered cubic metals. *Scr. Mater.* **64**, 605–608 (2011).
 56. Bishop, G. H. & Chalmers, B. A coincidence — Ledge — Dislocation description of grain boundaries. *Scr. Metall.* **2**, 133–139 (1968).
 57. Wang, G. J., Sutton, A. P. & Vitek, V. A computer simulation study of $\langle 001 \rangle$ and $\langle 111 \rangle$ tilt boundaries: the multiplicity of structures. *Acta Metall.* **32**, 1093–1104 (1984).
 58. Sutton, A. P. & Vitek, V. On the Structure of Tilt Grain Boundaries in Cubic Metals II. Asymmetrical Tilt Boundaries. *Philos. Trans. R. Soc. A Math. Phys. Eng. Sci.* **309**, 37–54 (1983).
 59. Sato, K. *et al.* Development of a novel straining holder for transmission electron microscopy compatible with single tilt-axis electron tomography. *Microscopy* **64**,

369–375 (2015).

Chapter 5

The role of $\Sigma 3\{111\}$ twin boundary during deformation twin nucleation process in an ultrafine-grained high-manganese austenitic steel

Chang-Yu Hung^{a,*}, Tomotsugu Shimokawa^b, Yu Bai^c, Nobuhiro Tsuji^{c,d},
Mitsuhiro Murayama^{a,c*}

^a Department of Materials Science and Engineering, Virginia Tech, Blacksburg, VA 24061, USA

^b Faculty of Mechanical Engineering, Kanazawa University, Kanazawa, Ishikawa, 920-1192, Japan

^c Department of Materials Science and Engineering, Kyoto University, Yoshidahonmachi, Sakyo-ku, Kyoto 606-8501, Japan

^d Elements Strategy Initiative for Structural Materials, Kyoto University, Yoshidahonmachi, Sakyo-ku, Kyoto 606-8501, Japan

^e Institute for Materials Chemistry and Engineering, Kyushu University, Kasuga, Fukuoka 816-8580, Japan

*Corresponding authors

Chang-Yu Hung (changyul@vt.edu) TEL: 540-231-0466, FAX 540-231-1963

Mitsuhiro Murayama (murayama@vt.edu) TEL: 540-231-9470, FAX 540-231-1963

Contact information of authors

Chang-Yu Hung E-mail: changyul@vt.edu

Tomotsugu Shimokawa E-mail: simokawa@se.kanazawa-u.ac.jp

Yu Bai, E-mail: bai.yu.6m@kyoto-u.ac.jp

Nobuhiro Tsuji E-mail: nobuhiro-tsuji@mtl.kyoto-u.ac.jp

Mitsuhiro Murayama E-mail: murayama@vt.edu

This chapter has been submitted for reviewed in Journal of Materials Science and Technology

Abstract

Ultrafine-grained (UFG) twinning-induced plasticity (TWIP) steels have been found to overcome the paradox of strength and ductility in metals benefiting likely from its unique interplay between conventional dislocation slip and deformation twinning behavior. Here, this study provides insights into the atomistic process of deformation twin nucleation at $\Sigma\{111\}$ twin boundaries, the dominant type of grain boundary in the UFG-TWIP steel of interest. In response to the applied tensile stresses, the structure of coherent $\Sigma\{111\}$ twin boundary changes from atomistically smooth to partly defective by a disconnection-mediated twin boundary migration mechanism. High resolution transmission electron microscopy (HRTEM) demonstrates that the formation of disconnection on coherent $\Sigma\{111\}$ twin boundaries is associated with the motion of Shockley partial dislocations on the boundaries. This disconnection-mediated twin boundary migration in UFG TWIP steel appears to be characteristically different from the coarse-grained counterpart where the localized stress concentration is induced by in-grain dislocations - $\Sigma\{111\}$ boundary interaction. On the other hand, in-situ TEM deformation experiments reveals the layer-by-layer emission of stacking faults is the deformation twin nucleation mechanism in the UFG TWIP steel, which is common with the coarse-grained counterpart.

Keywords: Ultrafine-grained materials, Deformation twinning, Grain boundary migration, In situ transmission electron microscopy (TEM), Strain mapping

5.1 Introduction

Nanocrystalline metals have attracted intensive research interest because of their potential to achieve extraordinary properties compared with conventional coarse-grained counterparts. This has led to a series of research regarding the synthesis, processing, characterization, and potential applications of nanocrystalline metals in the past few decades [1–5]. Nanocrystalline metals commonly exhibit a high strength/hardness that is generally accompanied by poor ductility, known as the strength-ductility paradox, regardless of their crystal structure seen in ultrafine-grained (UFG) aluminum [6], UFG interstitial free steel [7], and nanograined copper alloys [8]. The yield strength of materials increases monotonously with decreasing in the grain size, which can be understood in terms of Hall-Petch relationship [9,10]. On the other hand, the tensile ductility drops immediately when the average grain size becomes smaller than 1 μm because fine grains leave very little spaces for dislocation dynamics leading to a less enhanced strain-hardening rate and resulting in the plastic instability during deformation [11,12]. This strength-ductility trade-off relationship generally appears in most of nanocrystalline or UFG metals.

Recently, a combination of high strength and moderate ductility was simultaneously archived in UFG Mg alloy [13], UFG Fe-24Ni-0.3C metastable austenitic steel [14], and UFG high manganese Twinning Induced Plasticity (TWIP) steels [15–17]. Experimental results of the above examples indicate a possibility to overcome the strength-ductility trade-off relationship, and demonstrate the unexpected activation of deformation mode in addition to normal dislocation slip, for example, $\langle c+a \rangle$ dislocation activation in the UFG Mg alloy, deformation twinning in the UFG TWIP steels, and martensitic transformation in the UFG metastable austenitic steel. Tsuji et al. [14] suggest that the sequential activation of different

deformation modes would foster the regeneration of strain-hardening ability during plastic deformation and leading to a high strength and large ductility due to the possible interactions between different deformation modes. The mechanisms to activate such unusual deformation modes are still not fully understood, however, our previous study related to the grain size altering yielding mechanism in a UFG TWIP steel [15] suggests that the activation of different deformation modes takes place in the very early stage of plastic deformation, i.e., around the macroscopic yield point, due to the lack of initial mobile dislocations and inactive in-grain dislocation sources, both are characteristic in UFG grains. Deformation twinning was initiated at the grain boundaries and developed in the under-1 μm grains, while the normal in-grain slip was mostly observed in the over-1 μm grains.

Although the enhancement of strength and ductility by deformation twinning has been extensively described in conventional coarse-grained TWIP steels [18–20], we are not yet able to control the TWIP event in UFG metals because the detailed atomistic processes of deformation twinning at grain boundaries have not been well explored. The conventional deformation twinning mechanisms based on the arrangement of highly coordinated Shockley partial dislocations on $\{111\}$ slip planes [21–25] appear to be insufficient to explain the grain boundary mediated deformation twinning in UFG TWIP steels. We hypothesize that the deformation twinning in UFG TWIP steels is highly correlate with grain boundary structure and misorientation for the following reasons.

Only handful studies have focused on the correlation between grain boundary character and deformation twin mechanism in the conventional coarse-grained TWIP steels [26,27]. We [27] recently experimentally revealed that deformation twin nucleation at a $\Sigma 3\{111\}$ boundary occurs only when a localized stress concentration field formed by

dislocation pile-up at the annealing twin ($\Sigma\{111\}$) boundary, while no obvious localized stress concentration is required at relatively high-energy grain boundaries such as $\Sigma 21$ or $\Sigma 31$. It can be expected that nucleating deformation twin at high-energy grain boundaries in UFG TWIP steels could be spontaneous, similar to the cases in coarse-grained counterpart. On the other hand, the required localized stress concentration by dislocation pile-ups for deformation twin nucleation at $\Sigma\{111\}$ boundary is unlikely achievable in UFG microstructure, which leave an open question, i.e., why the UFG TWIP steel can overcome strength-ductility trade-off relationship if its dominant boundary ($\Sigma\{111\}$) does not play a key role in deformation twinning. In other words, what the atomistic details of deformation twin nucleation mechanism is if $\Sigma\{111\}$ boundaries actually act as deformation twin nucleation sites.

In this study, we aim to understand the microstructural response of $\Sigma\{111\}$ twin boundary to plastic deformation and its role during the deformation twinning process. A UFG Fe-31Mn-3Al-3Si (wt.%) high-manganese TWIP steel (SFE = 40 mJ·m⁻²) with average grain size = 0.79 μm was fabricated. The detailed deformed microstructure near $\Sigma\{111\}$ twin boundaries and their local strain level were investigated using transmission electron microscopy and microprobe scanning transmission microscopy, respectively.

5.2 Experimental procedure

5.2.1 Sample fabrication

A UFG TWIP steel having the average grain size, $0.79 \pm 0.39 \mu\text{m}$, were fabricated for this study. The chemical composition of the steel was Fe-31Mn-3Al-3Si wt.%. The as-received TWIP steel was cold rolled from 12 mm to 1 mm (92% reduction) by multi-pass cold rolling and then heat treated in a salt bath at 950°C for 5 minutes followed by water

quenching.

5.2.2 Uniaxial tensile test

The sheet-type tensile test pieces with a specific dimension, 13×2 mm rectangular plate, were sliced and mechanically thinned to approximately $150 \mu\text{m}$ thick for deformed microstructure characterization by electron backscatter diffraction (EBSD) and transmission electron microscopy (TEM) techniques. The $150 \mu\text{m}$ thick sheets were tensile-deformed to 0.046 and 0.062 engineering strain using a testing machine (Kammrath and Weiss Module 200 N) at a strain rate of $4.6 \times 10^{-4} \text{ s}^{-1}$ at room temperature.

5.2.3 Electron backscattered diffraction characterization

After uniaxial tensile test, specimens for EBSD analysis were mechanically polished by abrasive paper up to 2000 grits then electro-polished. The microstructural features including grain boundary maps and local strain distribution were examined using a TSL OIM EBSD system attached to a FEI Helios 600 dual-beam field emission gun (FEG) scanning electron microscope (SEM) / focused ion beam (FIB) system. The EBSD maps were acquired at 30 kV acceleration voltage and 13 mm working distance. The scanning step size was 50 nm. No data clean-up was performed except for the removal of some points with low confidence value.

The local strain distribution was evaluated from the kernel average misorientation (KAM). KAM is a local misorientation defined as the average misorientation of a point with its nearest neighbors in a grain. The average misorientation of a given point is calculated by taking that point as well as all of its nearest neighbors into account with a criterion that the misorientation exceeding threshold 3° will be discarded from the calculation, because these points are considered to belong to the adjacent grains.

5.2.4 Transmission electron microscopy characterization

Samples prepared for TEM analyses were cut from the center of the deformed samples, 2×2 mm square-shape foil, and then mechanically thinned to 70 μm thick. Thinning to electron transparency was achieved by using a twin-jet electropolisher (Fischione Model 110) with a 95% acetic acid - 5% perchloric acid electrolyte maintained at 17°C and the applied voltage of 38 V. The TEM characterization was performed using a JEOL JEM 2100 operated at 200 kV with Gatan Orius 200D and Ultrascan 1000XP cameras.

5.2.5 In-situ deformation TEM

The specimens for in-situ deformation tests were sliced 2×2 mm, identical to the one used for TEM analysis. The square-shape specimen was fixed on a cartridge-type blade for SATO Holder Duo (Mel-Build Co.) [28]. The strain rate was controlled at approximately $6.7 \times 10^{-5} \text{ s}^{-1}$ in this study. All videos were recorded in the bright field (BF) mode and a FEI Titan 80-300 S/TEM operated at 300kV was used. Gatan Orius SC200D camera and Digital Micrograph with the high-resolution streaming video plug-in were used for video recording.

5.2.6 Strain mapping using microprobe STEM

The FEI Titan 80-300V S/TEM also was used in this analysis. Strain mapping was performed using the parallel probe scanning transmission electron microscope (referred to microprobe-STEM) mode. The microprobe-STEM employed a 10 μm second condenser aperture to reduce the beam semi-convergence angle to be 0.13 mrad and the beam diameter to be less than 2 nm.

5.3 Results

The fully recrystallized and tensile-strained microstructure of the UFG TWIP steel were characterized by EBSD. Two grain boundary maps for fully recrystallized and tensile-

strained samples are shown in **Fig. 5.1(a)** and **Fig. 5.1(b, c)**, respectively. Black lines represent the high-angle grain boundaries with rotation angle θ , $15^\circ \leq \theta < 60^\circ$, and red lines represent annealing twin boundaries, known as $\Sigma 3\{111\}$ boundaries. **Fig. 5.1(a)** demonstrates that the microstructure prior to tensile straining were composed of fully recrystallized single austenite phase.

Kernel average misorientation (KAM) maps for fully recrystallized and tensile-strained samples (0.046 and 0.062) are shown in **Fig. 5.1(d - f)**. KAM analysis provides a qualitative analysis of the local misorientation that is strongly influenced by the density of geometrically necessary dislocations (GNDs) [29]. The fully recrystallized sample in **Fig. 5.1(d)** shows very little local misorientation over the entire scanned area containing both in the grain interior and the regions near grain boundaries, suggesting that only uninfluential amounts of deformations were introduced during the EBSD sample preparation. When the samples were tensile strained to the engineering strain of 0.046 and 0.062, the local misorientation were observed mainly around grain boundaries as indicated by white arrows in the **Fig. 5.1(e)** and (f). Since the local misorientation is a function of the GND density, the uneven distribution suggests that the heterogeneous dislocation dynamics at individual grain boundaries somehow triggered then proceeded by the applied stress. Although the level of plastic strain accumulated near grain boundaries cannot be quantified, the level of the plastic strain accumulation appears to be correlated with the grain boundary misorientation. For example, in the **Fig. 5.1(c, f)**, the GND density near coherent $\Sigma 3\{111\}$ boundaries (marked by green arrows and circles) are clearly less pronounced than those in other general high-angle grain boundaries. This result could be explained by considering the structure of the low energy $\Sigma 3\{111\}$ boundary, such that the coherent atomic structure of

$\Sigma 3\{111\}$ boundary is generally believed to be stable and not acts as a proactive dislocation source especially in the early stage of plastic deformation. Whether the twin boundaries were deformed or not cannot be immediately confirmed in here solely based on the EBSD with the scan step size of 50 nm. Therefore, further microstructure observations in $\Sigma 3\{111\}$ boundaries were conducted to have a better insight of local microstructure, and their microstructure would be compared with those in general high-angle boundaries.

In **Fig. 5.2**, the sample deformed to the engineering strain of 0.062 was characterized by TEM with a particular focus on the deformed regions near grain boundaries. Two general high-angle grain boundaries where the adjoining lattice is tilted by 47.5° along $[1\ 4\ 10]$ axis and a $[011]$ $\Sigma 9$ tilt boundary were shown in **Fig. 5.2(a)** and (b), respectively. As a molecular

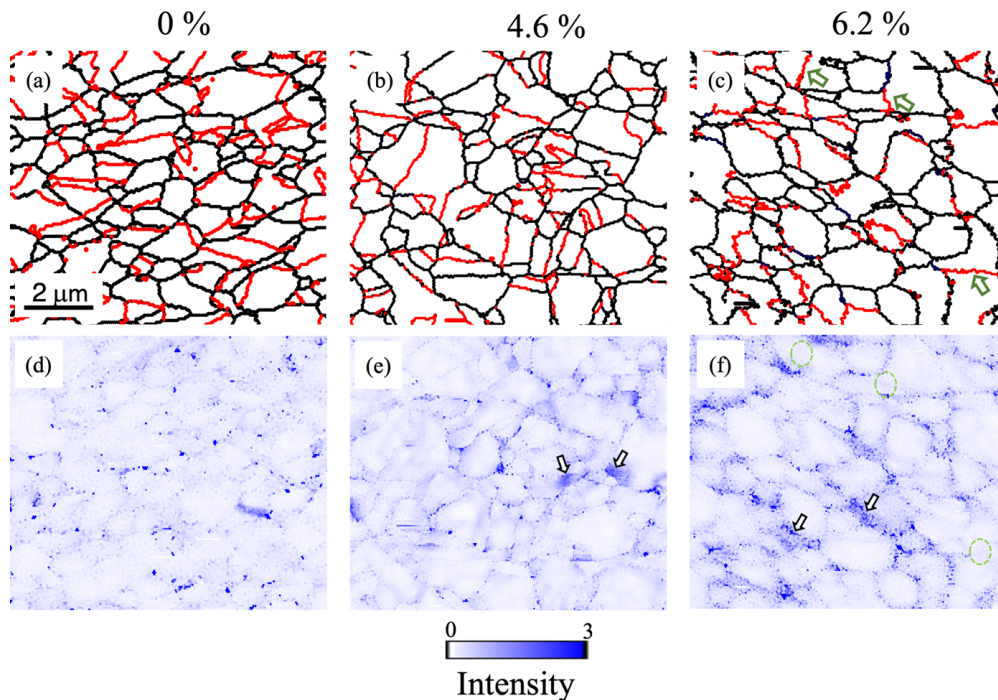


Figure 5.1 EBSD maps of fully recrystallized (0%) and tensile strained (4.6% and 6.2%) UFG samples with the scan step size of 50 nm: (a-c) grain boundary maps, (d-f) kernel average misorientation maps. Black lines in (a-c) represent the high angle boundaries with rotation angle (θ), $15^\circ \leq \theta < 60^\circ$, and red lines represent $\Sigma 3$ boundaries. The average misorientation showing in (d-f) is calculated by taking the points as well as all of its nearest neighbors into account with a criterion that the misorientation exceeding threshold 3° will be discarded from the calculation. The stress concentration and several representative twin boundaries are indicated by white arrows and green arrows, respectively

dynamics simulation reveals that the latter boundary has a great potential to emit partial dislocations [30], both boundaries were found to act as a nucleation site for deformation twin. The dark contrast indicated by the white arrows appears to be induced by a dislocation reaction within the grain boundary, i.e., a deformation twinning event associated with a grain-boundary dislocation dissociation. In **Fig. 5.2(c - e)**, three twin lamellas having different sizes in the range of 100 to 500 nm were observed, demonstrating that the $\Sigma 3\{111\}$ boundaries were also acting as nucleation sites for deformation twins without the presence of dislocation pile-ups, which are similar to the other general grain boundaries observed in **Fig. 5.2(a-b)**. Strain contrast that uniformly spreads along the twin boundaries was observed regardless of the width of twin. This characteristic localized strain contrast within $\Sigma 3\{111\}$ boundaries as well as deformation twin observed near / at twin boundaries shown in TEM images was not identified by the EBSD analysis possibly because of the limitation of EBSD's spatial resolution, i.e., the size of deformation twins (~ 3 nm) and the extremely localized strain within $\Sigma 3\{111\}$ boundary are too small to be identified.

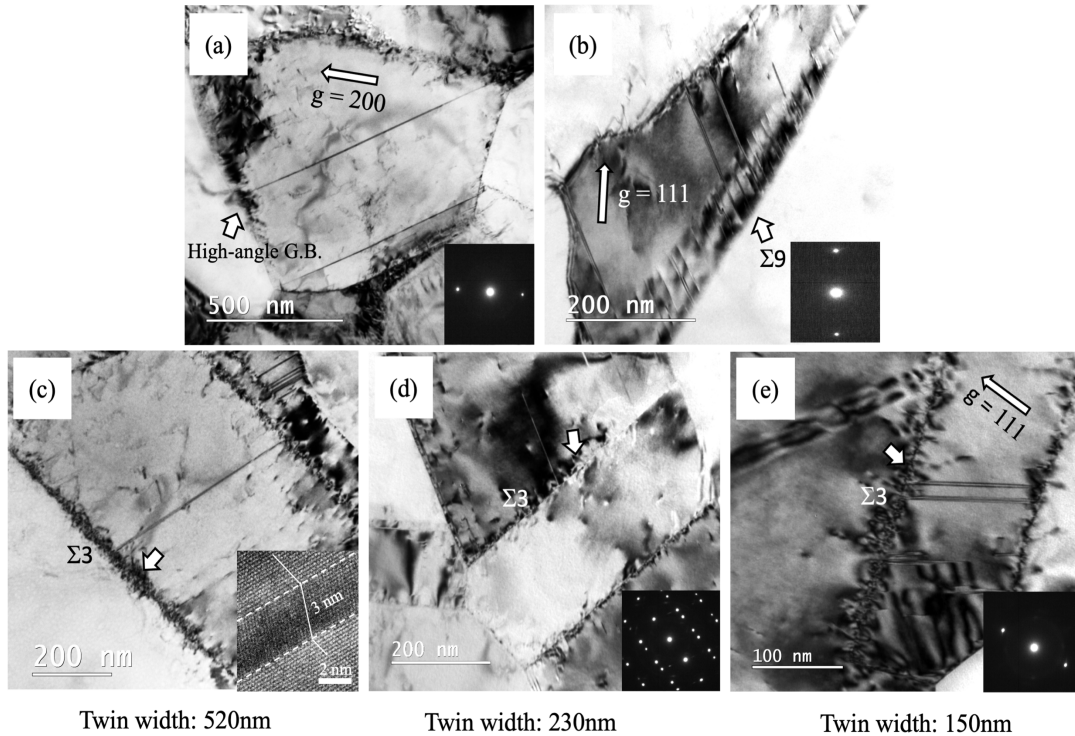


Figure 5.2 BF images show the formation of deformation twins in a UFG TWIP steel sample deformed to the engineering strain = 0.062. (a) a deformation twin is nucleated from a general high-angle grain boundary, taken in a two-beam condition with an operative reflection = g_{200} . The dark strain contrast along the grain boundary is indicated by a white arrow. (b) a $[011] \Sigma_9$ tilt boundary decorated with a group of grain-boundary dislocations is indicated by a white arrow, where deformation twins are nucleated. The BF image were taken in a two-beam condition with an operative reflection = g_{111} . (c-e) three $\Sigma_3\{111\}$ twin boundaries (Σ_3) having different twin width (520 nm, 230 nm, and 150 nm) are acting as the nucleation sites for deformation twinning. The localized strain concentration with dark contrast is uniformly spread along the $\Sigma_3\{111\}$ twin boundaries.

Fig. 5.3(a - d) are selected frames extracted from an in-situ TEM tensile deformation test movie in provided supplementary video. Several stacking faults nucleated at two $\Sigma_3\{111\}$ boundaries and a group of the dislocations are indicated by the arrows filled with dots and the black arrow, respectively. In the initial stage of plastic deformation, the nucleation of stacking faults from both sides of the $\Sigma_3\{111\}$ boundary and the glide of a group of dislocations took place simultaneously as seen in **Fig. 5.3(a)** and (b). The stacking faults were observed to be emitted from the boundary ahead of a group of dislocation (black arrow) piling up, suggesting that the dislocation pile-up was not responsible to the localized

stress concentration field for twin nucleation. Soon after that, the zero contrast of stacking fault was recorded in the **Fig. 5.3(c)**, which could be ascribed by the emission of the third overlapping stacking fault that made the contrast of the stacking fault nearly vanished, i.e., phase angle α becomes 2π as equivalent as the perfect lattice [31]. As the leading Shockley partial dislocation was continuously emitted from the $\Sigma 3\{111\}$ boundary (**Fig. 5.3(d)**), the outer fringe contrast of the fault 2 (F_2) turned from dark to bright, i.e., two stacking faults (F_1 and F_2) were overlapping and showed the reversal fringe contrast. These successive emission events occur rapidly and the precursor of deformation twin, overlapping stacking faults, are formed as a result. The BF image in **Fig. 5.3(d)** illustrates two $\Sigma 3\{111\}$ twin boundaries decorated by localized strain contrast and two stacking faults; both are inclined from the parallel incident electron beam direction. A Thompson tetrahedron inserted in **Fig. 5.3(d)** provides the crystallographic relationship between the $\Sigma 3\{111\}$ twin boundary and the emitted stacking fault. Plane \overline{ACD} and plane \overline{ABC} represents the $\Sigma 3\{111\}$ twin boundary and the stacking fault plane, respectively. In the deformation process, Shockley partial dislocations having the Burgers vector of b_1 and b_2 will glide on the twin plane of

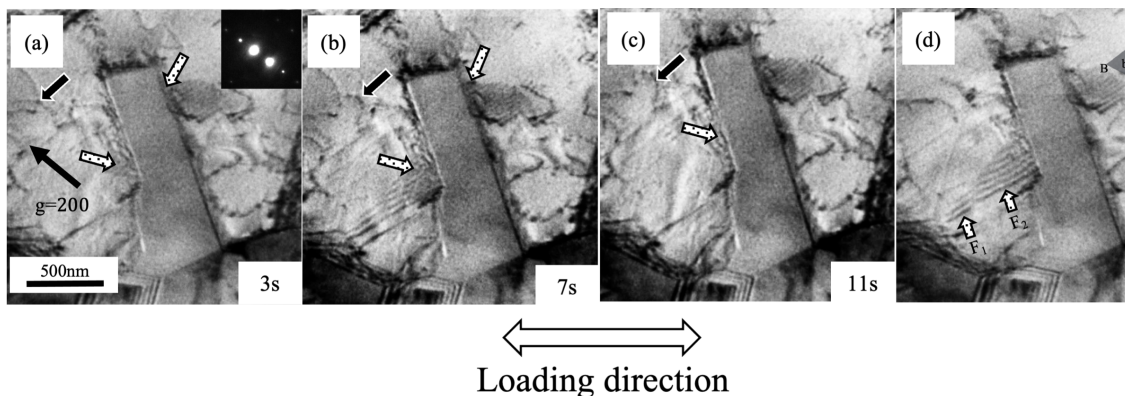


Figure 5.3 Selected frames of a TEM in-situ deformation test video data showing an area near the $\Sigma 3\{111\}$ twin boundary. The video (see provided supplementary video) was recorded in a two-beam condition with operative reflection = g_{200} . (a) the initial stage of the stacking fault emission event. The arrows filled with dots indicates the stacking faults nucleated from the boundaries. (b-d) the continuous emission of stacking faults from the $\Sigma 3\{111\}$ twin boundary. The periodic contrast change was observed during the deformation and may be the result of overlapping of stacking faults.

\overline{ACD} while Shockley partial dislocations having the Burgers vector of b_α and b_β on the plane of \overline{ABC} will be emitted to the grain.

An edge-on BF image in **Fig. 5.4(a)** illustrates a deformed $\Sigma 3\{111\}$ twin boundary and a thin deformation twin indicated by a black arrow. The $\Sigma 3\{111\}$ twin plane and the deformation twin plane were designated to be $(11\bar{1})$ and $(\bar{1}\bar{1}\bar{1})$, respectively, based on the selected area electron diffraction (SAED) pattern taken from a $[011]_{fcc}$ zone axis in the inset of **Fig. 5.4(a)**. The tensile axis (a double-white arrow) was determined to be approximately $[\bar{2} 5 \bar{5}]$ with respect to the crystal frame of matrix. Applying the Schmid's law to estimate the resolved shear stresses on slip planes, the $[\bar{2} 5 \bar{5}]_{matrix}$ tensile axis causes the resolved shear stress applied on $\{111\}\langle 112\rangle$ systems to be larger than that applied on $\{111\}\langle 110\rangle$ systems in both $\Sigma 3\{111\}$ twin plane and deformation twin plane. For example, the Schmid factor for $a/6[2\bar{1}1]$ Shockley partial dislocation gliding on $[11\bar{1}]$ planes is as high as 0.488 which would promote the Shockley partial dislocation to glide on the planes adjacent to the twin plane during plastic deformation. To probe detailed insights of how the $\Sigma 3\{111\}$ twin boundary being deformed and the origin of those localized contrasts near $\Sigma 3\{111\}$ twin boundaries, two regions squared in **Fig. 5.4(a)** along the twin boundary were examined by the high-resolution TEM (HRTEM) imaging technique. **Fig. 5.4(b, c)** are the corresponding HRTEM images taken from a $[011]_{fcc}$ zone axis, showing (i) atomic structure of a kink-like step prior to deformation twin nucleation (**Fig. 5.4(b)**) and (ii) a deformation twin nucleated at a step having a several-monolayer height (**Fig. 5.4(c)**). A pair of experimental and Fourier-filtered HRTEM images in **Fig. 5.4(b)** exhibit two defective steps (A and B) having a two- and three- monolayer height, respectively, while **Fig. 5.4(c)** shows a deformation twin nucleated from a three-monolayer height step. The step consisted of Shockley partial

dislocations on the successive $(11\bar{1})$ planes causes the $\Sigma 3\{111\}$ twin boundary to migrate into the neighboring matrix-lamellae thus consequently thickening the original twin-lamellae. In **Fig. 5.4(c)**, the boundary steps resulted by the $\Sigma 3\{111\}$ twin boundary migration appears to act as a nucleation site for deformation twin. The characteristic strain contrast along $\Sigma 3\{111\}$ twin boundary observed in the BF TEM images appears to be originated from the dislocations gliding on the several $(11\bar{1})$ planes adjacent to the $\Sigma 3\{111\}$ twin plane.

The strain mapping by the microprobe scanning transmission electron microscopy (μ p-STEM) technique was performed on the regions in/near an $\Sigma 3\{111\}$ twin boundary in **Fig.5.5**. Three regions of interest are marked as Region- I, II, and III. A section of the $\Sigma 3\{111\}$ twin boundary and deformation twins were included in Region- I and II to compare with the Region-III where deformation twinning has not taken place. First, the $\Sigma 3\{111\}$ twin boundary was tilted to the edge-on condition, such that the incident electron beam direction was parallel to the grain boundary plane. A series of over 600 electron diffraction patterns

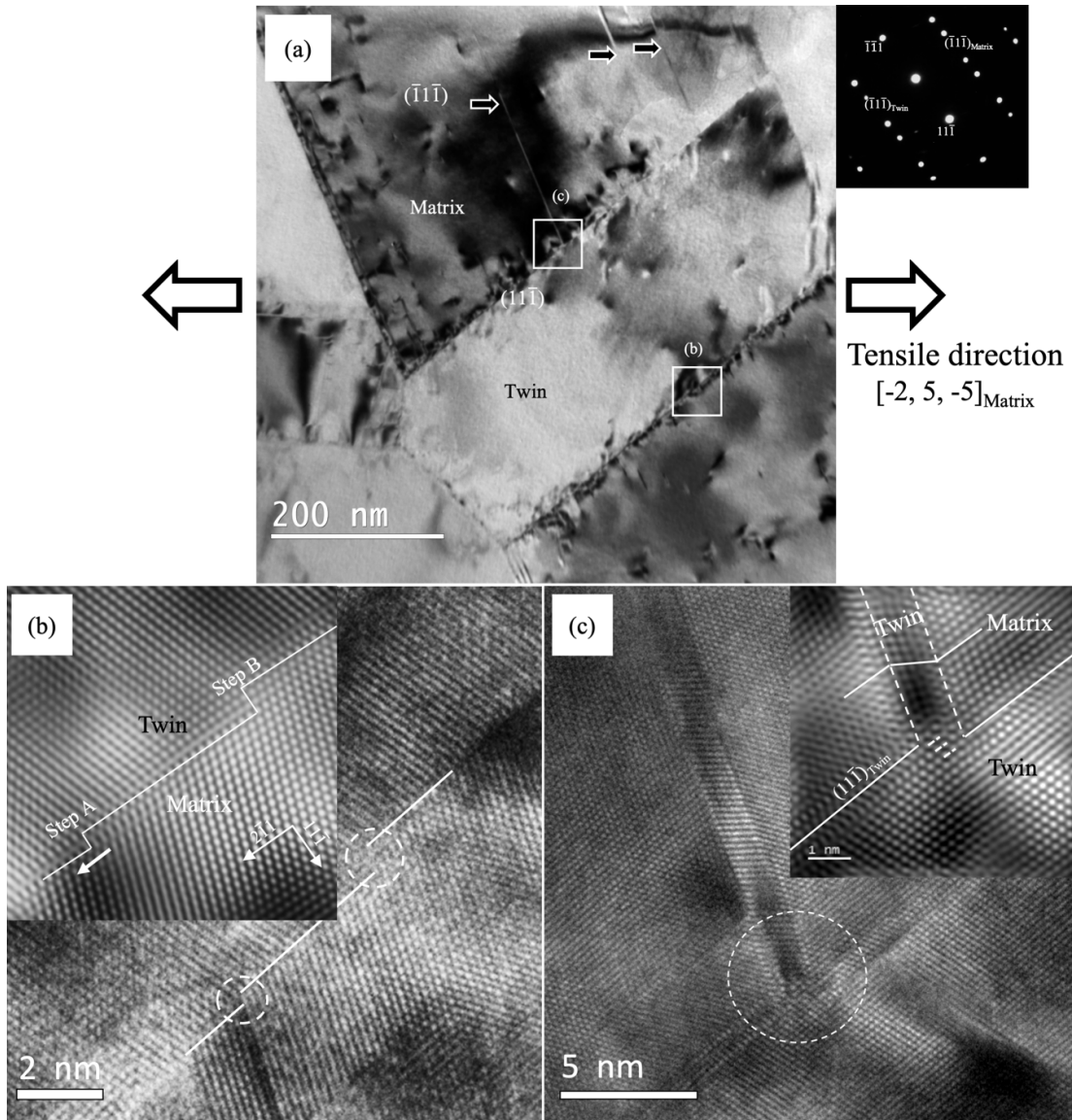


Figure 5.4 (a) BF image taken in a zone axis = $[011]$ shows the deformed microstructure and deformation twin at an $\Sigma 3\{111\}$ twin boundary. The $\Sigma 3\{111\}$ twin plane and deformation twin plane are designated to be $(11\bar{1})_{\text{matrix}}$ and $(\bar{1}\bar{1}\bar{1})_{\text{matrix}}$ based on the attached inset of diffraction pattern. The tensile direction indicated by double white arrow was estimated to be $[\bar{2} \ 5 \ \bar{5}]_{\text{matrix}}$. (b) HRTEM shows two kink-like steps that are circled by white-dotted line. The inset Fourier-filtered HRTEM corresponding to the white-dotted lines shows two Frank circuits (A and B) encircling Shockley partial dislocations and the steps. (c) HRTEM shows a deformation twin nucleated from a step having 3 monolayers in height at the $\Sigma 3\{111\}$ twin boundary. The inset Fourier-filtered HRTEM corresponding to the nucleation site circled by white-dotted line shows the detailed atomic structure.

were acquired from the 125×125 nm square in Region-I and 50×50 nm square in Region-II and III, with a distance of 5 nm and 2 nm between diffraction patterns, respectively. the diameter of STEM probe was less than 2 nm for this analysis. Secondly, to calculate the

strain from the diffraction patterns, a custom-made data processing software package combined with the NBD analysis software package (System In Frontier, Inc., Japan) was employed. The software determines the central point of recognizable diffraction spots in each of electron diffraction patterns, then computes the interplanar spacing, i.e., the distance between individual diffraction spot and the origin (the center spot). The relative strain along a crystallographic direction, for example, $[11\bar{1}]$, was determined based on the change of distance between the center spot and $11\bar{1}$ diffracted spots relative to that of the reference point. Finally a 2D strain map in a $[11\bar{1}]$ crystallographic orientation, i.e., in the direction of $\Sigma 3\{111\}$ twin boundary normal, was generated. The least strained position within each of regions (black cross marker in Region I, II, and III) was selected to be the reference point, thus the positive (tension) and negative (compression) strain were displayed relative to the reference point. **Fig. 5.5(b)** shows that a huge amount of tensile strain arose in a part of the $\Sigma 3\{111\}$ twin boundary, while the tensile strain below that area of the $\Sigma 3\{111\}$ twin boundary (white arrow) was much less pronounced. Similarly, another localized tensile strain on the $\Sigma 3\{111\}$ twin boundary was observed in **Fig. 5.5(c)** drastically decreased only a short distance apart. Based on these strain maps, the areas where the deformation twins nucleated have a relatively less pronounced strain field, suggesting that an energy relaxation mechanism associated with deformation twinning appears to take place within the $\Sigma 3\{111\}$ twin boundary, which reduce the stored strain. Region-III in **Fig. 5.5(d)** demonstrates a pronounced localized strain field (white arrows) at the $\Sigma 3\{111\}$ twin boundary. Based on the corresponding microstructure observed in **Fig. 5.4(b)**, the kink-like steps appear to be on the high strain site. We believe that the kink-like steps would become a nucleation site for deformation twin if the deformation could continuously proceed as localized stress

exceeding the twinning stress.

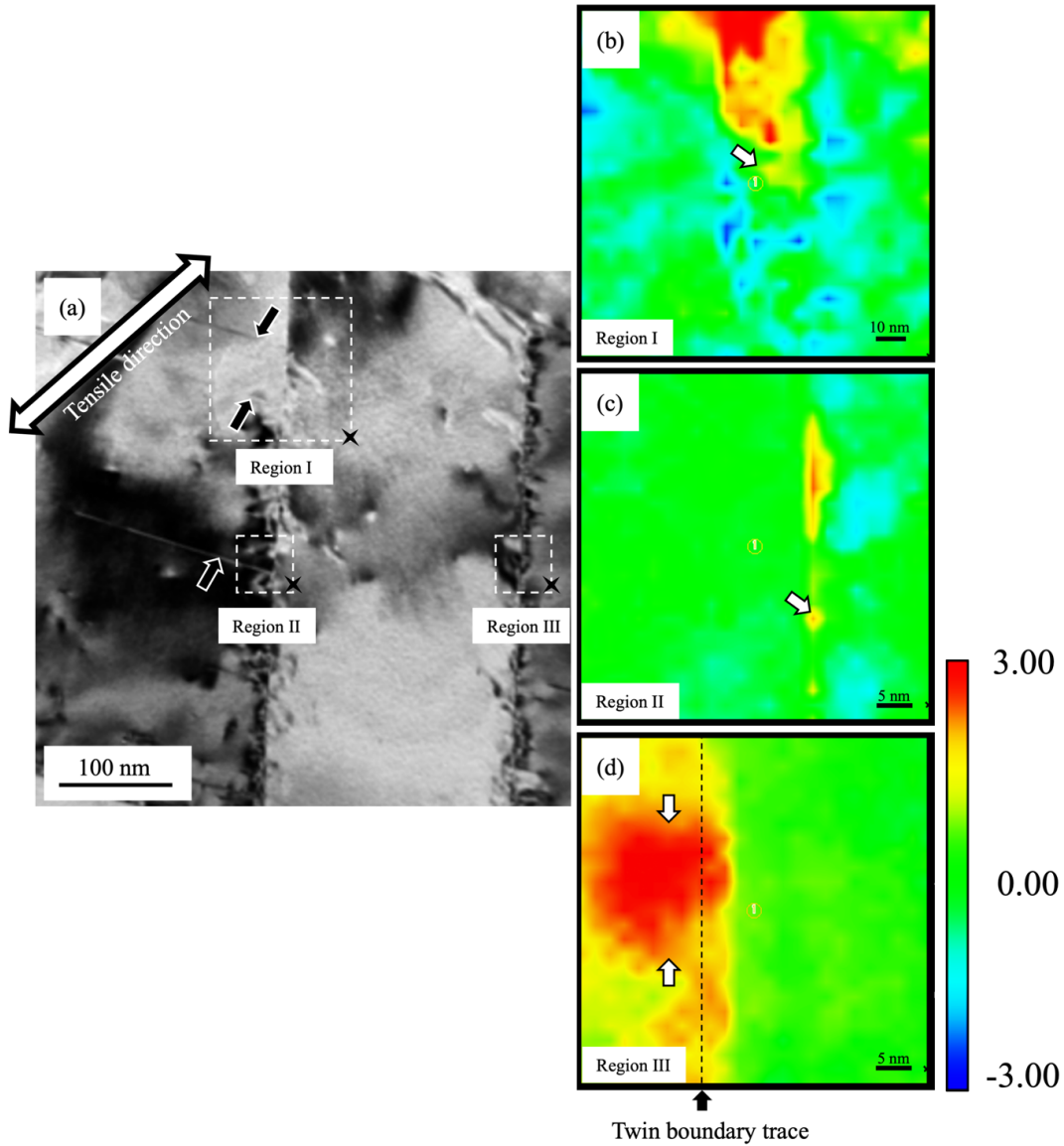


Figure 5.5 (a) BF image shows three deformation twins nucleated from the one side of a $\Sigma 3\{111\}$ twin boundary. Three regions of interest are squared by white dash lines and marked as Region- I, II, and III. (b- d) The strain maps of the three regions in $[1\bar{1}\bar{1}]$ direction show the strain distribution. The color map represents strain (%). Red indicate tensile strain and Blue indicates compression strain.

5.4 Discussion

The main finding of the present study is that the coherent $\Sigma 3\{111\}$ twin boundaries in the UFG TWIP steel can be a nucleation site for deformation twins by a two-step deformation process: (1) The formation of kink-like steps by grain boundary migration

mechanism, (2) The defective step containing mixed character grain boundary dislocations introduce the localized strain concentration that stimulates the sequential emission of Shockley partial dislocation at/near a kink-like step. Here, the differences in the microstructural response of the $\Sigma 3 \{111\}$ twin boundaries to plastic deformation in the present UFG TWIP steel and the coarse-grained counterpart [27] will be discussed.

Deformation activities at/near grain boundaries in face-centered cubic metals have been extensively described, both in experimentally [27,32,33] and theoretically [30,34–41]. Grain boundaries can be an effective dislocation source if their rotation axis is well aligned with the dislocation lines of Shockley partials or perfect dislocations such as a $[112] \Sigma 21$ tilt boundary [42] or a $[011] \Sigma 9$ tilt boundary (**Fig. 5.2(b)**) [30], or if their excess free volume within grain boundary regions could facilitate the formation of Shockley partial dislocation. On the other hand, the rotation axis of the coherent $\Sigma 3 \{111\}$ boundary is not parallel to the dislocation line of perfect or Shockley partial dislocations, and no free volume exist in the coherent $\Sigma 3 \{111\}$ boundary. Accordingly, it is generally believed that the coherent $\Sigma 3 \{111\}$ boundary is unlikely to act as a proactive dislocation source.

Our previous study [27] indicates that the nucleation of deformation twin at a $\Sigma 3 \{111\}$ boundary is very likely initiated from a localized strain concentration field induced by the interaction between piled-up dislocations and the boundary. The accumulated stress can be reduced by a grain boundary relaxation event, i.e., by emitting sequential stacking faults to closely spaced slip planes thus promoting the nucleation of deformation twin. This appears to be true if the grain size is large enough to offer sufficient rooms for Frank-Read dislocation sources to be bred so that a group of in grain dislocations can be generated and will interact with the grain boundaries. However, the in grain dislocation sources in the

present UFG steel are unlikely active due to the grain size constraint.

To explain the nucleation of deformation twin at $\Sigma 3\{111\}$ twin boundaries shown in **Fig. 5.2(b - d)**, there must be an alternative mechanism that is complicatedly related to the twin boundary structure and is different from the mechanism related to dislocation dynamics observed in coarse-grained TWIP steels. In case of the general high-angle grain boundaries in **Fig. 5.2(a - b)**, the grain boundaries acting as a dislocation source were frequently observed and could be ascribed by grain boundary structure transition or by free-volume assisted dislocation emission process [30,34–41] that have been demonstrated in coarse-grained TWIP steels. However, the free volume that long-period grain boundaries have does not exist in the coherent $\Sigma 3\{111\}$ boundary. Therefore, we assume that the coherent $\Sigma 3\{111\}$ boundary in the present UFG TWIP steel may be either inherently defective or become defective by a particular deformation mode and the defective $\Sigma 3\{111\}$ boundary can easily emit the Shockley partial dislocations observed in MD simulation [37]. In fact, Wang et al. has reported that many coherent boundaries in an nanotwinned copper alloy are inherently defective, having several kink-like steps (< 1 nm) prior to deformation [43]. Then, both in-situ deformation TEM [44] and MD simulation [45] studies have suggested that the formation of the steps is a result of grain boundary migration via motion of Shockley partial dislocations on the $\Sigma 3\{111\}$ twin boundary.

In the present study, the structures of the representative coherent $\Sigma 3\{111\}$ boundary prior to tensile straining in **Fig. 5.6(a)** shows a perfect and coherent atomic configuration with no defective step. Although there are several large incoherent $\Sigma 3\{112\}$ grain boundary being observed along the coherent $\Sigma 3\{111\}$ twin boundaries such as the representative one in **Fig. 5.6(b)**, these incoherent $\Sigma 3\{112\}$ boundaries without having a strong strain contrast

are formed by annealing and considered to be more stable than the steps (< 1 nm) formed by deformation [43,44,47,48].

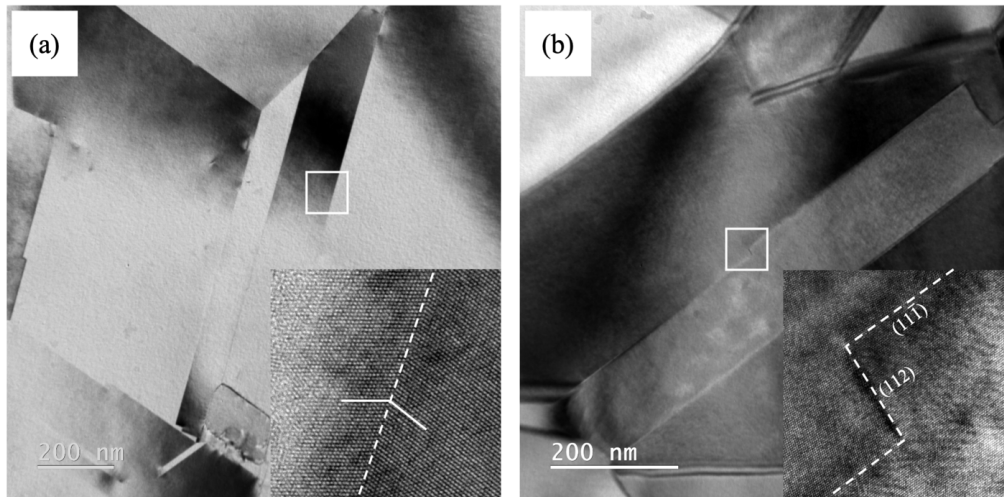


Figure 5.6 Two pairs of BF TEM and HRTEM images show two representative boundary structures of two $\Sigma 3\{111\}$ twin boundaries in an undeformed sample. (a) The atomic structure corresponding to the region marked by a white square shows the atomistically coherent and flat twin boundary. (b) The atomic structure corresponding to the region marked by white square shows a 5 nm (112) incoherent twin boundary.

Concerning the characteristic strain contrast that uniformly spreads along the coherent $\Sigma 3$ twin boundaries in **Fig. 5.2(c-e)**, these contrast are likely to be associated with the dislocations that glide on the boundary and their source may be the neighboring triple junction which has been described to be an effective dislocation source in nanocrystalline materials [49,50]. As a result, the Shockley partial dislocations could change the local boundary structure, i.e., kink-like steps were formed at a $\Sigma 3\{111\}$ twin boundary to accommodate the misfit between grains. As the localized stress field at /near defective steps exceeds the twinning stress during plastic deformation, the Shockley partial dislocation emission could take place and glide into the matrix-lamella along the successive $(\bar{1}1\bar{1})$ planes that are inclined to the $(11\bar{1})$ twin boundary as shown in **Fig. 5.4(c)**.

To determine the Burgers vector of the grain boundary dislocations associated with the steps, Frank circuit approach [48,51,52] was applied as shown in **Fig. 5.7**. Two enclosed

Frank circuits labeled by “A” and “B” were used to analyze the steps. The lattice vectors traveling around the circuits were recorded and labeled from t_1 to t_8 , i.e., the vectors from t_1 to t_4 and the vectors from t_5 to t_8 were defined with respect to the crystal frame of grain I (Twin) and grain II (Matrix), respectively. The Burgers vector of grain boundary dislocation can be determined by the summation of the lattice vectors when lattice vectors of $t_5 \sim t_8$ were coordinately transformed into the ones in crystal frame of twin. The Burgers vector of the grain boundary dislocation then can be expressed as the following:

$$b_{GB} = -\sum_1^8 t = 1/6[112]_I \quad (1)$$

, where the translation vectors of $t_1 \sim t_8$ are listed in **Fig. 5.7**. This Burgers vector of the grain boundary dislocation in the circuit A was determined to have a mixed character, i.e., the Burgers vector of grain boundary dislocation can be described by two specific displacement shift complete (DSC) lattice vectors:

$$b_{GB} = 1/6[112]_I = -d_1 + d_3 = -1/12[\bar{2}1\bar{1}]_I + 1/4[011]_I \quad (2)$$

, where d_1 and d_3 are the DSC lattice vectors illustrated in the schematic of **Fig. 5.7**. This step formed by the plastic deformation would generate a stress field thus stimulating deformation twin nucleation. On the other hand, the summation of the lattice vectors in the circuit B is zero meaning no Burgers vector is included. This result indicates that the three-monolayer height step could be a pure step (free of lattice defects), or the current HRTEM image taken from this particular zone axis (crystallographic direction) could not completely resolve the structure of the step, i.e., the displacement might exist in the direction parallel to the electron beam \sim zone axis. In the present study, multiple $\Sigma 3\{111\}$ boundaries prior to tensile straining were carefully examined and confirmed to have a perfect and coherent atomic configuration with no defective steps. Therefore, the authors would like to suggest

that the three-monolayer height step in here was formed by deformation rather than inherently defective.

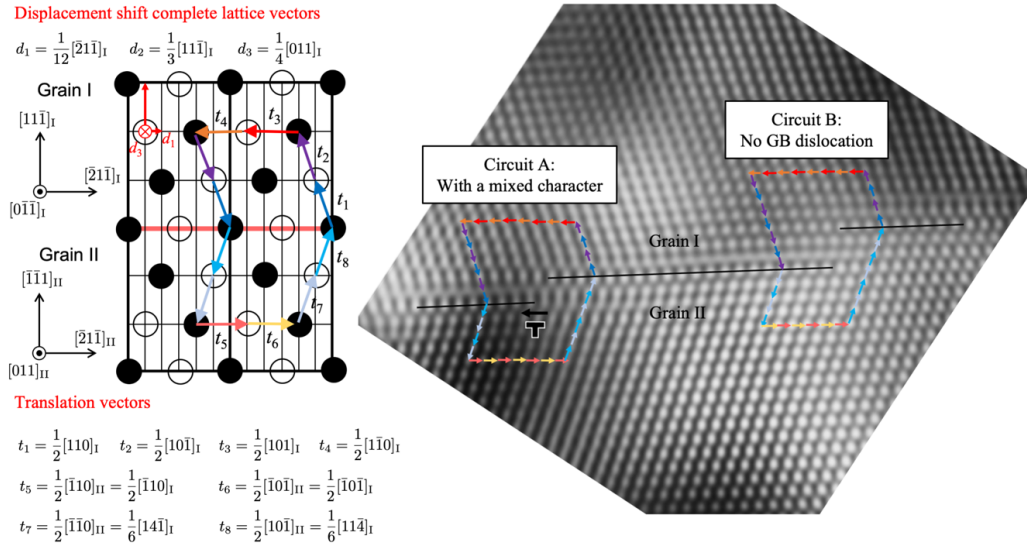


Figure 5.7 Two closed Frank circuits labeled by “A” and “B” were used to analyze the steps imaged in Fig. 4(b). The Burgers vector in circuit A was identified to have a mixed character, while the Burgers vector of dislocation in circuit B was not identified. The step in circuit B could be a pure step, or the displacements of the step might exist in the direction parallel to the electron beam direction \sim zone axis thus its structure cannot be resolved. The corresponding lattice vectors are schematically illustrated and described with a proper coordinate matrix transformation, as labeled from t_1 to t_8 . The corresponding displacement shift complete (DSC) lattice vectors are also specified to be $d_1 = 1/12 [\bar{2}1\bar{1}]_I$, $d_2 = 1/3[11\bar{1}]_I$, and $d_3 = 1/4[011]_I$.

A quantitative analysis with the nanobeam diffraction (NBD) analysis program was conducted to examine the correlation between local strain level and deformation twinning behavior. The strain level at/near the step in **Fig. 5.5(d)** is approximately $3.65\% \pm 0.32$ in average by taking all individual data points in the near-step region into account, while the strain level near the step with a deformation twin in **Fig. 5.5(c)** is significantly low, approximately $-0.02\% \pm 0.52$ in average. Our Frank circuit approach indicates that the strain concentration at the step in **Fig. 5.5(d)** is notable due to the contribution of the grain boundary dislocations having a mixed character and this appears to be consistent with the strain field of the Shockley partial dislocation having a pure edge component [53,54]. In contrast, the disappearance of localized strain field in **Fig. 5.5(c)** is likely caused by the

nucleation of deformation twin.

The two-step mechanism to form a nucleation site for deformation twins is schematically illustrated in the **Fig. 5.8(a)**, which represents the case in **Fig. 5.4(c)** where a 4-atomic-layered deformation twin was formed from a 3-monolayer height step. The first step of this process is: the resolved shear stress applied to the twin boundary would be intensified to stimulate the glide of Shockley partial dislocations. This dislocation activity introduces a step having a several-monolayer height that can be described as the grain boundary migration. The second step is: the step could have a localized strain concentration when it contains a mixed character grain boundary dislocation, then the nucleation of deformation twin is stimulated as the localized strain accumulate progressively. It should be noted that the angle between the grain boundary plane and the macroscopic axis of tension could possibly change during the deformation unlike the angle between the grain orientation and the axis of tension. The formation of ~1 nm deformation twin is schematically illustrated in **Fig. 5.8(b)**, demonstrating the emission of closely spaced overlapping stacking faults lying on parallel $(\bar{1}1\bar{1})$ planes from (i) to (iii). The Burgers vector of residual grain boundary dislocations after the nucleation of deformation twin can be determined by the following relationship:

$$b_R = b_{in} - b_{out} \quad (3)$$

, where b_R is the Burgers vector of residual grain boundary dislocation, b_{in} is the Burgers vector of the dislocations within defective step, b_{out} is the Shockley partial dislocation emitted from the step. Based on the crystallographic orientation relationship between the $\Sigma 3$ boundary and deformation twin, b_{in} and b_{out} can be designated to be $1/6[1\bar{2}\bar{1}]$ and $1/6[21\bar{1}]$ respectively. As a result, the magnitude of the residual grain boundary dislocation, i.e., $b_R =$

$1/6 [\bar{1}03]$, becomes larger than that of b_{in} and b_{out} . This suggests that the formation of deformation twin from the step is unlikely to be an energetically favorable event from the Burgers reaction standpoint. However, the released elastic strain energy by deformation twinning could be larger than the net dislocation energy increase.

The nucleation of deformation twin consisted of sequential Shockley partial dislocations can be explained by a universal energy relationship of the planar fault energy barriers in many FCC metals [55]:

$$\gamma_{utf} \cong \frac{1}{2} \cdot \gamma_{isf} + \gamma_{usf} \quad (4)$$

, where γ_{isf} is the intrinsic stacking fault energy, γ_{usf} is the unstable stacking fault energy, and γ_{utf} is the energy required to transform an intrinsic stacking fault to an extrinsic stacking fault. The term of $\frac{1}{2} \cdot \gamma_{isf}$ becomes negligible due to the low γ_{isf} of 40 mJ m^{-2} for the present alloy so that the γ_{utf} will be comparable to γ_{usf} . As long as the energy barrier γ_{utf} and γ_{usf} for continuous generation of stacking faults on the adjacent $\{111\}$ planes can be conquered, the deformation twinning at/near step could be achievable. Our study renders that the formation of the defective step containing mixed character grain boundary dislocations is required for localized strain accumulation thus stimulating the deformation twinning, which is different from the case in coarse-grained TWIP steel where the strain concentration is induced by the dislocation pile-ups [27].

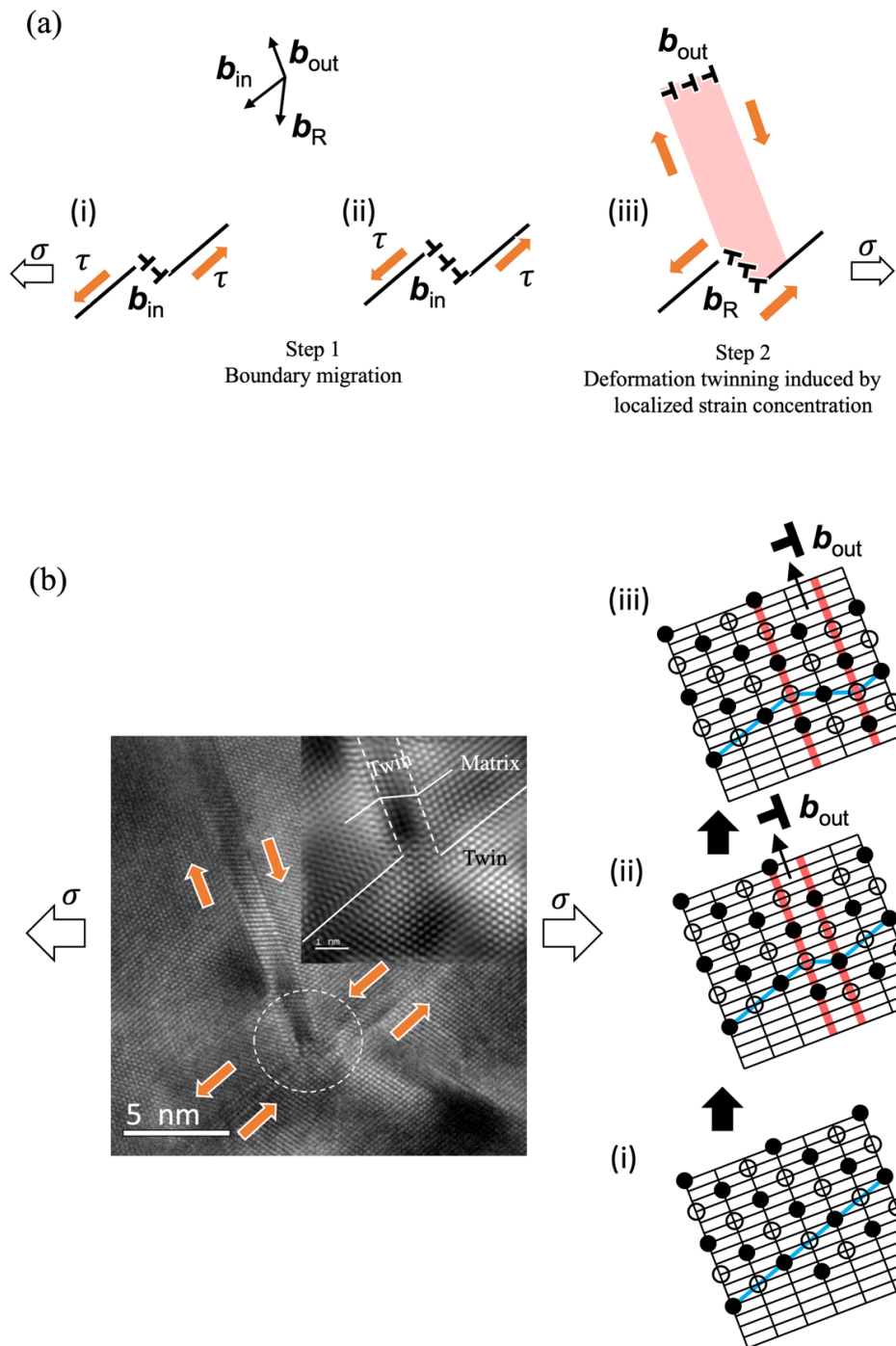


Figure 5.8 (a) A schematic illustration shows a two-step mechanism to form a nucleation site for deformation twin at a coherent annealing twin boundary. Step 1: Dislocations having Burgers vector of b_{in} are formed by grain boundary migration under an applied stress. Step 2: The defective step containing mixed character grain boundary dislocations introduce the localized strain accumulation progressively thus stimulating the deformation twin nucleation. (b) Deformation twinning processes (i, ii, iii) were schematically illustrated. The emission of closely spaced overlapping stacking faults lying on parallel $(\bar{1}\bar{1}\bar{1})$ planes was demonstrated with a step-by-step manner.

5.5 Conclusions

In this study, the role of $\Sigma 3\{111\}$ twin boundaries on the deformation twinning process was investigated in an UFG Fe-31Mn-3Si-3Al austenitic TWIP steel using in-situ TEM deformation and microprobe-STEM based strain mapping experiments. The detailed analysis of microstructural features and the strain state near the deformed $\Sigma 3\{111\}$ boundaries have drawn the following conclusions:

- 1) Localized strain concentration stimulates the nucleation of deformation twins at coherent $\Sigma 3\{111\}$ grain boundaries, thus the deformation twin nucleation can occur on all type of observed boundaries regardless of the grain boundary misorientation character, i.e., general high-angle grain boundary, boundaries having a particular tilt axis ($[011]\Sigma 9$), and low-energy coherent twin boundaries are all can be a nucleation site for deformation twin.
- 2) The formation of kink-like steps containing a mixed character grain boundary dislocation appears to be governed by the motion of Shockley partial dislocation on the planes of $\Sigma 3\{111\}$ twin boundary. This type of steps would accumulate strain, and the nucleation of deformation twins occurs at/near the kink-like step when the localized stress level exceeds the twinning stress.
- 3) The mechanism to generate strain concentrations at $\Sigma 3\{111\}$ twin boundaries is different between the UFG and coarse-grained TWIP steels due to the grain size constraint suppressing the grain interior dislocation activities in the UFG steel. On the other hand, the observed invisibility of stacking fault contrast during the deformation twin nucleation at $\Sigma 3\{111\}$ boundaries suggests that the deformation twin nucleation process could be identical in both the UFG and coarse-grained Fe-31Mn-3Si-3Al TWIP steel.

References

- [1] B. VERLINDEN, Severe plastic deformation of metals, *Metal. Metall.* 11 (2005) 165–182.
- [2] R.Z. Valiev, I. V. Alexandrov, Y.T. Zhu, T.C. Lowe, Paradox of Strength and Ductility in Metals Processed Bysevere Plastic Deformation, *J. Mater. Res.* 17 (2002) 5–8.
- [3] Y. Saito, H. Utsunomiya, N. Tsuji, T. Sakai, Novel ultra-high straining process for bulk materials—development of the accumulative roll-bonding (ARB) process, *Acta Mater.* 47 (1999) 579–583.
- [4] N. Tsuji, Y. Saito, H. Utsunomiya, S. Tanigawa, Ultra-fine grained bulk steel produced by accumulative roll-bonding (ARB) process, *Scr. Mater.* 40 (1999) 795–800.
- [5] Y. Estrin, A. Vinogradov, Extreme grain refinement by severe plastic deformation: A wealth of challenging science, *Acta Mater.* 61 (2013) 782–817.
- [6] N. Tsuji, Y. Ito, Y. Saito, Y. Minamino, Strength and ductility of ultrafine grained aluminum and iron produced by ARB and annealing, *Scr. Mater.* 47 (2002) 893–899.
- [7] H. Takechi, Metallurgical Aspects on Interstitial Free Sheet Steel from Industrial Viewpoints., *ISIJ Int.* 34 (1994) 1–8.
- [8] R.Z. Valiev, I. V. Alexandrov, Y.T. Zhu, T.C. Lowe, Paradox of Strength and Ductility in Metals Processed Bysevere Plastic Deformation, *J. Mater. Res.* 17 (2002) 5–8.
- [9] N.J. Petch, The cleavage strength of polycrystals, *J. Iron Steel InstInst.* (1953).
- [10] E.O. Hall, The deformation and ageing of mild steel: II Characteristics of the Lüders deformation, *Proc. Phys. Soc. Sect. B.* (1951).
- [11] Y. Wang, M. Chen, F. Zhou, E. Ma, High tensile ductility in a nanostructured metal,

- Nature. (2002).
- [12] J.W. Morris, Jr., Comments on the Microstructure and Properties of Ultrafine Grained Steel, *ISIJ Int.* 48 (2008) 1063–1070.
- [13] R. Zheng, T. Bhattacharjee, A. Shibata, T. Sasaki, K. Hono, M. Joshi, N. Tsuji, Simultaneously enhanced strength and ductility of Mg-Zn-Zr-Ca alloy with fully recrystallized ultrafine grained structures, *Scr. Mater.* (2017).
- [14] N. Tsuji, S. Ogata, H. Inui, I. Tanaka, K. Kishida, S. Gao, W. Mao, Y. Bai, R. Zheng, J.-P. Du, Strategy for managing both high strength and large ductility in structural materials—sequential nucleation of different deformation modes based on a concept of plaston, *Scr. Mater.* 181 (2020) 35–42.
- [15] C.-Y. Hung, Y. Bai, N. Tsuji, M. Murayama, Grain size altering yielding mechanisms in ultrafine grained high-Mn austenitic steel: advanced TEM investigations, *J. Mater. Sci. Technol.* 86 (2021) 192–203.
- [16] R. Saha, R. Ueji, N. Tsuji, Fully recrystallized nanostructure fabricated without severe plastic deformation in high-Mn austenitic steel, *Scr. Mater.* 68 (2013) 813–816.
- [17] J.-Y. Lee, J.-S. Hong, S.-H. Kang, Y.-K. Lee, The effect of austenite grain size on deformation mechanism of Fe-17Mn steel, *Mater. Sci. Eng. A.* (2021) 140972.
- [18] B.C. De Cooman, Y. Estrin, S.K. Kim, Twinning-induced plasticity (TWIP) steels, *Acta Mater.* 142 (2018) 283–362.
- [19] O. Bouaziz, S. Allain, C.P. Scott, P. Cugy, D. Barbier, High manganese austenitic twinning induced plasticity steels: A review of the microstructure properties relationships, *Curr. Opin. Solid State Mater. Sci.* 15 (2011) 141–168.

- [20] S. Vercammen, B. Blanpain, B.C.C. De Cooman, P. Wollants, Cold rolling behaviour of an austenitic Fe-30Mn-3Al-3Si TWIP-steel: The importance of deformation twinning, *Acta Mater.* 52 (2004) 2005–2012.
- [21] J.. Venables, The nucleation and propagation of deformation twins, *J. Phys. Chem. Solids.* 25 (1964) 693–700.
- [22] J.B. Cohen, J. Weertman, A dislocation model for twinning in f.c.c. metals, *Acta Metall.* 11 (1963) 996–998.
- [23] H. Fujita, S. Ueda, Stacking faults and f.c.c. (γ) \rightarrow h.c.p. (ϵ) transformation in 18 8-type stainless steel, *Acta Metall.* 20 (1972) 759–767.
- [24] MIURA S, TAKAMURA J, NARITA N, ORIENTATION DEPENDENCE OF THE FLOW STRESS FOR TWINNING IN SILVER CRYSTALS, (1967) 555–562.
- [25] S. Mahajan, G.Y. Chin, Comments on deformation twinning in silver- and copper-alloy crystals, *Scr. Metall.* 9 (1975) 815–817.
- [26] H. Beladi, I.B. Timokhina, Y. Estrin, J. Kim, B.C. De Cooman, S.K. Kim, Orientation dependence of twinning and strain hardening behaviour of a high manganese twinning induced plasticity steel with polycrystalline structure, *Acta Mater.* 59 (2011) 7787–7799.
- [27] C.-Y. Hung, Y. Bai, T. Shimokawa, N. Tsuji, M. Murayama, A Correlation Between Grain Boundary Character and Deformation Twin Nucleation Mechanism in Coarse-grained High-Mn Austenitic Steel, *Sci. Rep.* (2021) In press.
- [28] K. Sato, H. Miyazaki, T. Gondo, S. Miyazaki, M. Murayama, S. Hata, Development of a novel straining holder for transmission electron microscopy compatible with single tilt-axis electron tomography, *Microscopy.* 64 (2015) 369–375.

- [29] A.J. Schwartz, M. Kumar, B.L. Adams, D.P. Field, *Electron Backscatter Diffraction in Materials Science*, Springer US, Boston, MA, 2009.
- [30] M.A. Tschopp, G.J. Tucker, D.L. McDowell, Structure and free volume of $\langle 110 \rangle$ symmetric tilt grain boundaries with the E structural unit, *Acta Mater.* 55 (2007) 3959–3969.
- [31] D.B. Williams, C.B. Carter, *Transmission Electron Microscopy*, Springer US, Boston, MA, 2009.
- [32] V. Shterner, I.B. Timokhina, A.D. Rollett, H. Beladi, The Role of Grain Orientation and Grain Boundary Characteristics in the Mechanical Twinning Formation in a High Manganese Twinning-Induced Plasticity Steel, *Metall. Mater. Trans. A.* 49 (2018) 2597–2611.
- [33] J.K. Kim, M.H. Kwon, B.C. De Cooman, On the deformation twinning mechanisms in twinning-induced plasticity steel, *Acta Mater.* 141 (2017) 444–455.
- [34] T. Shimokawa, M. Tsuboi, Atomic-scale intergranular crack-tip plasticity in tilt grain boundaries acting as an effective dislocation source, *Acta Mater.* 87 (2015) 233–247.
- [35] T. Shimokawa, M. Tanaka, K. Kinoshita, K. Higashida, Roles of grain boundaries in improving fracture toughness of ultrafine-grained metals, *Phys. Rev. B.* 83 (2011) 214113.
- [36] Y. Mishin, M. Asta, J. Li, Atomistic modeling of interfaces and their impact on microstructure and properties, *Acta Mater.* 58 (2010) 1117–1151.
- [37] M.A. Tschopp, D.L. McDowell, Dislocation nucleation in $\Sigma 3$ asymmetric tilt grain boundaries, *Int. J. Plast.* 24 (2008) 191–217.
- [38] D. Spearot, K. Jacob, D. McDowell, Dislocation nucleation from bicrystal interfaces

- with dissociated structure, *Int. J. Plast.* 23 (2007) 143–160.
- [39] D.E. Spearot, K.I. Jacob, D.L. McDowell, Nucleation of dislocations from [001] bicrystal interfaces in aluminum, *Acta Mater.* 53 (2005) 3579–3589.
- [40] C.A. Schuh, M. Kumar, W.E. King, Analysis of grain boundary networks and their evolution during grain boundary engineering, *Acta Mater.* 51 (2003) 687–700.
- [41] V. Randle, *The role of coincidence site lattice in grain boundary engineering*, 1996.
- [42] T. Shimokawa, Asymmetric ability of grain boundaries to generate dislocations under tensile or compressive loadings, *Phys. Rev. B.* 82 (2010) 174122.
- [43] Y.M. Wang, F. Sansoz, T. LaGrange, R.T. Ott, J. Marian, T.W. Barbee, A. V. Hamza, Defective twin boundaries in nanotwinned metals, *Nat. Mater.* 12 (2013) 697–702.
- [44] Y.B. Wang, M.L. Sui, E. Ma, In situ observation of twin boundary migration in copper with nanoscale twins during tensile deformation, *Philos. Mag. Lett.* 87 (2007) 935–942.
- [45] J. Rezaei Mianroodi, B. Svendsen, Effect of Twin Boundary Motion and Dislocation-Twin Interaction on Mechanical Behavior in Fcc Metals, *Materials (Basel)*. 13 (2020) 2238.
- [46] Z. You, X. Li, L. Gui, Q. Lu, T. Zhu, H. Gao, L. Lu, Plastic anisotropy and associated deformation mechanisms in nanotwinned metals, *Acta Mater.* 61 (2013) 217–227.
- [47] L. Zhang, W. Mao, M. Liu, Y. Shibuta, Mechanical response and plastic deformation of coherent twin boundary with perfect and defective structures, *Mech. Mater.* 141 (2020) 103266.
- [48] J.P. Hirth, R.C. Pond, Steps, dislocations and disconnections as interface defects relating to structure and phase transformations, *Acta Mater.* 44 (1996) 4749–4763.

- [49] I.A. Ovid'Ko, N. V. Skiba, Generation of nanoscale deformation twins at locally distorted grain boundaries in nanomaterials, *Int. J. Plast.* 62 (2014) 50–71.
- [50] I.A. Ovid'ko, R.Z. Valiev, Y.T. Zhu, Review on superior strength and enhanced ductility of metallic nanomaterials, *Prog. Mater. Sci.* 94 (2018) 462–540.
- [51] J.. Hirth, R.. Balluffi, On grain boundary dislocations and ledges, *Acta Metall.* 21 (1973) 929–942.
- [52] F.C. Frank, LXXXIII. Crystal dislocations.—Elementary concepts and definitions, London, Edinburgh, Dublin *Philos. Mag. J. Sci.* 42 (1951) 809–819.
- [53] J.P. Hirth, J. Lothe, T. Mura, *Theory of Dislocations* (2nd ed.), Krieger Publishing Company, 1983.
- [54] J.C.M. Li, The interaction of parallel edge dislocations with a simple tilt dislocation wall, *Acta Metall.* 8 (1960) 296–311.
- [55] Z.H. Jin, S.T. Dunham, H. Gleiter, H. Hahn, P. Gumbsch, A universal scaling of planar fault energy barriers in face-centered cubic metals, *Scr. Mater.* 64 (2011) 605–608.

Acknowledgements

This study was partly supported by Nanoscale Characterization and Fabrication Laboratory (NCFL), Institute for Critical Technology and Applied Science (ICTAS), Virginia Tech and used shared facilities at the Virginia Tech National Center for Earth and Environmental Nanotechnology Infrastructure (NanoEarth), a member of the National Nanotechnology Coordinated Infrastructure (NNCI), supported by NSF (ECCS 1542100, ECCS 2025151). N.T., T.S. and M.M. greatly appreciate the financial support by the JST CREST (JPMJCR1994). M.M. acknowledges a financial support by the DOE Basic Energy Science Program (BES DE-FG02-06ER15786) for technical development of TEM in-situ deformation, and JSPS KAKENHI Grant Numbers (No. 19H02029, 20H02479). N.T. acknowledges a financial support by Elements Strategy Initiative for Structural Materials (ESISM, No. JPMXP0112101000), and JSPS KAKENHI (No. 15H05767, No.20H00306), all through the Ministry of Education, Culture, Sports, Science and Technology (MEXT), Japan.

Chapter 6

Conclusions

In this study, we discuss the effect of grain size and grain boundary character on deformation twinning behavior in a model alloy of Fe-31Mn-3Al-3Si austenitic steel using ex-/in- situ deformation TEM to develop a better understanding of twin-induced plasticity. The grain size refinement is generally believed to have a negative effect on deformation twinning mainly due to the lack of carrier of plastic deformation for dislocation dynamics. In the present study, we found that the deformation twinning behavior is indeed inhibited when grain size is refined to few micrometer regimes. However, deformation twinning was not suppressed but promoted as the grain size is refined down to submicron size regime. The discontinuous yielding behavior with yield drop observed in the UFG steel was also found to have a direct correlation with the size of grains. Our results suggest that the yield drop behavior is associated with the lack of carrier of plastic deformation while the regeneration of strain hardening rate can be contributed by the activation of deformation twinning in the UFGs. This grain size effect on deformation twinning behavior were systematically studied, and the correlation between discontinuous yielding behavior and grain size could potentially be transferable to other low-SFE structural materials.

In the coarse-grained TWIP steel counterpart, we found a grain boundary character dependent deformation twinning behavior. We experimentally reveal that deformation twin nucleation occurs at an annealing twin ($\Sigma 3$) boundary in a high-Mn austenitic steel when dislocation pile-up at $\Sigma 3$ boundary produced a local stress exceeding the twinning stress, while no obvious local stress concentration was required at relatively high-energy grain boundaries such as $\Sigma 21$ or $\Sigma 31$. $\Sigma 3$ boundary can act as a strong barrier against dislocations and planar defects

motion thus a local stress concentration field needs to be introduced by dislocations or planar defects piled-up against the $\Sigma 3$ boundary. The deformation twin nucleation at a $\Sigma 3$ boundary would not occur when the incoming dislocations made slip transfer across it. On the other hand, the high-sigma-value boundaries can spontaneously emit dislocations and transform into a much stable grain-boundary structure by a grain boundary relaxation mechanism. This result suggests that the atomic configuration and the free volume within grain boundaries can control the microstructural response of boundaries thus significantly affecting the deformation twinning processes. Grain boundary dependent deformation behavior using in-situ deformation technique in the present study provides not only the technique breakthrough but also the insights into deformation twinning processes at/near different grain boundaries that has not been fully explored in materials science community.

Although high-manganese austenitic steels have been studied for decades, well-developed conventional mechanisms associated with dislocation dynamics are not sufficient to explain the grain boundary mediated deformation twinning behavior in UFG TWIP steel. As a result, we are not yet to control the TWIP in UFGs. In the last part of this study, we provide insights into the deformation processes at/near $\Sigma 3\{111\}$ twin boundary. A defective “kink-like” step was observed along twin boundaries in the early stage of plastic deformation. The steps consisting of grain boundary dislocations with mixed characters will progressively introduce a pronounced localized strain field thus stimulating the nucleation of deformation twin, which is different from the case observed in coarse-grained counterparts. The detailed process of deformation twinning at/near twin boundary provide a possible reason why UFG TWIP can retain good ductility during deformation.